PHOTOVOLTAIC BASED ELECTRIC AND PLUG-IN HYBRID ELECTRIC VEHICLE BATTERY CHARGING INFRASTRUCTURE USING A MODIFIED Z-CONVERTER TOPOLOGY

Giampaolo Carli

A Thesis in the Department of Electrical and Computer Engineering

Presented in Partial Fulfillment of the Requirements

for the Degree of Master of Applied Science at

Concordia University

Montréal, Québec, Canada

August 2009

Library and Archives
Canada

Published Heritage
Branch

395 Wellington Street
Ottawa ON K1A 0N4
Canada

Bibliothèque et
Archives Canada

Direction du
Patrimoine de l'édition

395, rue Wellington
Ottawa ON K1A 0N4
Canada

Canada

ABSTRACT

Photovoltaic Based Electric and Plug-in Hybrid Electric Vehicle Battery Charging Infrastructure using a Modified Z-Converter Topology

Giampaolo Carli

There currently exist numerous uncertainties about the future of energy consumption in the industrialized world. It is safe to claim with confidence that fossil fuel reserves are proving to be inadequate, highly difficult to extract and refine, and less attractive to the community, given their environmental and socio-political impact. More recently, this has lead to the natural conclusion that renewable energy technologies should be preferred over more traditional ones. Replacing carbon as an economic engine can be achieved in numerous ways. However, it is still not clear, as to which renewable options will be more successful. On the other hand, it is quite safe to expect that the trend towards distributed and local power generation, using wind and photovoltaic sources will continue. At the same time, the enormous transportation sector will rely more heavily on electricity and related infrastructure needed for storage and distribution. All the above issues point towards the realization of public and private facilities to generate electricity locally, to recharge electric and plug-in hybrid electric vehicles.

In this thesis, a photovoltaic (PV) source is proposed for electric/plug-in hybrid electric vehicle battery charging, due to the fact that solar panels can be conveniently placed above the vehicle parking space and can double as a shade provider. In fact, such a feature is so desirable that indeed, several installations exist today, that use a carport PV array to generate power for purposes other than EV recharging. Determining the technical

goals for such facilities and discussing some relevant solutions is, broadly, the scope of this thesis. More particularly, the thesis aims at establishing application oriented technical differences between regular PV-grid-tied systems and PV systems that are specifically adapted to public or semi-public EV charging, noting that the former arrangement has enjoyed much attention in literature. This goal will be accomplished by presenting the design process for one such system, starting with the definition of technical specifications that take into account all the real constraints dictated by the state of the art in PV and battery technologies, grid interface requirements, safety standards, and market demands. The second part of this thesis focuses on the power converter topology, with strong emphasis on the analysis of the Z-loaded/sourced converter, as a fairly suitable and practical topology. At the same time, other possible topologies will also be considered for comparison purposes, especially with regards to reliability, efficiency, and cost.

ACKNOWLEDGMENTS

TABLE OF CONTENTS

LIST OF FIGURES

LIST OF TABLES

LIST OF ACRONYMS

ASD   Adjustable Speed Drive

DCM   Discontinuons Conduction Mode

DSP   Digital Signal Processing

ESR   Equivalent Series Resistance

EV   Electric Vehicle

FET   Field Effect Transistor

HEV   Hybrid Electric Vehicle

HF   High Frequency

IGBT   Insulated Gate Bipolar Transistor

MPP   Maximum Power Point

MPPT   Maximum Power Point Tracking

MTBF   Mean Time Between Failures

NPC   Neutral Point Clamped

PF   Power factor

RHP   Right Hand Plane

RMS   Root Mean Square

SOC   State of Charge

SUR   Switch Utilization Ratio

VSI   Voltage Sourced Inverter

ZVS   Zero Voltage Switching

LIST OF PRINCIPAL SYMBOLS

C	Z-converter impedance circuit capacitance
C_{HB}	Z-converter half-bridge capacitance
D	Z-converter duty cycle or modulation index
D_o	Z-converter shoot-though duty cycle
$D_{o(max)}$	Maximum shoot-through duty cycle
E_{off}	IGBT turn-off energy loss
E_{on}	IGBT turn-on energy loss
F_G	Grid frequency
F_{SW}	Switching frequency
I_B	Battery Charge or discharge current
i_B	AC small signal of battery current
$I_{bp(RMS)}$	Rms current for DC-DC FET in Z-converter (Z-circuit side)
$I_{bs(AVG)}$	Rms current for DC-DC FET body diode in Z-converter (battery side)
I_c	Current in Z-circuit capacitor
I_{IN}	Grid current
i_{IN}	AC small signal of grid current
I_L	Current in Z-converter impedance circuit inductor
I_{LB}	Battery charge current
i_L	AC small signal of current in Z-converter impedance circuit inductor
I_{PV}	Solar panel output current
I_R	IGBT rated current
$I(t)_{pk}$	IGBT instantaneous current

K_{PV}	Photovoltaic utilization factor
L	Z-converter impedance circuit inductance
L_B	Battery charging inductance
L_{IN}	Grid source equivalent inductance
N	Transformer turns ratio
$P_c(t)$	Instantaneous reactive power in Z-converter impedance circuit capacitor
P_G	Grid power (absorbed or delivered)
$P_g(t)$	Instantaneous grid power (absorbed or delivered)
$P_{sw,OFF}$	IGBT power dissipation due to turn-off transition
$P_{sw,ON}$	IGBT power dissipation due to turn-on transition
R_B	Equivalent battery charging resistance
R_C	Z-converter impedance circuit capacitor ESR
R_{HB}	DC-DC half-bridge capacitor ESR
R_{IN}	Grid source equivalent resistance
R_L	Z-converter impedance circuit inductor ESR
V_B	Battery voltage
$V_{B(max)}$	Maximum battery Voltage
$V_{B(min)}$	Minimum battery Voltage
V_C	Z-converter impedance circuit capacitor voltage
v_C	AC small signal of Z-converter impedance circuit capacitor voltage
$V_{C(max)}$	Maximum Z-converter impedance circuit capacitor voltage
$V_{C(min)}$	Minimum Z-converter impedance circuit capacitor voltage
$Vg_{(PK)}$	Peak of grid source voltage (modified by isolation transformer gain)

V_{HB}	DC-DC half-bridge capacitor voltage
V_{IN}	Grid source voltage
V_{PV}	Photovoltaic source voltage
$V_{PV(max)}$	Maximum photovoltaic source voltage
V_R	IGBT rated voltage
$V(t)_{pk}$	IGBT instantaneous voltage
δ	AC small signal of duty cycle D
δ_0	AC small signal of duty cycle Do
ΔI_L	Z-converter impedance circuit inductor peak-peak switching ripple current
ΔV_C	Z-converter impedance circuit capacitor peak-peak ripple voltage (120Hz)
ω	Grid source angular frequency

CHAPTER 1

INTRODUCTION

1.1 BACKGROUND

All-electric autonomy of batteries is a well-known issue for gaining consumer confidence in electric vehicle (EV) performance. The major concern is the present limit for Li-ion and Ni-MH batteries to a practical drive range of 300km (180mi) on a single charge. This is coupled with a pervasive shortage of charging stations that, even when available, cannot generate enough power for fast charging (less than 15 minutes). Even in the likely event that fast charging will be available soon, it is conceivable that the necessary high power availability will come with an additional price to the user. It appears, that EVs will continue to benefit from slower charging strategies. For instance, standard Level II (SAE J1772) charging, bounds the available power to less than 14.4kW so that a fully depleted 35kWh battery pack will require 2½ hours to achieve full state-of-charge (SOC). In realistic circumstances, this naturally implies that the charging station will also double as a parking facility, where the vehicle is expected to reside for relatively long time periods. For instance, a typical clientele of the carport could be urban office workers, who commute from their home to their workplace, and are expected to use the car only very lightly during their workday. In fact, the typical worker will park in the morning, with only a partially discharged battery, and leave at night, fully recharged. As the required level of charging power over an 8 hour-day period could be less than 1.5kW, it is then conceivable that some (or most) parking places be equipped with only Level I charging.

1

As will be shown through the research performed in this thesis, where photovoltaic generation is convenient, power levels compatible with both Level I and II are possible, making solar carports ideal for EV charging applications.

1.2 GRID CONNECTION

For practical purposes, connection of the carport to the grid is highly desirable, as such a connection would serve a number of useful purposes. The grid would primarily act as extended storage by collecting excess energy produced by the PV array. This will relieve the carport from the task of locally storing energy in batteries or flywheels. Secondly, the grid can supplement any deficiency in PV generation, during cloudy days or at night, for instance. Finally, storing energy during peak hours of grid utilization and the availability of connected batteries during the same period seems to be the optimal solution for the utility company for the many potential benefits described in [1], namely power factor improvement, back-up power during grid failures, and peak shaving.

About the last point, it is well worth pausing on the realization that stand-alone installations, such as micro-grids, must allow locally generated power to be stored in battery banks, as well as being converted to AC, in order to drive neighboring loads. At the same time, power must also be allowed to flow from the batteries to the AC line at times when PV generation is lacking. It appears then, that at least three out of the four power flow paths described above also apply to stand-alone systems. The order of importance for the power paths is not the same; nevertheless, it is still conceivable that many findings within this thesis may be applicable to micro-grids as well. Keeping this fact in mind, this thesis will, henceforth, focus solely on PV grid-tied EV charging applications.

1.3 CONTRIBUTION OF THE THESIS

This thesis is divided into two main parts. The first is devoted to determining the major technical features that can be attributed to a plausible PV public charging facility of the present and future. Chapter 2 discusses present conditions for the EV market, and attempts to determine the related prescriptions for PV charging, such as battery interface and communication with the on-board controller. Chapter 3 looks at the characteristics, requirements, and limitations of solar panel arrays and establishes the electrical and physical configurations that maximize performance. The results from these two chapters are subsequently used in Chapter 4, dealing with grid interface, in order to outline rough power demands and specifications for the overall system.

Based on these findings, the second part of this thesis explicitly addresses the topic of power conversion, which is most definitely the central function of the PV charging infrastructure. Special attention is devoted to the Z-sourced/loaded inverter-rectifier [2], because it offers the possibility of controlling grid power and battery power through a single stage of conversion. In fact this "3-way" power flow is the most significant difference between regular PV-grid-tied systems and PV-grid-tied systems for EV charging purposes, compelling the designer to give a fresh look to conversion topologies that might otherwise be ignored. With regards to the Z sourced/loaded converter, the main contribution of this thesis will be to demonstrate that stable and acceptable operation for all power flow paths is possible, even when using conventional SISO linear control methods. This is done by actually carrying out a sample design for the system, based on the requirements found in Chapter 4. It is important to note that this study is mainly concerned with the performance of the proposed topology, rather than the

control. Thus, the present choice of a linear control scheme, as compared to more sophisticated and effective methods, must be viewed as an expedient approach to obtaining a functioning power processor model for analysis and comparison. As such, the stability analysis presented in this thesis is neither general nor comprehensive. However, it successfully underlines the associated challenges posed by the Z-converter, including non-minimum phase behavior due to the presence of Z-circuit resonance. Having demonstrated the feasibility of the Z-converter system, its performance is also evaluated and compared to that of two other topologies, each representative of an alternate design philosophy, with special relevance granted to cost, efficiency, and reliability.

CHAPTER 2

ELECTRIC VEHICLE CHARGING ISSUES

2.1 BATTERY CHARGING STRATEGIES

EV/PHEV batteries are typically charged by a DC power supply that is normally derived from an AC source. Many earlier EVs utilized off-board chargers for this purpose, in order to avoid adding weight to the vehicle. With technological advances in the field of power electronics and in consideration of the added convenience to the user, most electric vehicles today use an on-board rectifier. In fact, today's EV/PHEV manufacturers loosely follow SAE J1771 recommendations that require an AC electrical connection and power capacity not to exceed 14.4kW. Moreover, common wisdom may suggest that this strategy has the supplemental benefit of simplifying future public infrastructure. To this point, the California Air Resources Board (CARB), through their report *"ZEV Infrastructure: A Report on Infrastructure for Zero Emission Vehicles,"* invokes economic factors to suggest that electric vehicles be minimally equipped with an on-board rectifier. Table 2-1 shows the standard charging levels and their significance. While levels I and II are in line with the above considerations, SAE J1772 also includes provision for so-called fast charging (level III), which allows for the transfer of much higher power levels to EV/PHEV batteries.

Table 2-1 Summary of Charging Levels for EVs/PHEVs

Charging Levels	
Level 1	"Level 1" EV charging employs cord & plug connected portable EV supply equipment (EVSE) that can be transported with an EV. This equipment is used specifically for EV charging and shall be rated at 120 VAC and 15A, and shall be compatible with the most commonly available grounded electrical outlet (NEMA 5-15R).
Level 2	EV charging employs permanently wired EVSE that is operated at a fixed location. This equipment is used specifically for EV charging and is rated at less than or equal to 240 VAC, less than or equal to 60A, and less than or equal to 14.4 kW.
Level 3	EV charging employs permanently wired EVSE that is operated at a fixed location. This equipment is used specifically for EV charging and is rated at greater than 14.4 kW.

Presently, fast charging is not commonly used, mainly because commercially available battery technologies do not allow for excessive charging currents. Furthermore, at this time such quick charging schemes can only be regarded as a marketing gimmick, because of the required massive power demand. To charge a 35-kWh battery in 10 minutes requires 250 kilowatts of power—five times as much as the average office building consumes at its peak [3]. Notwithstanding these important impediments for the development of public level III infrastructure, the market drive for the possibility of quick refueling stops at charging stations (as is now done with gas stations) makes such development very likely in the future. This is especially true in view of continuing efforts to improve battery chemistry and ultra-capacitor specifications to allow higher currents. The advent of fast charging will most certainly presuppose a return to off-board rectifiers, so that direct access to the battery pack will become a necessity. It is, thus, reasonable to predict that future EVs/PHEVs will have both AC and DC plugs for battery charging. Such an assumption is critical for the purpose of the study carried out in this thesis, as the

PV resource provides DC power, bypassing the on-board rectifier, in order to minimize energy losses.

2.2 VOLTAGE LEVELS

Battery technology for EVs/PHEVs is still being developed, and has not yet reached maturity, let alone any kind of standardization. Each manufacturer is free to choose different chemistries and system designs; hence, it is currently impossible to establish a common specification. For the purpose of this thesis, the most problematic parameter is the voltage level, given that in some cases a transformer and corresponding inverter must be added to allow for voltage flexibility. Even with addition of a transformer, it is impossible to correctly quantify the performance of the power processor, if the battery voltage is allowed to possess a very wide range. Therefore, in wishful expectation that such voltage be standardized at some point in the future, a reasonable assumption must be made in the short-term.

Table 2-2 Nominal Battery Voltage Levels for Several Vehicle Models

Chevy Volt	350V	DC connection: no	Fast charging (level 3): no
GM EV1	312V	DC connection: no	Fast charging (level 3): no
Phoenix Motorcars	380V	DC connection: yes	Fast-charging (level 3): yes
Tango	350V	DC connection: devel	Fast-charging (level 3): devel
Tzero	340V	DC connection: no	Fast charging (level 3): no
Tesla Roadster	375V	DC connection: no	Fast charging (level 3): yes
Honda EV	288V	DC connection: no	Fast charging (level 3): no
Toyota RAV4 EV	288V	DC connection: no	Fast charging (level 3): no
Fisker Karma	400V	DC connection: no	Fast charging (level 3): no
Toyota Prius	275V	DC connection: no	Fast charging (level 3): no
American Electric	48V	DC connection: no	Fast charging (level 3): no
Dynasty EV	72V	DC connection: no	Fast charging (level 3): no

Table 2-2 shows the nominal battery voltages for various EV/PHEV models, suggesting that a range between 275V to 400V represents a reasonable assumption,

although some neighborhood vehicles still use lead-acid batteries, and have much lower nominal voltages.

2.3 SAFETY

Vehicles are intrinsically non-stationary, and consequently, cannot be grounded through a permanent safety conductor. As the battery pack voltages are quite unsafe, they must be isolated from the chassis under operating conditions as described or assumed by many standards such as UL 2202, UL 2231, ISO 6469, J1772, and J1766. However, this clause is not strictly necessary during charging, because the charger's conductive coupling can be used to force both the chassis and the floated battery to safety ground. This could possibly relieve the charger power system from providing galvanic isolation to the battery, but also entails that the grounding conductor be oversized, while imposing strict safety regulation on all external wiring, connectors, and interlocks. Moreover, SAE J1772 calls for Ground Fault Detectors (or equivalent means) to ascertain the isolation integrity of the battery pack, making it impractical to assume that the battery pack could be anything else than fully floating at all times. The immediate consequence is that the charger must be designed to provide galvanic isolation from the AC line.

CHAPTER 3

PHOTOVOLTAIC SOURCE FOR CHARGING

3.1 POWER RATING WITH AVAILABLE OVERHEAD SPACE

Determining the nominal power level that should be made available at a charging station is an important step. Under average meteorological conditions, it is reasonable to expect that the PV resource will provide all the power demand from a discharged vehicle. This demand is limited by three main factors:

a)   The maximum safe charging current level for a specific type of battery pack;

b)   The current limit levels imposed or suggested by regulatory bodies, such as the National Electric Vehicle Infrastructure Working Council (IWC) or the NEC;

c)   The size and conversion efficiency of the solar panels.

The first criterion solely cannot be used as a deciding factor, given that battery packs are available in different sizes, capacities, and preferred charging algorithms. Although the third criterion deserves careful consideration, it is subjected to many variables relating to the design strategy for the charging station or carport. For instance, it will be demonstrated in this study (in section 3.2) that the solar resource for a given vehicle can double or triple, when neighboring stations become vacated and available. The analysis for the simplest configuration (a single PV string per station) is otherwise quite plain. It is expected that the PV string used for an average parking spot be of commensurate size to the parking spot itself, or about $15m^2$ in surface. For the purposes of a solar powered carport, however, it may be reasonable to presume that a larger surface would be available. For this study, a PV surface of $25m^2$ per vehicle is

considered. For mono-crystalline silicon, considering an optimistic cell efficiency of 20%, the maximum available power from the panels can be calculated, using the best-case insolation level of 1kW/m².

$$P_{PV} = 1kW/m^2 \cdot 25m^2 \cdot 20\% = 5kW \qquad (3\text{-}1)$$

In view of this objectively modest contribution from the PV resource, it seems that the second criterion is the most significant. The IWC and SAE J1772 have set limits for Level I and II charging, making it reasonable to assume that the station should be minimally rated for Level II charging. In the event that a larger power is required than that available at a given parking spot, there exist two options: either the grid is invoked, to supplement the demand, or the power from PV panels, assigned to other vacated parking spots, is redirected, as described in 3.2.

It is important to note that the value calculated for P_{PV} in (3-1) only represents a maximum or peak power output from the PV resource, obtainable only with advantageous meteorological conditions and during a fraction of the 24hr solar cycle. A more revealing number for this consideration is the average-day energy that can be converted by the panels. Although this quantity represents a power, it should be understood as the kWh energy delivered in a day period to a square meter surface. This value changes radically for different geographical locations, as illustrated in Fig. 3-1. The sample shown corresponds to various Canadian locations and is contrasted to data from the Virgin Islands, for the purpose of appreciating the sunlight deficit during the winter at higher latitudes. For instance, with a rather modest 3.89kWhr/m² per day delivered in March, in Ottawa, the 20% efficient, 25m² panel will deliver only 19.5kWh in an average

day. Thus, a 35kWh battery pack would actually require the full day (10.5hrs), in order to replenish from a 50% battery state of charge (SOC).
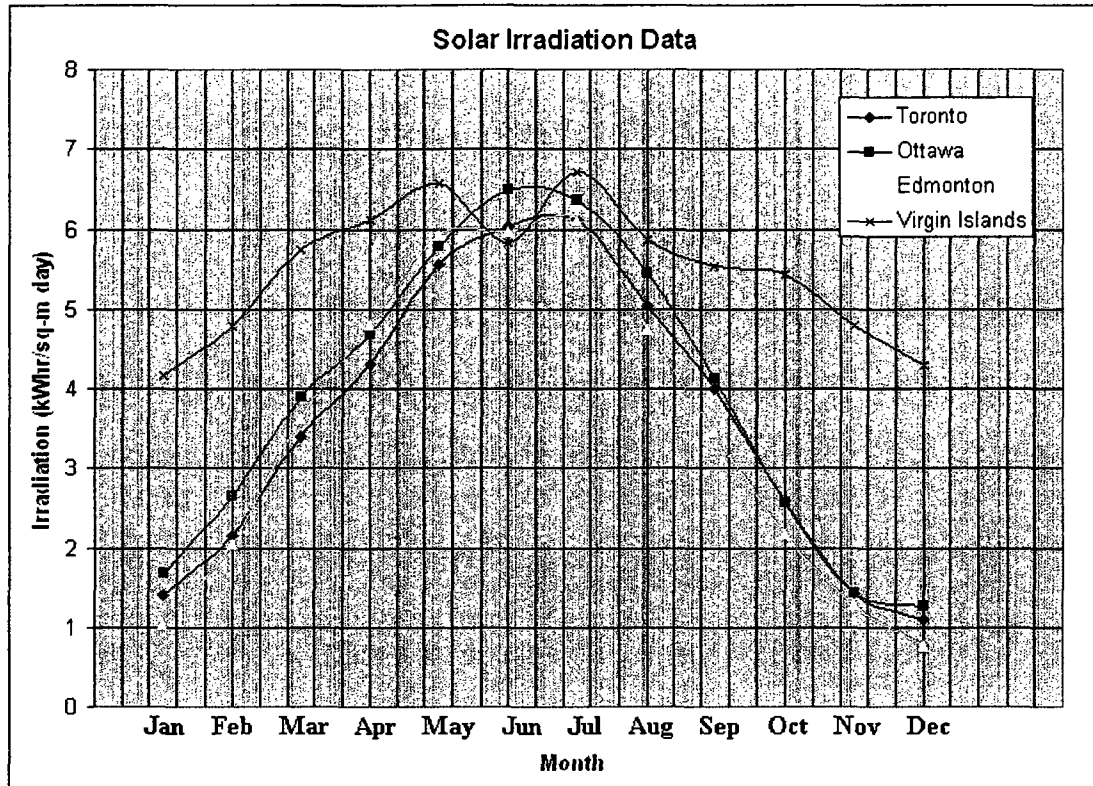
Fig. 3-1 Irradiation Data for Different Geographical Locations *

Information taken from http://energy.caeds.eng.uml.edu/fpdb/irrdata.asp

This result appears disappointing initially, raising doubts on the overall wisdom of this project, at least for higher latitude locations. Three aspects, however, must be kept in mind. Firstly, depending on the intended use, the carport may not be completely occupied. Therefore, several PV strings may be providing power to a single EV. Secondly, on an average, the battery SOCs of the vehicles will be presumably higher than 50%. Finally, slow charging has its own advantages, as mentioned earlier, especially when the user is utilizing the carport for long-term parking.

3.2 ARCHITECTURE

The configuration of the PV system is of critical importance, as it strongly affects

material and maintenance cost, reliability, availability, efficiency, safety, and

performance. Several studies have been conducted to describe various trends towards the

optimal architecture [4]-[6]. In older systems, such as the one used for the PIER carport,

in San Diego, CA (see Fig. 3-2), the panels are connected in series, in order to achieve

higher powers, by means of an increased supply voltage.
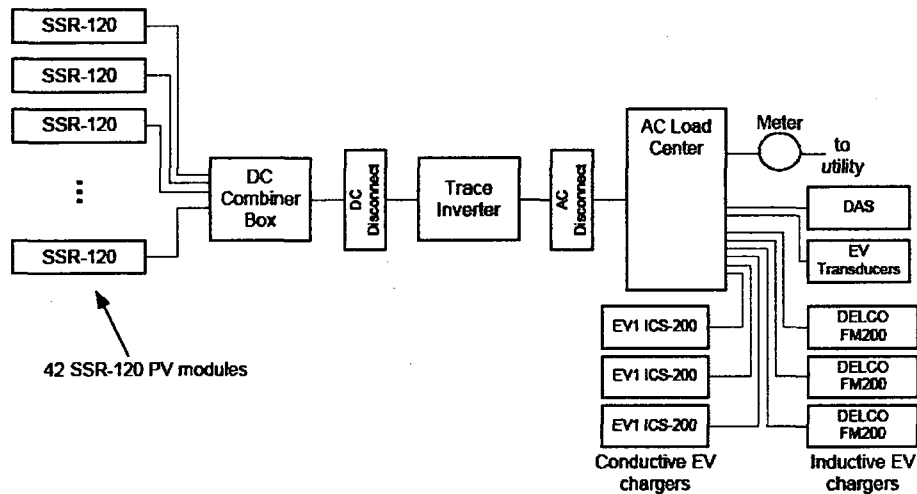
Fig. 3-2 Block Schematic of the PIER carport, San Diego, CA.

There exist several restrictions to this method, related to safety and semiconductor

capability, limiting the maximum number of series-connected panels for each string.

When larger amount of power is needed, the panels are usually connected through

breakers or fuses, to a DC combiner box. Due to partial shading effects, some strings can

deliver more power than others. However, the parallel connection of strings renders the

maximum power point tracking (MPPT) control impossible for individual strings.

Moreover, when one string produces more power than another, isolation diodes for each

string becomes necessary, further decreasing overall efficiency. Having all the power generated from a single source also suggests use of a large centralized inverter, for grid power generation. This is an added undesirable condition, because a single-failure results in a complete system shutdown. In addition, large-capacity power processors do not benefit from economies of scale and are often designed using naturally commutated devices at very low switching frequencies. The resulting power processor has high material and installation costs, low availability, and poor line-current quality; it should not be considered for modern installations. Fig 3-3 shows a general centralized carport application, such as the PIER carport.
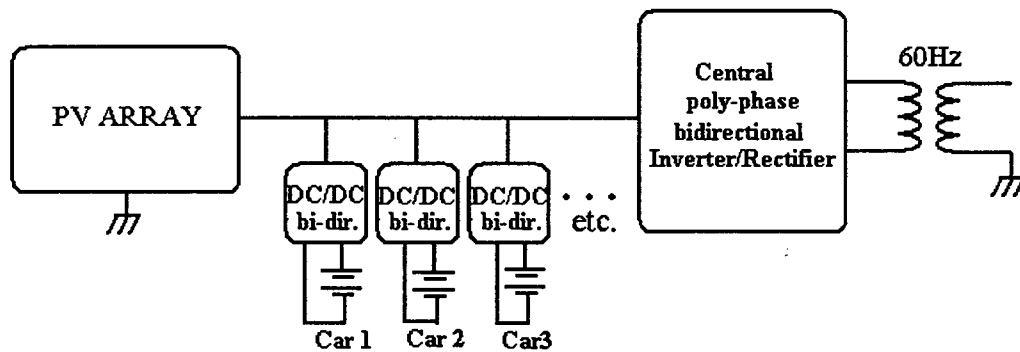
Fig. 3-3 Centralized architecture
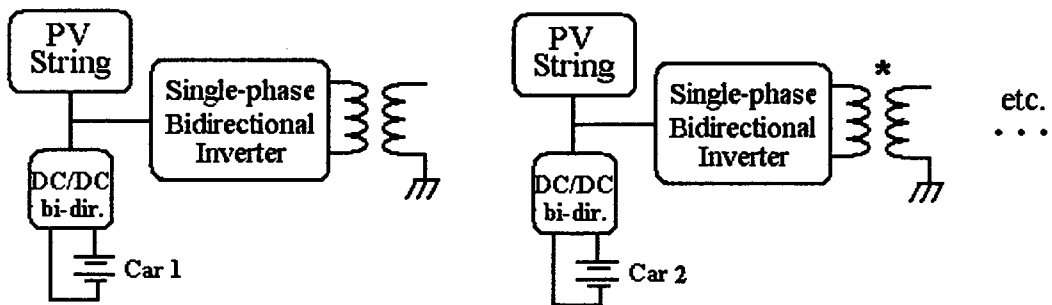
Fig. 3-4 Distributed architecture

The distributed architecture shown in Fig. 3-4 is more promising. The inverter stage is distributed and so is the PV resource. Both can benefit from economies of scale and no single point of failure exists. Furthermore, the inverter can be a single-phase HF type for high power quality flow to the line. The double conversion stage between battery and grid remains problematic. The options shown in Fig. 3-5 are similar to the previous architectures, except that they possess few additional possible advantages.
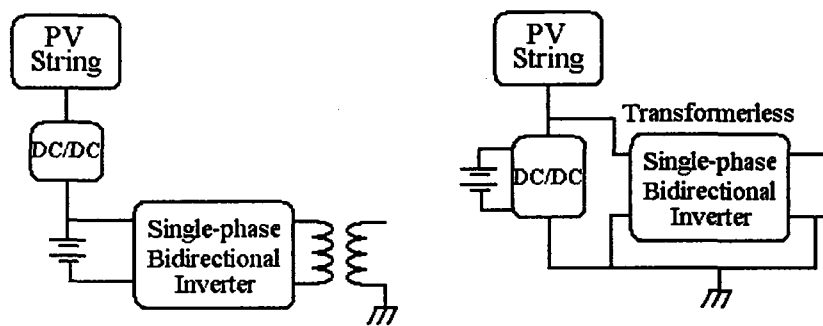
Fig. 3-5 Improved distributed architectures

On the left of Fig. 3-5, the DC/DC MPPT stage need not be bi-directional. However, an extra conversion stage is now added in the critical power flow path PV-to-grid. The configuration on the right shows an arrangement that allows the use of a transformer-less inverter topology. In either case, each PV string possesses its own MPPT converter that can feed data to a central computer, for the purpose of evaluating, which strings are underutilized. Thus, a fully distributed architecture can be exploited to optimize energy flow from the PV source to the battery; representing the most critical power flow path. A straightforward example of this concept is shown in Fig. 3-6, which takes the form of a simple contactor matrix that can connect any PV string to any other, using only two contactors per charging station.
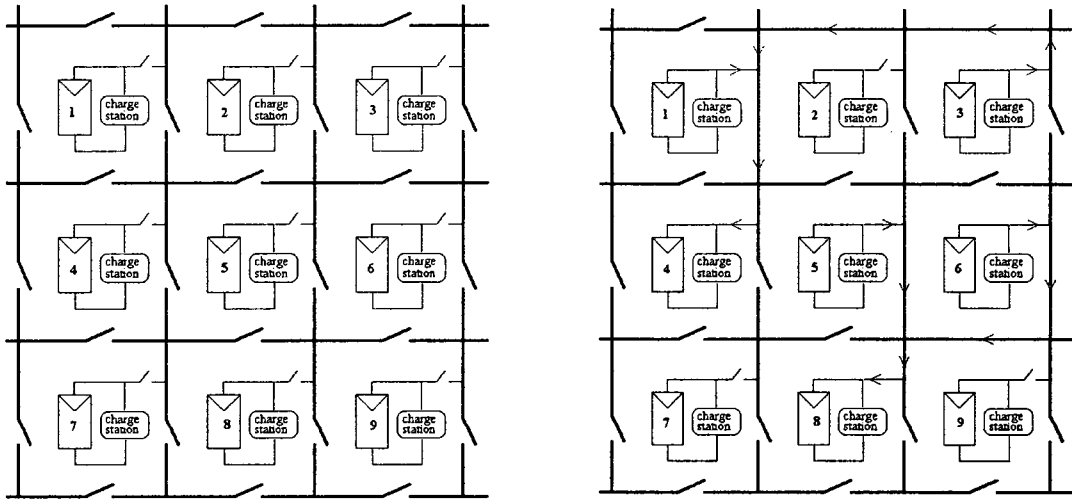
Fig. 3-6 Contactor matrix for PV resource management

The arrangement on the right, in Fig. 3-6, shows how vacated charging stations 1 and 3 are connected to 4, while vacated stations 5 and 6 are connected to 8. Different contactor configurations are obviously possible; however, they are not addressed in this study. It is simply important to realize that the nominal assignment of a PV string to a single charging station does not necessarily entail a compromise on energy availability to the EV/PHEV.

3.3 VOLTAGE

Peak voltage from each string is limited by safety considerations to 600V, in order to stay clear of added costs for specialized cabling and other accessories. NEC 690 specifies maximum voltage as the open-circuit voltage obtained at the lowest expected panel temperature. On the other hand, lower level of voltage range is determined by design considerations. The conversion systems shown in Figs. 3-4 and 3-5 can be studied individually for this purpose. When an isolation transformer is present in both the DC/DC

converter as well as the inverter, very little restriction is placed on the choice of nominal PV voltage. In fact, the chosen topology for the power inverter/rectifier can be buck, boost, or buck-boost, and therefore, the PV voltage can be chosen accordingly. This is not the case shown in Fig. 3-5 (right), which is complicated by the fact that the line is directly connected to the inverter. As voltage fed inverters are naturally of the "bucking" type, it appears that the minimum voltage output of the PV resource should be higher than the maximum expected grid peak voltage. For Level II charging, a 240VAC nominal line, with a maximum peak voltage of 360V, is assumed. The PV resource should then be disabled or unloaded, when its output voltage decreases below this level.

Calculation of PV nominal voltage is straightforward. For varying MPP levels and temperature, the PV panel output voltage will be coarsely constant. The variations of the MPP, due to insolation and temperature, are considered as $\pm$ 5% and $\pm$ 12%, respectively (from -20 °C to 65 °C, using standard 0.28% per °C, for PV cells), for a total of $\pm$ 17%. Therefore, for a minimum voltage of 360V DC, nominal PV voltage is 430V DC, and the maximum is 500V DC. The open circuit voltage of the panel is typically considered as 20% higher than the loaded voltage (600V). This voltage corresponds to an absolute maximum, at light load and minimum temperature, which is at the safety limit. Therefore, the PV will be optimally rated at –20 to +65 °C, with a nominal operating voltage of 430V DC $\pm$ 70V DC.

3.4 SAFETY

Safety issues related to PV grid-tied systems are extremely diverse and are dealt differently in different parts of the world, and even within the same country, depending on the standard followed. Furthermore, at least currently, the North American utility

companies seem to hold more influence on design decisions, contrary to the reports proposed by the NEC, UL, and ISO. The main contention is whether one of the PV panel string live conductor should be grounded or not. Traditionally, in North America, this practice was universally accepted and is still largely preferred. However, the NEC recently allowed panel conductors to be floating, as long as certain conditions are met. This affords the designer of the inverter the possibility of using transformer-less connections to grid, as is now widely done in Europe. Nevertheless, the lack of galvanic isolation also raises the possibility of DC current injection into the grid distribution and its associated issues. The main reason that PV live circuits were initially required to be grounded was because of the connection to the downstream inverter. In fact, an ungrounded panel could be driven with both 60Hz and high switching frequency components by the inverter's commutating action. Unfortunately, the surface of the panel itself is not completely isolated from the live panel conductor, and can in fact, exhibit several hundreds of pico-farads under dry conditions, and much more in wet conditions. Therefore, the leakage current from the panel surface can potentially generate a shock hazard. It is up to the designer to conceive an inverter topology that does not generate large common mode voltage at the PV power conductors.
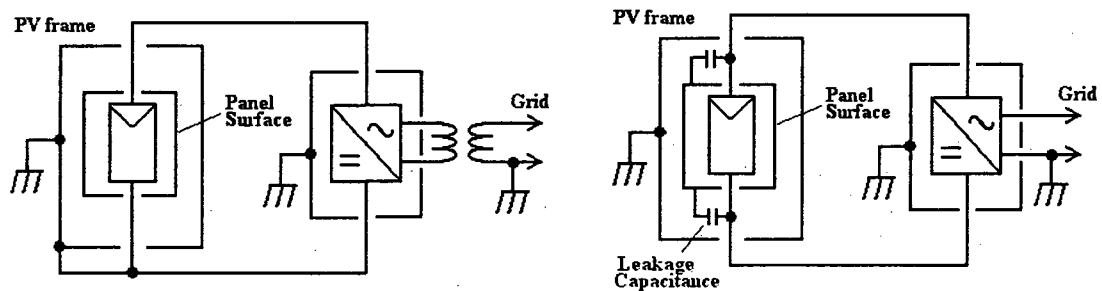
Fig. 3-7 Grounded, galvanically isolated system (left). Ungrounded, transformer-less system (right)

In this thesis, it is assumed that the grounded system will continue being the accepted norm in North America, and all three topologies analyzed will reflect this choice, although one of the three will indeed still be transformer-less.

CHAPTER 4

GRID CONNECTION ISSUES

4.1 LINE STABILITY ISSUES

As aforementioned in the introductory chapter, the grid could perform the function of "storing" excess energy produced by the PV resource of the carport, thus eliminating the need for local storage (batteries and flywheels). In fact, the scenario is somewhat more complicated than that. It is well known that intermittent generators, such as solar and wind installations, can potentially cause problems to the grid. In fact, should these generators become very widespread, or be connected to remote locations on the grid; the energy they produce may exceed the available load. Simple energy conservation theory dictates that such a condition is untenable and must be remedied either by storing the energy for later use or by decreasing power generation, thus underutilizing the generator's capacity. Even when produced energy is not in excess, the flow of current, back towards the power substation can cause the local point of common coupling to experience a voltage boost that can be severe when line impedance is significant.

Furthermore, and especially in the case of PV sources, the instantaneous level of generated power can experience rapid variations (up to 15% per second, due to clouding) that cannot be compensated in real-time by the grid, thus causing voltage flicker. These serious issues concerning distributed generation are presently the object of intense study and mobilization by public and private parties and will not be addressed in this thesis. Nevertheless, it is important to consider the following points:

1)   Present grid penetration levels of distributed systems, in general, and photovoltaics, in particular, are very low, less than 2-3% in North America. Several studies referenced in [7] have established that flicker and voltage boost are significant only when the penetration levels at the power sub-station are more than 5% and 15%, respectively, in most cases.

2)   In the case of a carport, the load is intrinsically a storage type; EV/PHEV batteries. In other words, especially for large carports, there is a statistically high probability that the storage and the load are one and the same. Scenarios involving an empty carport and overproduction occurring simultaneously can be deemed so rare that decreasing production in such instances would be fairly acceptable. In fact, grid-connected EV/PHEV batteries could be beneficial to the utility company for the reasons mentioned in the introductory chapter.

4.2   INVERTER DISTORTION AND DC CURRENT INJECTION

As the PV resource generates DC voltage, an inverter is needed in order to connect to the line. Several regulatory agencies, such as UL and IEC, have imposed common specifications for inverter performance. Minimally, the inverter must produce low harmonic distortion currents (less than 5%) and near unity power factors (displacement PF compensation is not yet allowed in most cases). Furthermore, the inverter is not allowed to inject a DC current component into the grid, as this could cause distribution transformers to saturate. Commonly followed standards IEEE 929, IEC 61727, and EN 61000 specify between 0.5% and 1% of rated output current as a maximum, while some national European standards add a 5mA absolute requirement in addition to this minimum percentage.

4.3 LOCAL DISTRIBUTION CONFIGURATION

As a final note, the solutions considered in the previous sections assume the use of single phase connections. The main appeal of the 3-phase system is the enhanced power capacity, the fact that this power is delivered and absorbed without any line-frequency components, and the elimination of 3rd harmonic currents in the distribution and grounding wiring. These features are quite attractive and include the advantage of potentially eliminating undesirable pulsating charging current to the EV battery. On the other hand, the single-phase configuration allows for less expensive and simpler distributed inverters. Especially considering the fact that PV can only provide 5kW of power to the inverter, and that intervening DC/DC converters need to be added to can eliminate any pulsating current, it appears that a single-phase system is much better adapted to this application and will be assumed throughout this study.

CHAPTER 5

POWER ELECTRONIC INVERTER TOPOLOGIES

5.1 INTRODUCTION

When defining the technical goals for a distributed power converter system to be used in a PV-powered, grid-tied carport, suitable compromises must be made, in order to contain costs while providing acceptable performance. Essentially, the main design objective is dictated by the fact that the carport will be a public or semi-public structure. Hence, it is crucial that the system is robust, reliable, and offers high availability. It was already ascertained that both the PV resource and the power conversion system must be distributed, providing flexibility and redundancy, while choosing topologies that are characterized by low component count and stress levels, in order to ensure a high Mean Time Between Failures (MTBF). MTBF will broadly be referred to as "reliability" henceforth, in this thesis.

Another important consideration is that renewable resources are not easily harnessed. This simple fact makes energy conservation through high conversion efficiency a priority. As mentioned above, the number of conversion stages should be minimized, at least for the most utilized power flow paths. In the case of a carport, the power will flow most frequently from the PV array to the EV battery and from the grid to the EV battery. Therefore, given a choice, the flow paths should be optimized in line with the following priorities: in decreasing order of importance, array to battery, grid to battery, array to grid, and battery to grid. A schematic, showing possible power flow paths is depicted in Fig. 5-1.
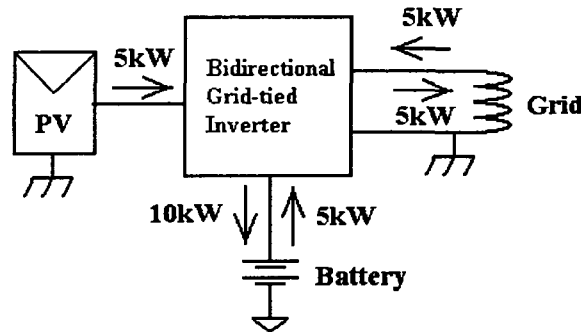
Fig. 5-1 Possible power plow paths with specified power level

Finally, it is reasonable to expect that the initial cost penalty would be more than offset by a design that is intrinsically low-maintenance, considering the application. This goal can be achieved by avoiding or minimizing the use of short-life components, such as electrolytic capacitors, electromechanical devices (relays, fans, and power connectors), and fault detectors or suppressors (MOVs and GFID). In addition, the control scheme should be robust and rely as little as possible on critical sensing devices that have time stability limitations or require periodic calibration. These include thermistors, shunt resistors, hall-effect devices, and linear opto-electronics.

Having established the general design philosophy, the detailed specifications for the power conversion system, as have emerged in the discussion earlier in this study, are summarized here:

PV panel string peak power: 5kW
PV panel voltage range*: 430VDC±70V on full temp. range and 10-100% insolation
PV operating temperature: -20 degC to 65 degC
PV grounding required at either power conductors or as a center-tap
Grid nominal voltage: Single-phase 220-240VAC
Grid nominal current: 25A
Current distortion: < 5%
Power factor: Unity
Charger voltage range 275V to 400V (galvanically isolated)
Charging Power 10kW max
Discharging Power 5kW

The specifications shown above indicate a desirable range, as they guarantees a higher than line peak voltage for a transformer-less topology. The specifications also indicate the highest practical voltage allowed by code; of course, a higher voltage implies less cabling loss and higher efficiency.

5.2 PROPOSED POWER CONVERSION TOPOLOGIES

From the foregoing discussion, it appears that the ideal power processor would only have a single conversion stage between all power ports (i.e. the PV, the inverter, and the EV battery). Furthermore, the power processor would also handle two DC levels simultaneously (EV battery and PV) and permit bucking and boosting to and from the grid. The Z-source/loaded converter (Z-converter) is known to possess all these attributes and will, therefore, attract most of the attention in this thesis; it will also be the first topology to be analyzed in detail. The Z-converter will be compared to another class of power processors that allows utilization of dedicated converters for the grid as well as the battery that can be isolated using small and highly efficient HF power transformers.

Safety and current shaping issues are easily resolved. However, the higher component count of the circuit can affect reliability. Finally, a third type of power processor will also be considered for comparison purposes. This third circuit represents the transformer-less topology; it allows direct connection to the grid distribution transformer without intervening isolation. However, the transformer-less topology is still not popular in North America, despite its broad acceptance in Europe. The good safety record of the transformer-less option in Europe, coupled with the objective advantages in the areas of cost and efficiency, will more than likely ensure its adoption worldwide. These topologies are simpler and more efficient than the previously discussed topologies.

Nevertheless, they demand the use of sophisticated and precise control circuits, to avoid DC current injection onto the grid. In addition, safety requirements are more stringent for all the major components (panels, EV battery, and inverter). Although European standards do not require a ground on the PV string, the topology presented in this study has one, in order to satisfy the specifications.

For all topological options, the switching frequency is considered as 25 kHz. This choice allows the use of a fast IGBT technology, which is demonstrably better suited for power levels in the required range. Furthermore, given that physical size is not a priority for this application; higher frequency operation could be needlessly wasteful.

5.3 THE Z-CONVERTER

5.3.1 Background

The use of the Z-converter AC power absorption/injection, with simultaneously controlled battery charging, has been successfully demonstrated in literature [8]. The AC source/load could comprise of an EV electric machine, while the DC source could comprise of a fuel cell. The same concept can be extended to PV grid-tied systems. The grid-tied system, on the other hand has fewer degrees of freedom, because of two main reasons. Firstly, in the case of the fuel-cell-battery HEV described in [8], the battery pack is native to the system, and therefore, its characteristics are fully known. In the case of a PV grid-tied carport, the PV and grid resources are expected to function with widely different battery technologies and characteristics. Secondly, the electric machine, used in [8] can be managed by the vehicle controller, while the grid behavior is an external variable. On the other hand, in the case of the PV carport, the EV battery will need to be

isolated through a transformer, so that the turns-ratio can provide added flexibility. The schematic of the Z-converter system is shown in Fig. 5-2.
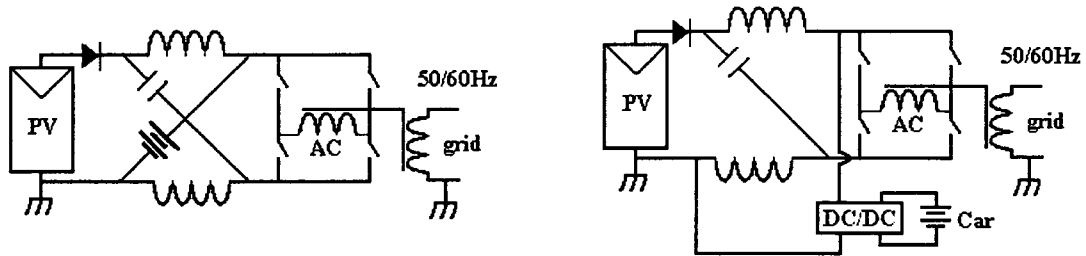
Fig. 5-2 Non-isolated grid-tied Z-converter (left); Grid-tied Z-converter with Isolated Charger (right)

It is important to realize that the DC/DC converter was added to the original design, in order to solely provide galvanic isolation. In fact, the Z-converter possesses double modulation capability, and can shape the grid current while simultaneously regulating EV battery charging. This goal is achieved with a single conversion stage and can be considered as the main advantage of the Z-converter. An added advantage is the inherent buck-boost capability of this topology. However, given the presence of the isolation transformers to the grid and EV battery, this benefit is marginal in this application. Some of the drawbacks include:

a)   An outsized 60Hz transformer is required, because a large common mode voltage would otherwise exist at the PV modules, making it impossible to meet leakage current specifications. A central 60Hz transformer can possibly be used, to service all charging stations. Nevertheless, the single point of failure in this case would not be desirable.

b)   Single-phase power is delivered and absorbed in 120Hz sinusoidal pulses. Because of the single stage of conversion, this power ripple must be stored at some point

26

in the circuit. As the EV battery is by far the largest dynamic repository of energy in this circuit, it is likely to absorb most of this ripple. In fact, in the case of full PV production into the grid, the battery would not only experience AC current alone, but its amplitude would also be very large. As disturbing as this may appear, such an approach will be considered and even encouraged at times, because it allows the elimination of an additional large decoupling capacitor across the PV panels, improving cost and reliability. At the same time, the concern about the AC component can be rationalized in several ways. For instance, whenever PV production exceeds the demand of the battery, the local MPPT system can be bypassed, so that excess power is redirected to neighboring charging stations. This would not eliminate the ripple, but would at least avoid battery current reversal at line frequency. Otherwise, it could be assumed that future EVs will draw their energy from ultra-capacitor banks that are ripple-tolerant, rather than electro-chemical devices. In either case, it is practical, that by storing the ripple in the battery by control methods is more complicated than simply introducing a large decoupling capacitor across the PV source. This method will therefore be considered, by default, in this thesis. Later, it will also be demonstrated that the ripple can easily be redirected from the battery to an added decoupling capacitor, if the design demands this requirement.

c)   In order to address the ripple problem more clearly, an additional DC/DC converter can be utilized in conjunction with the EV battery, to regulate the 120Hz out of the charging current, with minimal decoupling. While this approach works in theory, it will require an added controller and the conversion efficiency may be reduced. In fact, the DC/DC converter would now have to be considered a second full conversion stage.

This defeats the stated main advantage of the Z-converter and will only be considered briefly in 6.1.6. Therefore, no attempt will be made to completely eliminate this problem; rather, the 120Hz ripple is accepted for this topology and will be managed using innovative techniques. These techniques involve modulation of the shoot-through duty cycle, D_o, with the intended purpose of directing the ripple either into the EV battery (or Z-circuit capacitors, when the battery is not connected) or into an added decoupling capacitor across the PV source, depending on the design requirements.

5.3.2 Static Design Equations and Control Scheme for the Z-Converter

The analysis of the operation of the bi-directional Z-inverter has been presented in [2], [9], and will not be repeated here. The only new addition is the DC/DC isolated converter needed for safety, as shown in Fig. 5-3.
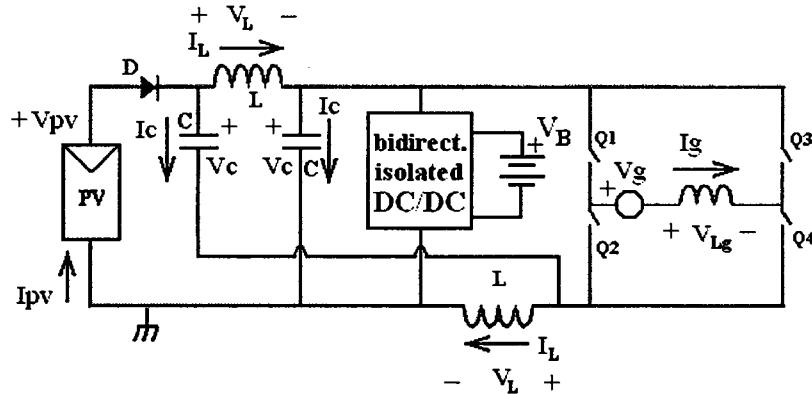
Fig. 5-3 Z-converter with added isolated DC/DC converter

In order to maximize efficiency, this added bidirectional converter is normally operated at 100% duty cycle in open loop. Therefore, when in normal operation, the voltage V_B is identical to voltage V_C, except for the static gain of the DC/DC converter. When no battery is present, and the PV feeds the grid with full available power, this

28

converter does not operate, and appears as an open circuit. The three main static equations are derived in [2], and are re-stated below:

$$Vg_{(PK)} = V_C \left(\frac{D}{1-Do} \right) \tag{5-1}$$

$$Do = \left(\frac{V_C - V_{PV}}{2V_C - V_{PV}} \right) \quad \text{or} \quad V_C = V_{PV} \left(\frac{1-Do}{1-2Do} \right) \tag{5-2}$$

$$I_L = \frac{D}{1-2Do} I_{IN} \tag{5-3}$$

Here, D is the modulation index or active duty cycle; D_o is the shoot-through duty cycle. Eq. (5-2) is written in two ways. The first is more applicable when a battery is connected. In this case, the battery stiff voltage at V_C is independent of D_o. Rather, D_o depends on V_C. When the battery is not present, the DC/DC converter is replaced by its input capacitor alone. In this case, the capacitor voltage V_C depends on D_o, as shown in the second variation of (5-2).

Unfortunately, the validity of these equations is subject to strict operational conditions. In the first place, the circuit variables must be static or slow-changing. However, contrary to 3-phase systems, in 1-phase systems, the power is delivered to the load in a sinusoidal fashion. This causes substantial 120 Hz ripple on the Z-circuit components, and hence, static behavior within a cycle cannot be claimed. Secondly, the switching pattern, topology, or the operating point must be such that several undesirable conversion modes are avoided or contained. These are described exhaustively in [10], [11]. This scenario can be briefly explained here, as modes that cause either the diode, D, to turn off prematurely, during the active state, or the inverting bridge to short at the beginning of the active state, thus adding an un-programmed shoot-though sub-period.

These modes, in conjunction with discontinuous conduction mode (DCM) conditions, at low AC loads, can cause the capacitor voltage to float much higher than that predicted by (5-2). However, the voltage rating of the capacitor must be kept as low as possible, in order to allow use of low-voltage semiconductors. A reasonable approach to this problem, as described in [11], proposes the use of a switch in place of diode D. The idea is to block conduction only during programmed shoot-through sub-periods, while allowing reverse current under all other conditions. The subsequent revised topology is shown in Fig. 5-4.
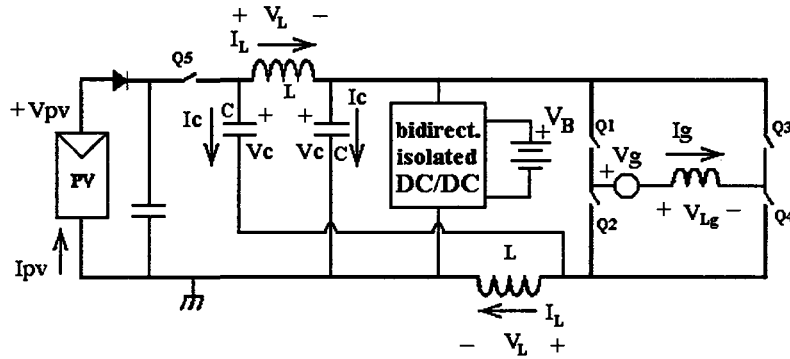
Fig. 5-4 Modified Z-converter topology to avoid undesired capacitor voltage boost

It is worth noting here that the added diode would be needed anyway, in order to allow connections of adjacent PV panels. Furthermore, the added capacitor would also be needed, in order buffer high frequency current from the PV panel and decouple the converter locally; its size depends on whether it will also be used to decouple the grid AC power, as discussed earlier.

Equations (5-1) and (5-2) show the two variables, D and D_o, that control the grid and battery power flow, whereas the total power flow is controlled by the PV panel MPPT function. A simplified block diagram of the control system is depicted in Fig. 5-5. The PV MPPT will determine the appropriate current that should be drawn from the

panels and generate a reference signal. This reference is compared to the measured PV current, and an error is generated, that represents the reference to an internal current loop. The controlled current in this case is the grid line current, whereby the grid current request will change with the MPPT request. At the same time, the EV on-board charge controller sends a current level request, which is a reference for the average battery current. This signal will be a DC signal in steady-state. However, the actual battery charging current could have a sizeable AC component at line frequency. The error between requested and actual charge current produces the control signal D_o.
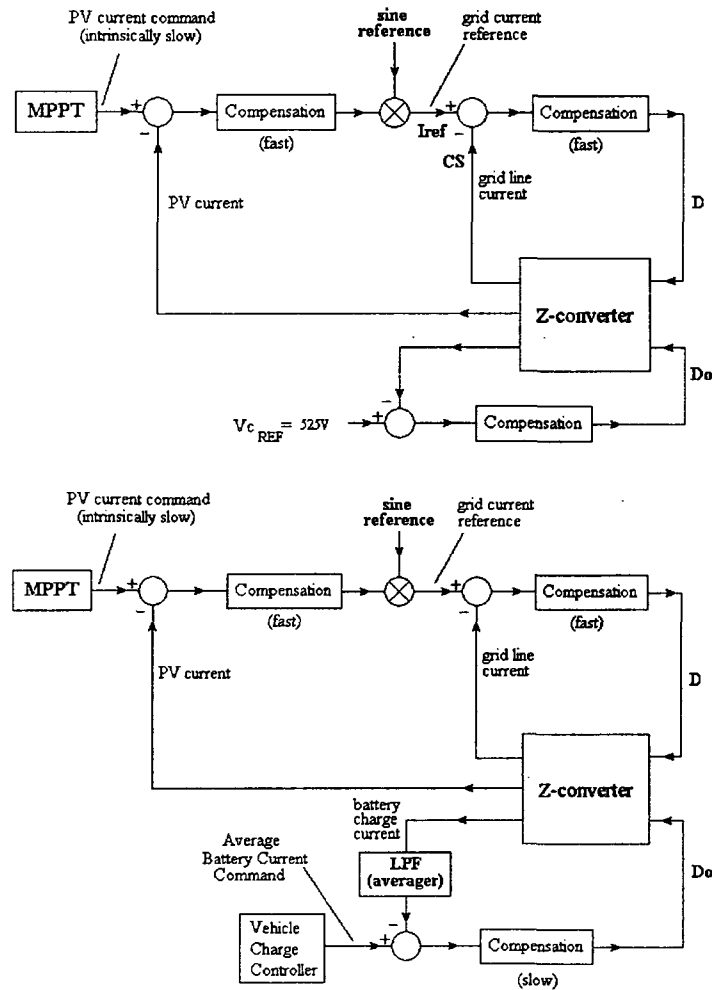
Fig. 5-5 Control strategies: With no battery (top), With battery (bottom)

31

Fig. 5-5 also shows the control strategy in case there is no battery connected. The converter acts as a simple grid-tied inverter, and the modulating signal D_o is simply utilized as a means to regulate the capacitor voltage, at 550V. This voltage level allows the use of commercially available high efficiency IGBTs rated between 900V-1200V, for the inverting bridge. It must be noted that, although the specified PV voltage range does not allow the use of more efficient 600V devices, the Switch Utilization Ratio (SUR) for the Z-converter is still high compared to alternate topologies (see 7.1).

5.3.3 Design of the Isolating Bi-directional DC/DC Converter

Fig. 5-6 shows the evolution of the Z-converter, from having the battery connected directly, in lieu of one of the Z-circuit capacitors having an intervening isolating DC/DC converter. In both cases, the Z-circuit is no longer balanced and/or symmetrical. Although this scenario does not preclude acceptable operation, the presence of the converter allows the possibility of restoring symmetry. Fig. 5-6 demonstrates this design aspect.
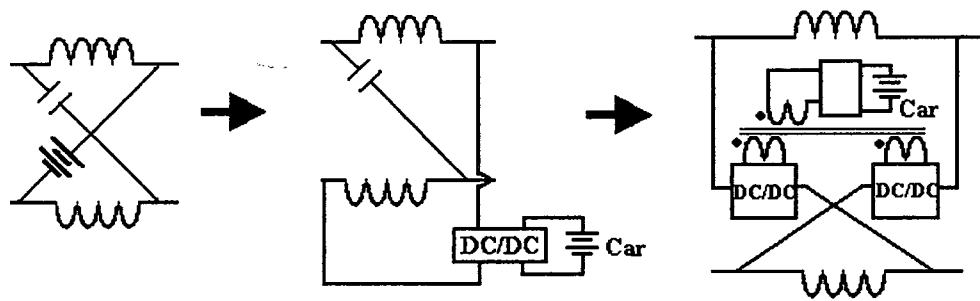
Fig. 5-6 Evolution of Z-circuit: Non-isolated (left), asymmetrically isolated (center), proposed symmetrically isolated (right)

This novel circuit topology adds a DC/DC converter with split primaries on the isolation transformer. However, a single secondary drives the EV battery, as depicted in

32

Fig. 5-6. Two sets of primary switches are required. The switches conduct half of the current and can be sized accordingly. Also, because the converter operates at full duty cycle in open loop mode, very high efficiencies are obtainable by the use of simple soft-switching techniques, and various topologies, with similar costs and performance can be proposed to implement them. For the purpose of obtaining quantitative data, one such topology is proposed and analyzed without further justification, as long as it is made clear that other topologies can be substituted for this function. The chosen topology is shown in Fig. 5-7 and is based on using two half bridges, operating at a high frequency.
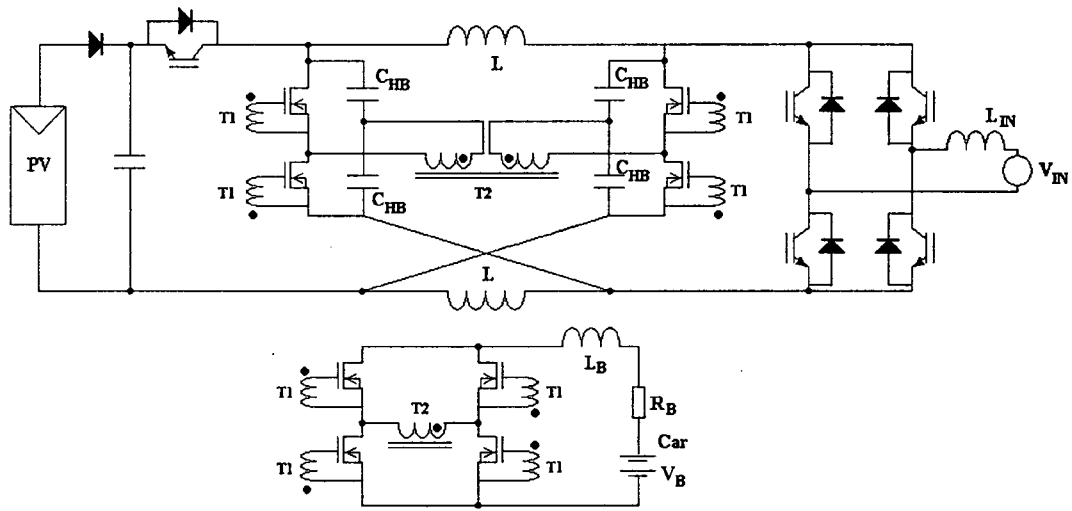
Fig. 5-7 Evolution Complete detailed schematic for Z-converter including symmetrical DC-DC isolating converter

The converter of Fig. 5-7 uses 8 switches, with very low current and voltage ratings. However, different versions could use only 6 switches (or even 4), rated for higher voltages. Furthermore, as compared to popular push-pull topologies, the half-bridge topology does not suffer from transformer saturation, when operated in open-loop full duty cycle, and has inherent zero-voltage switching (ZVS).

Despite the high number of MOSFETs, a single gate drive transformer can drive all switches simultaneously. In addition, there is no need to add two separate half-bridge capacitors. In fact, because of the required CV product, the Z-circuit capacitors are of the electrolytic type, which are commonly available with a 450V maximum rating. Hence, two series capacitors must be used, given that the overall capacitor voltage can be expected to be higher than 600V. Therefore, besides the high number of switches, the DC/DC converter can be kept compact. The operation of the half-bridge topology is well known and will not be addressed here. Nevertheless, the transformer turns ratio needs to be calculated and the equivalent average model obtained.

5.3.4 Calculation of the Turns Ratio

It is critical that the transformer turns ratio be kept to a minimum, in order to maintain the reflected battery voltage as low as possible, allowing the use of efficient devices. However, when the battery has low voltage ($V_{B(min)}$ = 275V), the reflected voltage must still be higher than the maximum PV voltage ($V_{PV(max)}$ = 500V). Thus, the turns ratio from each primary to the secondary winding is calculated as, $N = \dfrac{V_{PV(max)}}{2V_{B(min)}} = \dfrac{10}{11}$

where the factor of 2 is generated by the half-bridge operation. A ratio of unity will be adopted here for two main reasons: first, the half-bridge, operated in soft-switching mode, does not feature a perfect 100% voltage transfer, due to the presence of parasitics. Secondly, a 1:1 ratio is optimal, because it allows all three windings to be arranged in tri-filar configuration 'in the transformer, reducing leakage inductance to a minimum. The maximum voltage on the Z-circuit capacitors can now be calculated with $V_{B(max)}$ = 400V

and N=1. Hence, $Vc_{(max)} = 2N \cdot V_{B(max)} = 800V$. Thus, 900V MOSFETs must be used in the primary circuit, while 500V MOSFETs can be used in the secondary.

5.3.5 Derivation of the Equivalent Average Circuit of the DC/DC Converter

Each primary of the transformer can be simplified, as shown in Fig. 5-8. The average transformer current over one cycle can be considered zero, while the average current into the MOSFETs is ¼ I_{LB} (50%, due to the parallel primaries sharing current, and another 50%, due to the duty-cycle). The average rectified secondary voltage is 50% of V_C. Hence, the derived average model is straightforward, and is shown in Fig. 5-9.
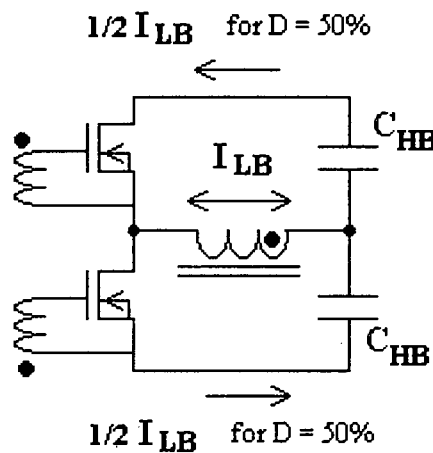
Fig. 5-8 Primary circuit for DC-DC section
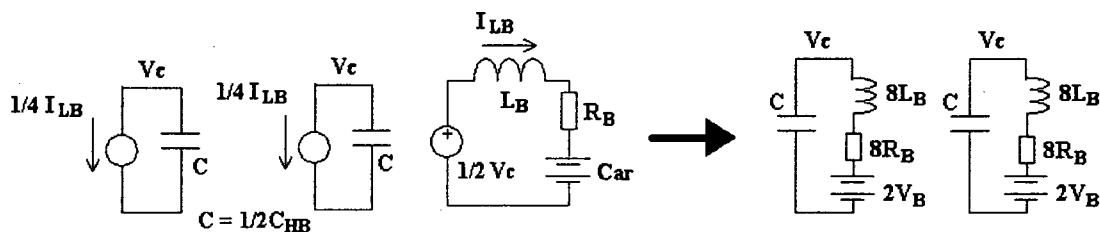
Fig. 5-9 Derivation of the average model for the DC-DC converter

Thus, the DC/DC converter and battery load can simply be modeled as a parallel branch on the Z-circuit capacitors, as shown in Fig. 5-9. APPENDIX A provides a detailed derivation of the equivalent battery circuit model.

5.3.6 Design of the Z-Circuit: Capacitor

The Z circuit includes two capacitors and two inductors. The main function of the capacitors is to store and release reactive energy from and to the grid, when the EV battery is not connected. In this case, the PV cannot provide the sinusoidally pulsating power, leaving this task to the capacitors, since the inductors do not store appreciable energy. The voltage ripple at line frequency must be kept low, in order to reduce voltage stresses and allow proper operation of the inverter. A peak-peak ripple of 10% is common for electrolytic capacitors at line frequency and will be adopted for the design. In order to calculate the ripple, it is necessary to determine the maximum levels of power flow in and out of the grid. The PV resource will provide a maximum of 5kW. Thus, the inverter should be designed to allow this power to access the line. For optimal sizing of the inverter semiconductor devices, this should also be the amount of power that can be drawn from the line, so that a maximum of 10 kW can be used to charge the battery, if both the grid and the PV resource make their maximum contribution (see Fig. 5-1). From these considerations:

$$Pg(t) = P_{PV}[1 + \sin(2\omega t)] \quad \text{and} \quad Pc(t) = \frac{P_{PV}}{2}\sin(2\omega t)$$ where the factor of 2 is added

given that there are two capacitors in the Z-circuit.

$$Pc(t) = Vc(t) \cdot i_C(t) = Vc(t) \cdot \frac{dVc(t)}{dt} C = \frac{P_{PV}}{2}\sin(2\omega t) \; ; \quad \text{hence:}$$

$$\int_{V_{low}}^{V_{high}} Vc(t)\,dVc = \frac{P_{PV}}{2C} \int_0^{\frac{\pi}{2\omega}} \sin(2\omega t)\,dt$$

or

$$\frac{1}{2}Vc^2\bigg|_{V_{low}}^{V_{high}} = -\frac{P_{PV}}{4C\omega}\cos(2\omega t)\bigg|_0^{\frac{\pi}{2\omega}} = \frac{1}{2}(Vhigh - Vlow)\cdot(Vhigh + Vlow) = \frac{P_{PV}}{2C\omega}$$

(Vhigh-Vlow) is the peak-peak capacitor ripple voltage ΔV_C, while ½ (Vhigh+Vlow) is the DC component of the capacitor voltage V_C.

Hence: $\Delta Vc = \dfrac{P_{PV}}{2Vc\cdot C\omega}$ (the worst case) occurs when the DC component Vc is minimum. However, the capacitor voltage is regulated at 550V, and therefore, the target ΔV_C is 55V. With P_{PV}=5kW and ω=377 rad/sec, a ΔVc of 55V necessitates a minimum capacitor C=220μF. Considering tolerances and margins, a nominal value of 470μF is reasonable. The capacitor current will be $Ic = \Delta Vc \cdot \omega C$, which computes to Ic = 4.54A peak. Note that the value for calculated I_C does not include switching frequency ripple from the inductors in the Z-circuit. Rather, this includes only the line frequency component. The voltage rating for the capacitor is determined by considering a connected EV battery, with maximum rated voltage of 400V.

5.3.7 Design of the Z-Circuit: Inductor

The high frequency ripple current is generated during the shoot-though switching interval, when the full capacitor voltage is impressed on the inductors. The maximum ripple current is thus obtained for the widest shoot-through duty cycle, D_o, and maximum value of V_C. Maximum duty cycle, D_o, is obtained for minimum V_{PV} = 360V. From (5-2):

$$Do_{(MAX)} = \left(\frac{Vc_{(max)} - V_{PV(min)}}{2Vc_{(max)} - V_{PV(min)}}\right) = \left(\frac{800V - 360V}{1600V - 360V}\right) = 0.355$$

37

The limit on the switching ripple current on inductor L represents a somewhat flexible design choice, as the ripple is absorbed within the Z-circuit, and only has a moderate effect on the output quantities. Furthermore, the issue of DCM avoidance is managed by the use of the bi-directional switch in place of the diode. Possible limits on the ripple are current capability of the Z-circuit capacitors, the saturation level of the magnetic material used for the inductors, and additional conduction loss in the semiconductor devices. However, a small L is preferable, in order to reduce the quality factor, Q, of the Z-circuit, for easier loop compensation (see 5.3.8.1). Therefore, an RMS current of 5A is a reasonable choice, based on typical performance of high-voltage electrolytic capacitors. This corresponds to $\Delta I_L = 17.3A$ for triangular wave-shapes.

The maximum ripple is: $$\Delta I_L = \frac{Do_{(max)} \cdot Vc_{(max)}}{F_{SW} \cdot L}$$ Hence: L = 650μH

5.3.8 AC Analysis of the Z-converter

The Z-converter must be well understood in its AC behavior, in order to justify the choice of the power components, especially the inductors and capacitors. Moreover, in this application, the converter will have different operating regimes, corresponding to 3 distinct cases (PV to Grid with battery, PV to Grid no battery, and Grid to/from battery).

As will be seen, the full control system consists of as many as 4 control loops: these are the input current control loop, the MPPT PV current control loop, the I_B or V_C control loop (depending on the presence or absence of the battery), and, optionally, the current ripple reduction control loop. The analysis of all these loops is complicated by the fact that this is a MIMO system with two coupled control variables D and Do and two controlled outputs (grid current I_{IN} and charge battery current I_B or capacitor voltage V_C).

38

Reference [9] provides useful insights on how the dual-modulated Z-converter can be decoupled, using non-linear feedback schemes, that would likely require sophisticated application of DSP methods. Given that the objectives of this thesis are mainly geared towards an appreciation of the power topologies rather than the control mechanisms, a more traditional strategy, involving a number of iterations, is adopted. The small-signal model is studied and the first control loop is compensated, assuming single modulation of D, with D_o kept constant. The second loop is then compensated, with the first closed loop in place, and so on. With all compensated loops in place, coupled transfer functions can be optimized by iteration. Thus, in order to obtain a working model for simulation, analysis, and comparison, SISO techniques can still be employed rather than more involved methods, such as LQR or non-linear feedback de-coupling.

As was mentioned in 5.3.1, the control scheme can be made to direct the ripple current into the EV battery (Scheme 1) or into the PV source (Scheme 2). The former is more complex, and hence, its derivation will be demonstrated in more detail below. However, the latter will also be designed and simulated for verification.

5.3.8.1 Inverting Operation with no Battery: Plant behavior

Fig. 5-10 shows the circuit to be averaged. Note that the ESRs of the power passive components are included.
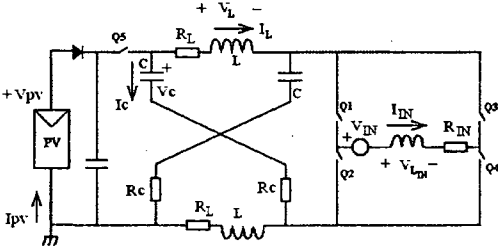
Fig. 5-10 Base circuit with no battery for average modeling

By assuming symmetric operation, with the Z-circuit capacitors and inductors pairs being identical, and also considering only the three normal switching states, the following average model can be derived.

$$\frac{d}{dt}\begin{bmatrix} I_L \\ V_C \\ I_{IN} \end{bmatrix} = \begin{bmatrix} \dfrac{-(Rc+R_L)}{L} & \dfrac{2Do-1}{L} & \dfrac{DRc}{L} \\ \dfrac{1-2Do}{C} & 0 & \dfrac{-D}{C} \\ \dfrac{2DRc}{L_{IN}} & \dfrac{2D}{L_{IN}} & \dfrac{-(2DRc+Rin)}{L_{IN}} \end{bmatrix}\begin{bmatrix} I_L \\ V_C \\ I_{IN} \end{bmatrix} + \begin{bmatrix} \dfrac{(1-Do)}{L} \\ 0 \\ \dfrac{-D}{L_{IN}} \end{bmatrix}V_{PV} + \begin{bmatrix} 0 \\ 0 \\ \dfrac{-1}{L_{IN}} \end{bmatrix}V_{IN} \quad (5\text{-}4)$$

By setting the differentiated state vector on the left side to zero, the DC relationships can be readily derived. However, the presence of parasitic resistance terms makes this solution lengthy. Instead, it is more practical to approximate the solution by setting these resistances to zero and solve the undamped system; this will yield a fairly good idea of the bias point operation and will aid with the design of the main circuit components. The three solutions for the undamped system were already expressed in Eq. 5-1, Eq. 5-2, and Eq. 5-3.

The small-signal model is derived from the average model, by perturbing all inputs (D, D$_o$, V$_{PV}$, and V$_{IN}$).

$$s\begin{bmatrix} i_L \\ v_C \\ i_{IN} \end{bmatrix} = \begin{bmatrix} \dfrac{-(Rc+R_L)}{L} & \dfrac{2Do-1}{L} & \dfrac{DRc}{L} \\ \dfrac{1-2Do}{C} & 0 & \dfrac{-D}{C} \\ \dfrac{2DRc}{L_{IN}} & \dfrac{2D}{L_{IN}} & \dfrac{-(2DRc+Rin)}{L_{IN}} \end{bmatrix}\begin{bmatrix} i_L \\ v_C \\ i_{IN} \end{bmatrix} + \begin{bmatrix} \dfrac{(1-Do)}{L} \\ 0 \\ \dfrac{-D}{L_{IN}} \end{bmatrix}v_{PV} + \begin{bmatrix} \dfrac{RcI_{IN}}{L} \\ \dfrac{-I_{IN}}{C} \\ \dfrac{2Vc-V_{PV}-2RcI_L}{L_{IN}} \end{bmatrix}\delta + \begin{bmatrix} \dfrac{2Vc-V_{PV}}{L} \\ \dfrac{-2I_L}{C} \\ 0 \end{bmatrix}\delta_0 + \begin{bmatrix} 0 \\ 0 \\ \dfrac{-1}{L} \end{bmatrix}v_{IN}$$

$$(5\text{-}5)$$

Solving the above system yields the transfer functions, from any of the four inputs to any of the three state variables. Again, the explicit representation of this solution is not desirable and should be left to numeric analysis if desired and, once more, the simpler

undamped model is considered as a starting point. The characteristic equation of the undamped system is given by:

$$\det[sI - A] = s\left[s^2 + \frac{2D^2}{CL_{IN}} + \frac{(1-2Do)^2}{LC}\right] \quad (5\text{-}6)$$

Here, A represents the state matrix. There exist 12 transfer functions, in total, that can be derived from the small signal model. The most important ones, for inverting operation, relate the grid current (I_{IN}) to the control signal δ (small signal of D). This is shown in Eq. 5-7.

$$\frac{i_{IN}}{\delta} = \frac{(2Vc - V_{PV})\left[s^2 - \frac{2D \cdot I_{IN}}{(2Vc - V_{PV})C}s + \frac{(1-2Do)^2}{LC}\right]}{sL_{IN}\left[s^2 + \frac{2D^2}{CL_{IN}} + \frac{(1-2Do)^2}{LC}\right]} \quad (5\text{-}7)$$

As can be seen, Eq. 5-7 is characterized by two zeros and two poles, in addition to a pole at the origin, that are determined by the power components, defined in 5.3.6 and 5.3.7. The form of Eq. 5-7 suggests that another criterion exists for choosing the values for the Z-circuit components that was not envisaged in 5.3.6 and 5.3.7. It relates to the fact that the Z-circuit has a relatively high Q and has natural resonance that cannot be eliminated by control. It is thus important not to excite the system at this resonance point, which must therefore be separated from the 120 Hz driving function. It is desirable to choose the Z-resonance at a higher frequency, in order to keep component size small. However, achieving this goal can be difficult. In fact, as clearly shown in [12], and hinted by the denominator in (5-7), the resonant frequency changes with operating point of D and D_o. Hence, a much higher frequency than 120 Hz must be chosen for nominal resonance. Of course, this implies small values for L and C, in direct contrast to the requirements for effective energy storage. These contrasting requirements are difficult to resolve, and

represent the biggest challenge for stable operation. In the present case, the values, as

derived in 5.3.6 and 5.3.7, produce a nominal resonance that is comfortably higher than

400 Hz. However, in the worst case, this frequency can be below 200 Hz, requiring

careful compensation.

A precise analysis of the transfer function of the Z-converter is outside the scope

of this thesis; rather, the main results from [12] and [13] will be used. In those references,

the authors point out the existence of a RHP zero in the transfer function (also visible in

Eq. 5-7), and determine the root loci of the Z-network for varying parameters. References

[12] and [13] also state that better dynamic behavior (due to increased damping) can be

achieved with higher values of D_o and C, and lower values of L. While the higher limit of

C and lower limit of L are determined by cost and ripple current at 25 kHz, D_o is set by

requiring V_C to be at 550V (see Eq. 5-2). Furthermore, the ESRs for the Z-network

components also increase damping, and should therefore be maximized, as far as

efficiency considerations permit. Here, $30m\Omega$ is used for R_{IN} and R_L, and $120m\Omega$ for R_C.
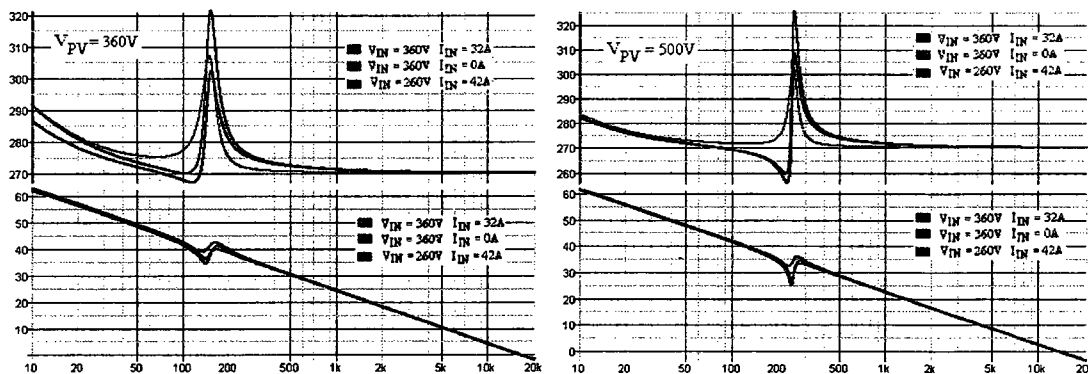
Fig. 5-11 Plant frequency response (i_{IN}/δ) for extreme values of V_{IN}, I_{IN}, V_{PV}.

Fig. 5-11 shows the i_{IN}/δ transfer function, including damping, obtained numerically

using the *SiMetrix* software and (5-5). It is possible to see that there is no phase reversal

42

within the full range of operating conditions. As such, the plant can be compensated to obtain stable operation. Also, the resonance is closest to 120 Hz, when V_{PV} is lowest; however, there is no overlap.

5.3.8.2 Inverting Operation: No Battery compensation for the input current loop

The first loop to be compensated is the input current loop. This choice is not arbitrary; in fact, it is based on the fact that the input current loop is inherently weakly coupled to D_o, thus providing an adequate starting point. The main requirement for controlling the input current is that it can produce an undistorted waveform. As a consequence, the gain of the compensator at 120 Hz must be of the order of 20dBs or higher, for an error of less than 5%. Crossover will be designed at approximately 10 kHz, below the *Nyquist* limit of 12.5 kHz, for a switching frequency of 25 kHz.
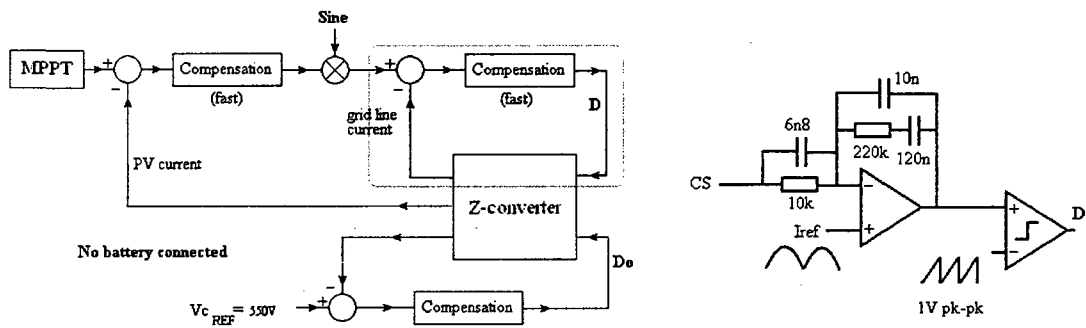
Fig. 5-12 Input current loop (left); Error amplifier design (gain: 21db at 120Hz) (right)

Fig. 5-12 shows the compensation for the loop controlled by duty cycle D (while D_o is kept fixed, for inverting operation without the battery). It must be noted here that, throughout this thesis, no formal derivations of the compensators are performed. Rather, the specific implementations that are used in the simulations (Ch. 6) are shown for reference. The signal I_{ref} is a sinusoidal waveform, in phase with the input voltage; its

amplitude is controlled by the MPPT section. The signal CS is the feedback signal from the line current sensor (refer to Fig. 5-5). With this compensation, consisting of two poles and two zeros, the open-loop response is shown in Fig. 5-13, for key operating conditions.
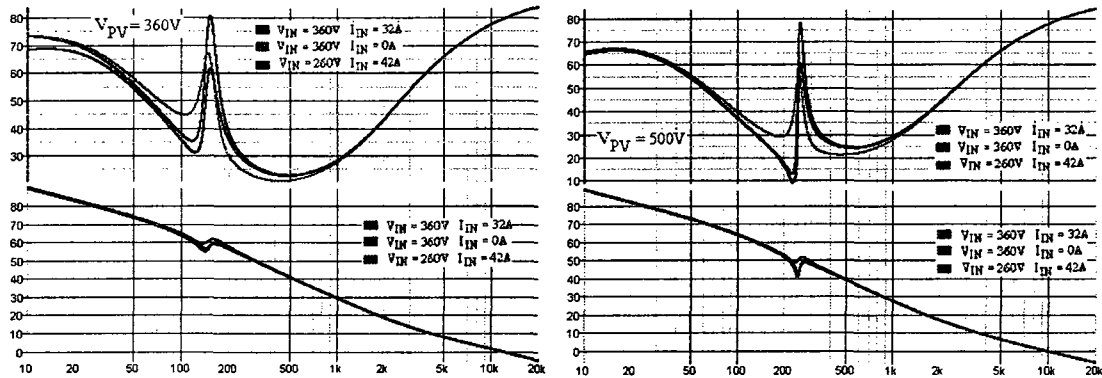
Fig. 5-13 Input current open loop response with Do constant (extreme conditions)

Note that the phase margin is greater than 70°, crossover at 10 kHz, as targeted in both extreme cases. It must be noted here that throughout this thesis, stability is analyzed using Bode plot techniques, despite the presence of an RHP zero in the undamped system. Stability evaluation then follows the guidelines presented in [14].

5.3.8.3 Inverting Operation: No Battery MPPT PV Current Loop (Scheme 1)

The input current loop (discussed in 5.3.8.2) is an inner loop to the MPPT commanded loop, as shown in Fig. 5-14. In other words, the MPPT device programs the desired PV panel output current by commanding the appropriate current at the grid. In order to design the compensator, the closed loop transfer function of the input current loop (with D_o kept constant) is obtained from the model, and a provisional compensation is also obtained.
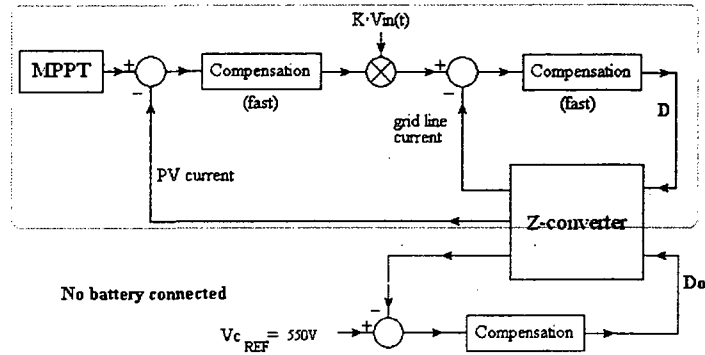
Fig. 5-14 MPPT Panel Current Loop

Note that the overall response for this loop must be set much slower than line frequency, otherwise the commanded line current will be distorted by the error voltage. This can cause long time lags to steady-state upon an MPPT command or line voltage change. Such a scenario may or may not be acceptable, especially in the presence of an MPPT device with its own dynamic properties. Moreover, the ubiquitous Z-circuit resonance tends to push this loop to instability, if a larger bandwidth is targeted. To address this issue, a slightly quicker response can be designed, at the cost of adding a ripple elimination circuit, as part of the capacitor voltage regulation control. This increases the coupling between D and D_o. This latter solution can be deemed the least of two problems, and is adopted, as will be discussed in 5.3.8.5.
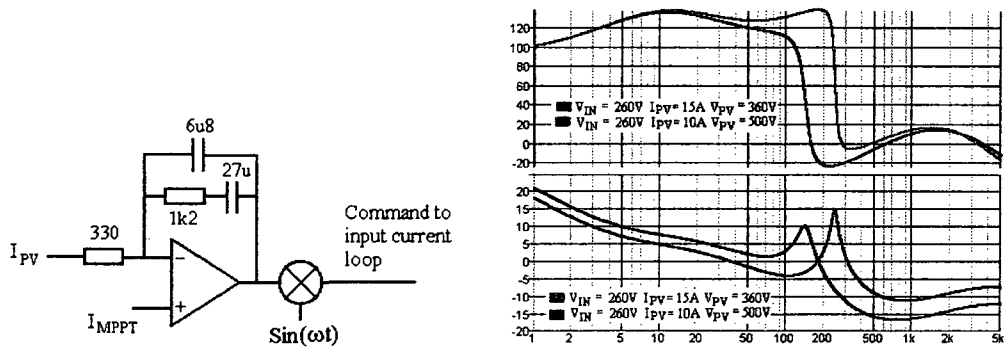
Fig. 5-15 Compensator for MPPT Panel Current Loop (left); Loop response (right)

45

Fig. 5-15 shows the compensation used and the frequency response of loop, without the added ripple elimination scheme, mentioned above. Note that the loop by itself, as aforementioned, is indeed unstable.

5.3.8.4 Inverting Operation: No Battery Capacitor Voltage Control (Scheme 1)

The voltage on the capacitors will be regulated at 550V, when the EV battery is not present. No attempt should be made to regulate the 120 Hz ripple out, because this would force the pulsating current into the PV source, which runs against the objectives of Scheme 1. Therefore the designed loop bandwidth should be small.
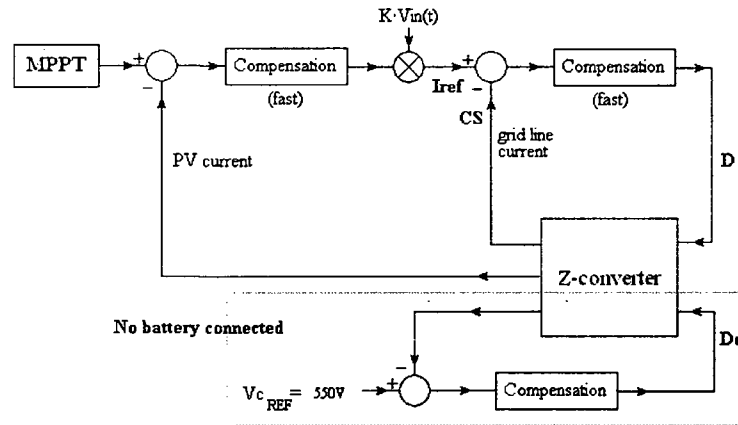
Fig. 5-16 Basic loop for Z-capacitor voltage compensation

Although its purpose is clear, this loop may or may not fully set D_o. In fact, an additional optional control of D_o can be added, to force most of the 120 Hz current ripple away from the PV source, and into the Z-capacitors (see 5.3.1). Without this addition, heavy filtering at the PV output becomes unavoidable, and Scheme 2 must be adopted. The full capacitor voltage regulation scheme is, therefore, dealt with in the following sub-section.

5.3.8.5 Inverting Operation: No Battery Reduction of PV Ripple (Scheme 1)

The optional additional control is shown in Fig. 5-17. This idea is related to that used in [9], where output ripple was successfully eliminated in a Z-loaded rectifier application. In [15], a similar concept using feed-forward was employed in a bi-directional ASD system, to achieve the same purpose.
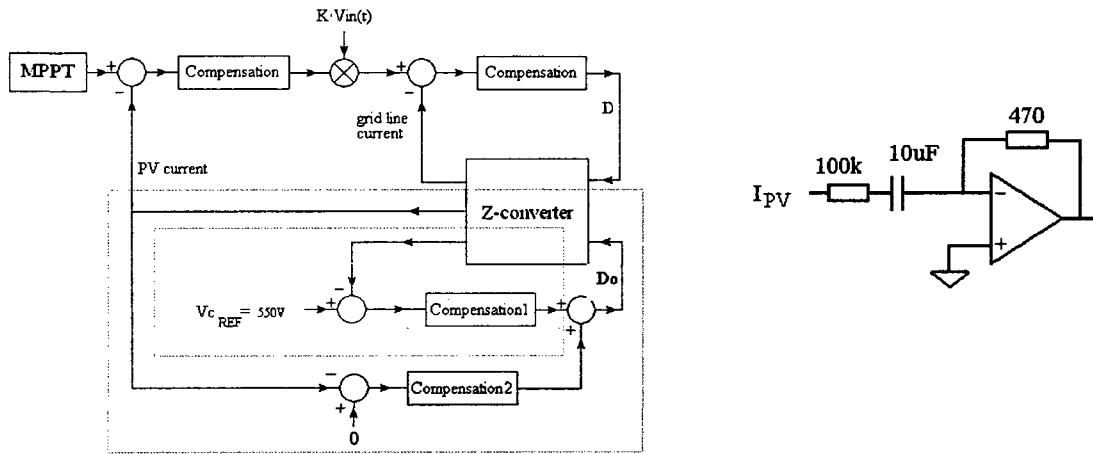
Fig. 5-17 Modified loop for capacitor voltage regulation (left); Compensation2 (right)

Unfortunately, in this case, simulation studies show that the ripple cannot be eliminated completely, due to issues related to stability and dynamic range of control variable D_o. However, these issues can be minimized to an acceptable level with or without further addition of a modest decoupling capacitor (see 6.1.4, for more in-depth discussion). The proposed action compares panel current, I_{PV}, to a DC reference (such as 0V). The compensation that follows will ignore the DC component of the error, suggesting a derivative controller, with a zero at the origin. It will also deliver substantial operating gain at 120 Hz, thus reducing the ripple component on the sensed variable, the PV current. These characteristics are supplied by the compensation shown in Fig. 5-17. With this added feedback and the input as well as PV current control loops in place, the

open-loop transfer function from V_C to D_o can be modeled and compensated through the block labeled "Compensation1" in the Fig. 5-17. The compensator and the overall loop, including Compensation 1 and Compensation 2, are shown in Fig. 5-18.
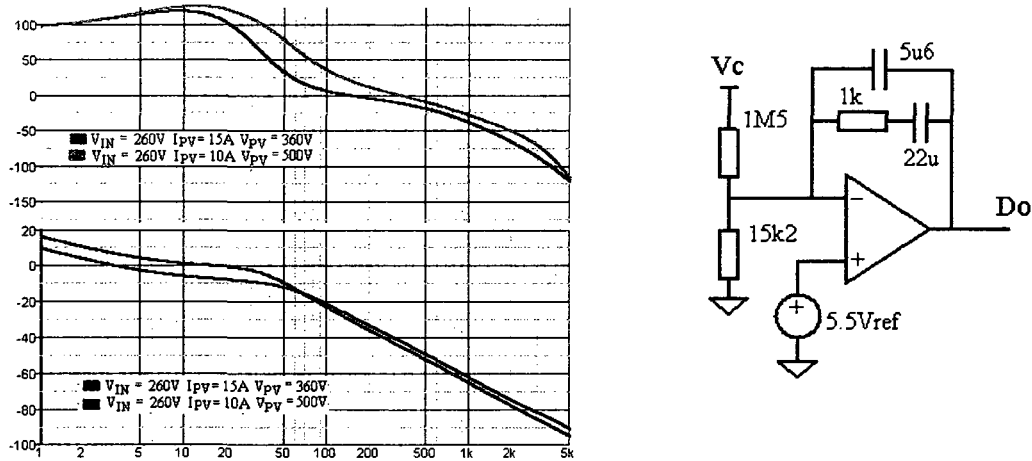
Fig. 5-18 Overall V_C control loop response and compensator (Compensation1)
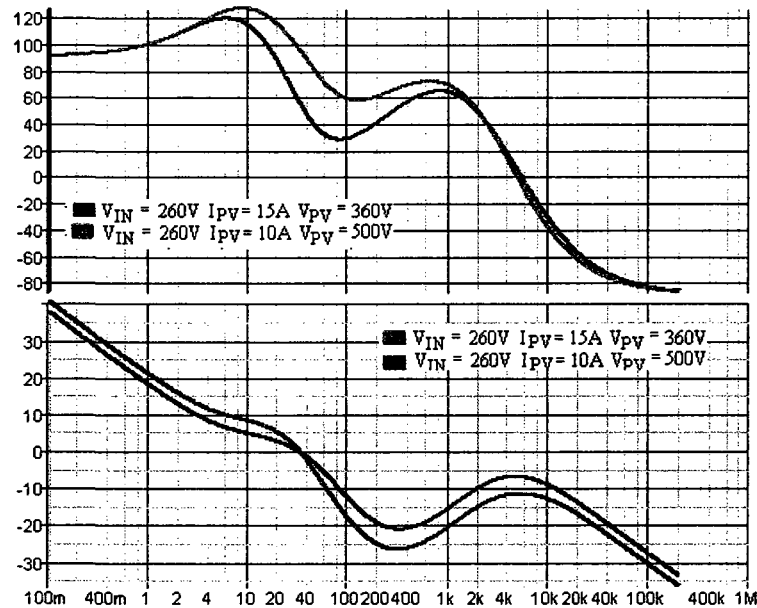
Fig. 5-19 Revised loop response for the PV panel current control loop

Fig. 5-19 shows the revised Bode plot for the PV panel current control loop. Comparing this to Fig. 5-15, it is notable that the instability is successfully eliminated.

5.3.8.6 Operation with Battery: Plant Behavior

The steps followed in sections 5.3.8.1 to 5.3.8.5 are repeated for a system with a connected battery. From the steps performed in 5.3.5 and APPENDIX A, the topology with battery and the DC/DC isolating converter in place can be redrawn in Fig. 5-20. The averaging method is used again, including the additional state space variable, i_B.
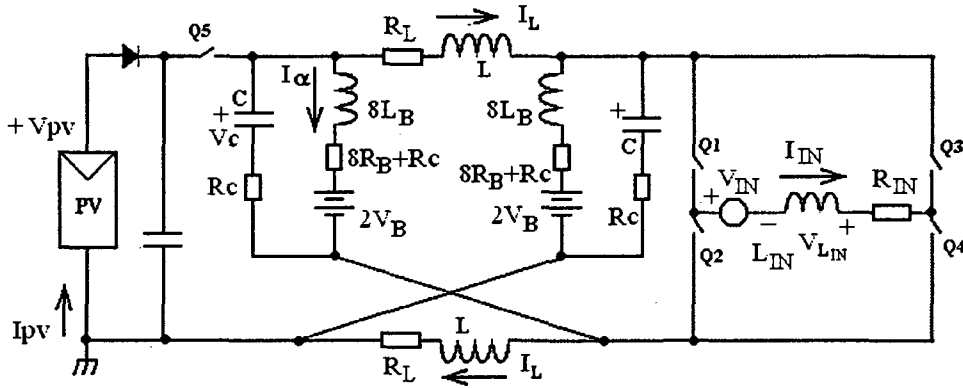
Fig. 5-20 Equivalent model of Z-converter with battery.

$$I\alpha = \tfrac{1}{4}\,I_B \qquad C = \tfrac{1}{2}\,C_{HB} \qquad R_C = 2R_{HB}$$

$$\frac{d}{dt}\begin{bmatrix} i_L \\ v_C \\ i_{IN} \\ i_B \end{bmatrix} = \begin{bmatrix} \dfrac{-[R_C+R_L]}{L} & \dfrac{2Do-1}{L} & \dfrac{DR_C}{L} & \dfrac{R_C(1-2Do)}{4L} \\[2mm] \dfrac{(1-2Do)}{C} & 0 & \dfrac{-D}{C} & \dfrac{-1}{4C} \\[2mm] \dfrac{2DR_C}{L_{IN}} & \dfrac{2D}{L_{IN}} & -(2DR_C+Rin) & \dfrac{-DR_C}{2L_{IN}} \\[2mm] \dfrac{(1-2Do)R_C}{2L_B} & \dfrac{1}{2L_B} & \dfrac{-DR_C}{2L_B} & \dfrac{-(2R_B+1/2R_C)}{2L_B} \end{bmatrix}\begin{bmatrix} i_L \\ v_C \\ i_{IN} \\ i_B \end{bmatrix} + \begin{bmatrix} \dfrac{1-Do}{L} \\[2mm] 0 \\[2mm] \dfrac{-D}{L_{IN}} \\[2mm] 0 \end{bmatrix}V_{PV} + \begin{bmatrix} 0 \\[2mm] 0 \\[2mm] \dfrac{-1}{L_{IN}} \\[2mm] 0 \end{bmatrix}V_{IN} + \begin{bmatrix} 0 \\[2mm] 0 \\[2mm] 0 \\[2mm] \dfrac{-2}{2L_B} \end{bmatrix}V_B$$

$$(5\text{-}8)$$

The frequency response for the input current loop is obviously modified by the presence of the battery, and needs to be checked again for stability. Furthermore, a different loop, one that controls battery current instead of capacitor voltage, is now present, that needs to be characterized and compensated. Since the compensation for the other loops will tentatively be the same, whether or not batteries are connected, there will be no need to

evaluate the plant open-loop response, but each control loop will be assessed individually.

5.3.8.7 Operation with Battery: Compensation for the Input Current Loop

The response of the input current loop with the battery connection is shown in Fig. 5-21. It is evaluated by inserting an AC stimulus upon signal D, with the output of the MPPT compensation kept constant. Note that in this case, D_o is not kept constant as was followed previously; in fact, D_o is allowed to change, given that it is coupled to D. In keeping with the iterative design approach discussed in 5.3.8, this results in a more realistic description of the true open-loop response.
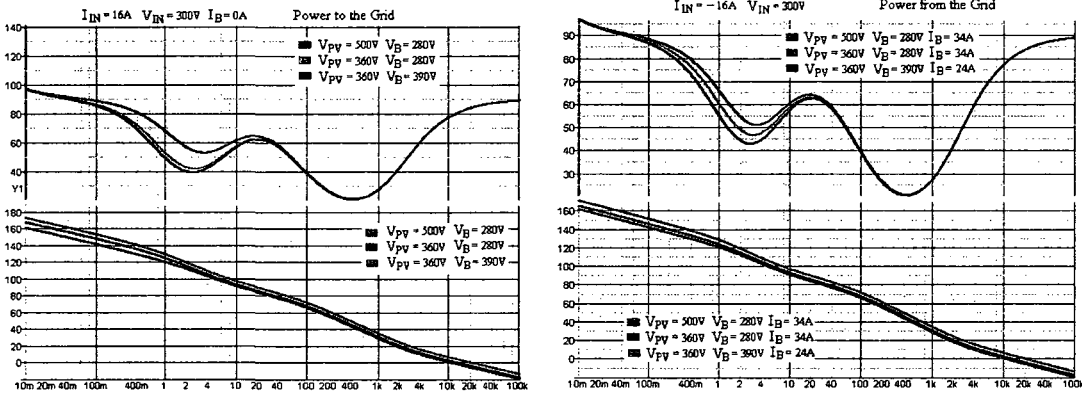
Fig. 5-21 Input current loop response (with compensation) for system with battery

From Fig. 5-21, it is clear that the response is similar to that obtained without the battery connection and with D_o kept constant, with the obvious difference that the Z-circuit resonance is removed. Note that Fig. 5-21 only depicts a small number of operating conditions for PV, input, and battery voltages and currents. All other relevant conditions were analyzed (not shown here); the compensation obtained in 5.3.8.2 is retained.

5.3.8.8 Operation with Battery: MPPT Panel Current Loop (Scheme 1)

Fig. 5-22 shows the panel current control open-loop response. As can be noticed, the response is similar to that of Fig. 5-15, without the resonance, due to the presence of the battery.
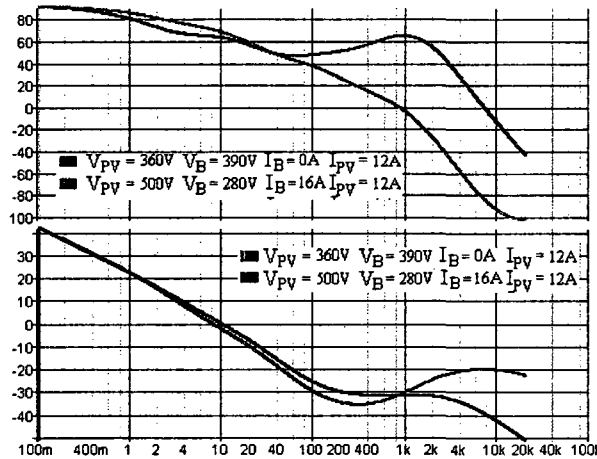
Fig. 5-22 MPPT I_{PV} loop response (with compensation) for system with battery

It is worthwhile mentioning here that the tentative compensation used in 5.3.8.3 is retained.

5.3.8.9 Operation with Battery: Battery Current Regulation (Scheme 1)

The connected battery will be charged by the amount of current requested by the vehicle's on-board controller. This control loop replaces that used to regulate the capacitor voltage, when the battery is not present. Because its function is fundamentally different when a battery is connected, it is unlikely the same compensation used in 5.3.8.4 can be retained. Rather, different control circuits must be selected depending on whether the battery is present or not. The plant open loop response is obtained by adding a stimulus upon D_o, and is shown in Fig. 5-23.
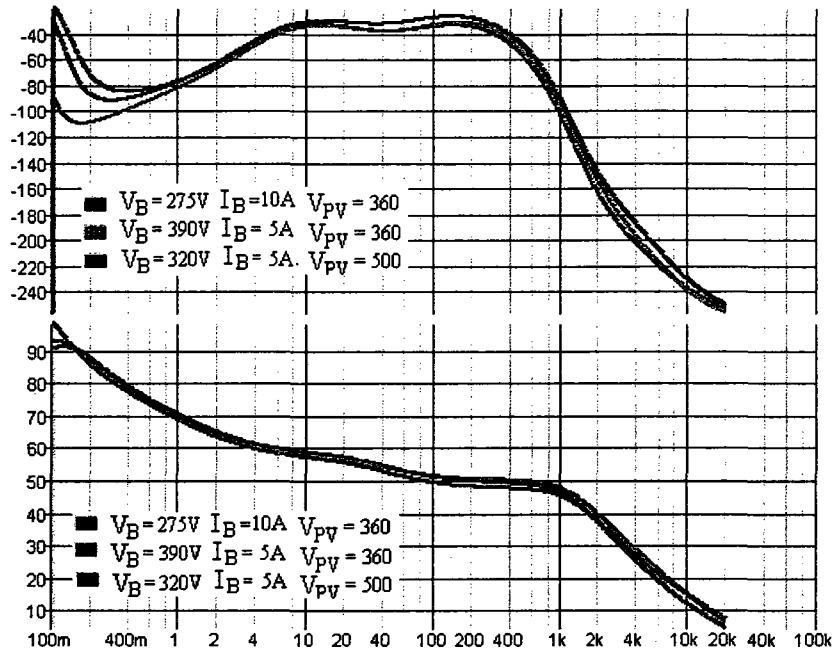
Fig. 5-23 Plant frequency response for charge current loop

This response shows a high gain, notably at 120 Hz. The required compensator will, therefore, attenuate markedly at this frequency; so that the 120 Hz will (suitably) not be transmitted to the error (this suppression at 120Hz is required; see 5.3.8.3). Compensation 1 and Compensation 2, as well as the overall charge current loop response, are shown in Fig. 5-24. Note that Compensation 2 is unchanged.

From the discussion above, Compensation 1 will essentially offer a high gain only at DC or very low frequencies, exposing another major limitation of the proposed system. Naturally, if the rate of change of the I_B request signal from the on-board vehicle controller exceeds approximately 1 Amp/sec, the loop can only retain control in the presence of unacceptably large real battery current, I_B.
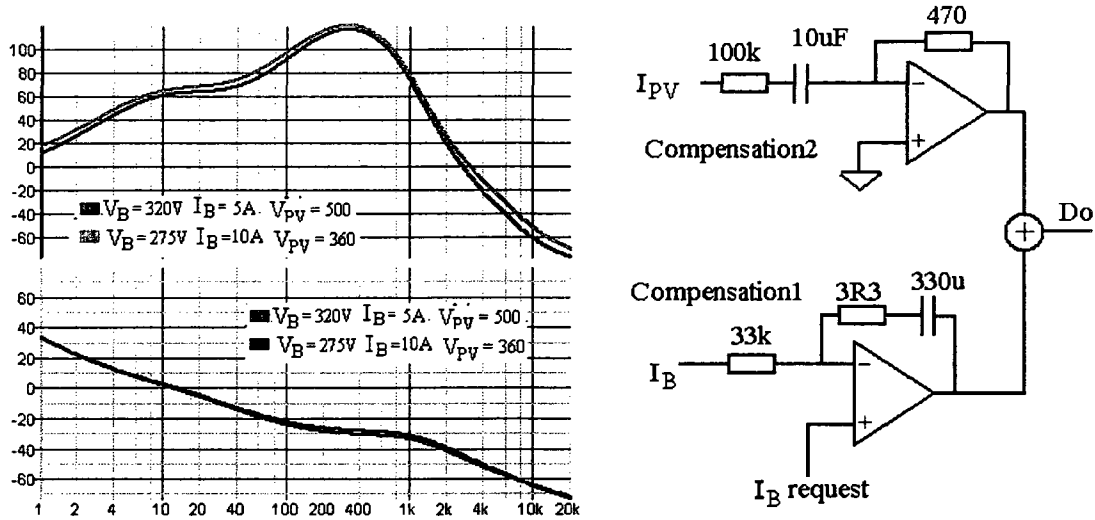
Fig. 5-24 Overall response for charge current loop (left); Compensators used (right)

In actual circuits, the most likely scenario would include a particular control op-amp in one of the loops saturating, so that the charge control loop opens, and the system runs uncontrolled. To avoid this occurrence, a restriction must be imposed on the I_B request signal rate of change and additional protection circuits must be considered. This limitation, however, is only very significant in Scheme 1.

5.3.8.10 Discussion on Compensation for Scheme 2

When it is desired to alleviate the battery current ripple problem and instead opt for adding more decoupling at the PV terminals, Scheme 2 can be targeted. Obtaining Scheme 2 is a simple problem of eliminating the ripple elimination loop (Compensation 2). The remaining Compensation 1 is then modified to have much higher gain at 120 Hz, in order to regulate out the ripple.
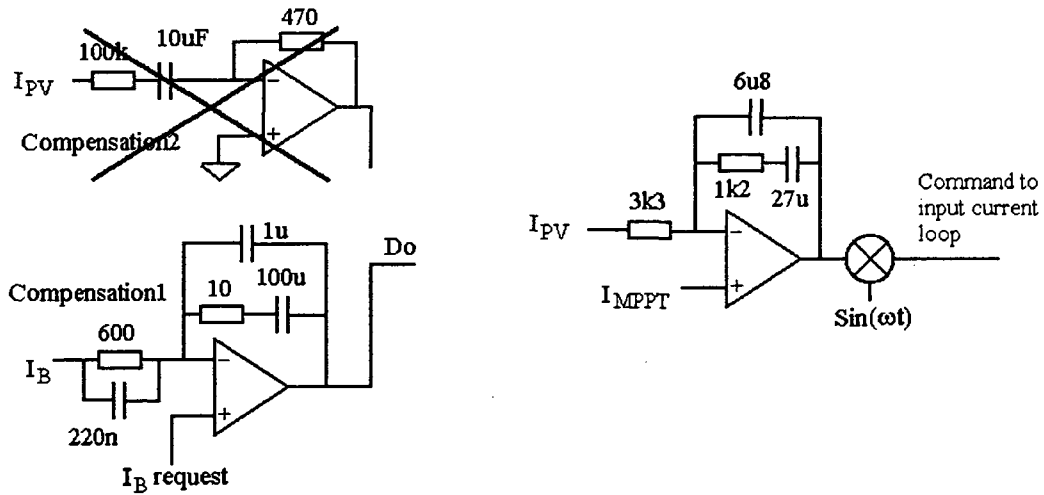
Fig. 5-25 Compensation changes for Scheme 2. Battery charge current and MPPT I_{PV}

The MPPT Panel Current Loop compensation must also change, to eliminate the instability shown in Fig 5-15. In addition, its gain must be suppressed, in order to make the error irresponsive to the newly acquired 120 Hz ripple. The compensation modifications are shown in Fig. 5-25.

5.3.9 Comments

Having fully modeled the Z-converter for this application, its performance will be evaluated in the next chapter. Some comments of a more qualitative nature can be introduced here.

5.3.9.1 Cost

The Z-topology allows distributing PV power to the grid as well as to the EV battery with a single stage of conversion. One of the hopeful consequences of this premise is a reduction in cost. Table 5-1 is a list of cost factors that are relevant for the Z-converter.

Table 5-1 Cost factors for Z-converter

COST REDUCTION	COST ADDITION
Light cabling from PV (due to high PV voltage supported)	5kVA 60Hz isolation transformer
Relatively low power component count	High voltage power capacitors
Simple drive method for DC/DC converter	High voltage power semiconductors
Simple 1:1 isolation transformer for DC/DC converter	Large enclosure/sheet metal
Open loop operation of DC/DC converter (no isolated sensors)	Added protection circuits (see 5.3.8.9)

It appears that the cost balance may or may not be a positive one. The presence of the line-frequency transformer and larger enclosure weighs heavily on the negative side. However, this transformer may be required because of other criteria. For instance, the transformer-less topology is far from being universally accepted by safety agencies around the world. Utility companies may also rather see a galvanic barrier, prior to the interface point, in order to ensure both isolation and guaranteed elimination of DC current injection into the grid. In these cases, the Z-converter is certainly cost competitive.

5.3.9.2 Reliability

Voltage levels on the IGBTs and Z-circuit capacitors are relatively high. However, when appropriate ratings are used, the reliability of this topology is intrinsically very good, due to low component count. The presence of the 60 Hz transformer does not affect it in an appreciable manner, and there exist only four 450V (standard availability) small value electrolytic capacitors, that are commercially available in various reliability and life ratings. This fact is possible due to the introduction of the added ripple attenuating control described above, for allowing a design with very little capacitance across the PV source (Scheme 1) - large capacitors being otherwise necessary

(Scheme 2) [16]. Worst-case voltage on the capacitors is 400 V (for maximum battery voltage of 400V), while that on the IGBT, is 1240 V, excluding any parasitic transients (with maximum V_B at 400V and min V_{PV} at 360V). Higher voltage devices are both more expensive as well as less performing than lower voltage ones; however, they do allow more design trade-offs.

Note that Fig. 5-7 shows the presence of 13 switches. Although this number is high, it can be reduced down to 9 by employing alternate common topologies for the DC/DC converter. On the other hand, the chosen topology for the DC/DC converter portion can be realized using high reliability, low voltage/low current devices. Because the converter runs in open loop, the driver is simple, and the control is devoid of isolation/sensing devices.

5.3.9.3 Dynamic Behavior, Interaction with PV Source, Interaction with Grid

It is evident that the control of the Z-converter is extremely complicated, due to the unavoidable relationship between the two control variables, D and D_o, and the fact that the energy storage components are present within the control equations. Also, the impossibility of effectively decoupling the power flow into the battery and the PV source from that of the Z-capacitor implies that the 120 Hz power ripple must be absorbed by either the battery or the PV source. For Scheme 1, this is achieved by decreasing the bandwidth of the charge current control system, with consequent slow response to external stimuli from the PV source and input line voltage. The PV source voltage itself changes rather slowly in response to irradiation level shifts and speed of the MPPT algorithm [17], thus causing only minor problems. A sudden change in the I_B request signal, however, is problematic for Scheme 1, and must be avoided externally, as

mentioned in 5.3.8.9. As such, changes cannot be easily handled using linear control. Should this become a critical issue, Scheme 2 can always be implemented, as it supports much quicker dynamics.

5.3.9.4 Design Flexibility

Another obvious shortcoming, originating from the close coupling of the battery to Z-circuit, and the use of linear control (compared to robust techniques, such as Sliding Mode Control), is the fact that the charge limiting resistance, R_B, becomes a non-negotiable part of the control loop. It becomes impossible to optimize the loop response prior to knowing this resistance value. Unfortunately, different battery technologies and even different states of charge have different characteristic resistances that would require different optimal compensations. In addition, the nominal battery voltage is also limited by the absence of a fully regulated DC/DC converter. Therefore, connection to a severely discharged battery, for instance, is not supported by this topology.

5.4 HIGH-FREQUENCY TRANSFORMER-ISOLATED TOPOLOGY

5.4.1 Background

In specific cases, where a large 5kVA, 60 Hz transformer is unacceptable, various topologies that retain galvanic isolation from grid to panels can be used. These are described in references [4] and [18]. A fair assessment, based on these references, is that there is no clear option among the competing topologies; rather, different approaches satisfy different design priorities. On the other hand, because the PV-powered charge infrastructure is not a straightforward grid-tied system, like those described in [4] and [18], which include an added DC/DC charger, many of the proposed circuits are not

easily exploitable. The otherwise attractive *pseudo-DC-link* topologies are an example, as

are topologies using output current-fed inverters. Among those approaches that use a HF

transformer for isolation, the benchmark is provided by the classic two-stage topology

with DC-link, shown in Fig. 5-26.
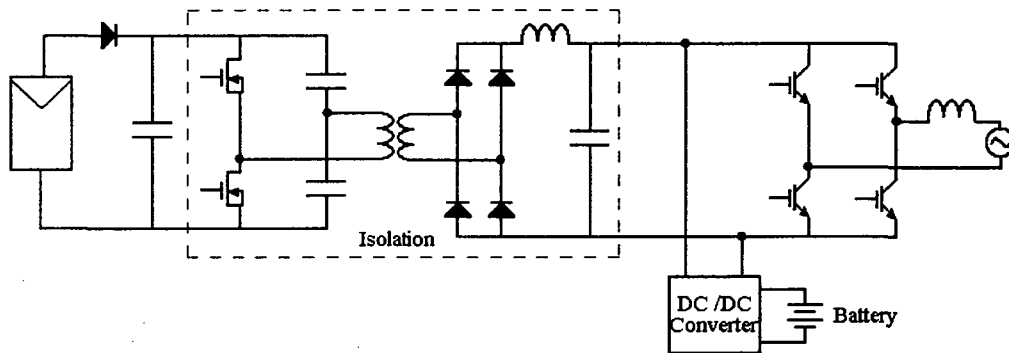
Fig. 5-26 HF Transformer Isolated Topology

For comparison purposes, this topology will be studied in the following chapters.

The lengthy AC and dynamic response analysis for the inverter and DC/DC converter

will not be included here, given that these are common topologies that have been treated

at length in related literature.

5.4.2 Isolation and DC-Link

The main purpose of the isolation section shown in Fig. 5-26 is, of course, to offer

isolation from the grid to the PV. Such an arrangement can also provide supplementary

functions. For instance the half-bridge could be replaced by a regulated buck-boost

converter stage. In this case, the DC-link voltage could be made to track the EV battery

voltage and minimize switching losses in the DC/DC converter, while the buck-boost

stage provides added flexibility, to deal with wider voltage ranges out of the PV panel.

This can be implemented with few minor added costs, in terms of component stress and

overall efficiency, which might be offset by the need to satisfy design requirements. In the case of this thesis, the requirements have been set, and can be satisfied by the isolated buck topology of Fig. 5-26, running in open loop at full duty cycle for zero-voltage switching (ZVS) and maximum efficiency. Due to ZVS, a very high frequency can be selected when MOSFETs are used, so that the filter components in the DC link can be minimized in size and cost.

5.4.3 Component Design

5.4.3.1 Isolation Transformer Turns Ratio Calculation

The steady state voltage gain from the output of the PV source to the input of the inverter bridge is simply ½ N, where N is the turns ratio of the transformer. Because the voltage-source inverter (VSI) bridge can only buck, the defining condition is with minimum V_{PV} = 360V and maximum V_{IN} = 370Vpk. A turns ratio of 3/7 will provide a minimum DC link voltage of 420V, corresponding to an overhead of 14%, for dynamic control. The maximum DC link voltage will be 580V, allowing the use of efficient IGBT devices.

5.4.3.2 DC-Link Filter

The DC-link filter inductor can be considered a simple smoothing choke of very small value. This is due to the full duty cycle on the half-bridge. The capacitor, on the other hand, will be sized to handle the pulsating power from the grid, and will therefore be as large as the combined size of the Z-circuit capacitors discussed earlier.

5.4.3.3 Inverter Bridge and DC/DC Converter Power Devices

As the DC bus voltage is limited to less than 600V, very fast and efficient IGBTs as well as diodes can be used for the inverter bridge and the DC/DC converter. The architecture of the DC/DC converter is shown in Fig. 5-27. The arrangement is similar to that of the Z-converter, with the DC-link capacitor split, in order to accommodate a half-bridge converter. The main difference is that this converter has a full loop controlling duty cycle. Therefore, the smoothing choke will be relatively large and can be expected to detract from the efficiency number. A turns ratio for T2 of 1:2 will guarantee that a 400V battery can be charged, when V_{PV} is minimum, at 360V. The inductance L_B is calculated so as to provide $\pm10\%$ ripple under worst-case; that is, when V_{PV} is maximum, at 500V, and battery voltage is minimum, at 275V. Calculation of the required inductance value is straightforward and yields 800μH, at 50 kHz switching frequency.
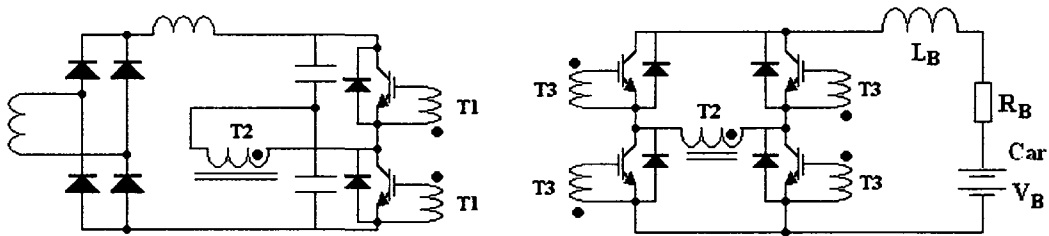
Fig. 5-27 DC/DC converter

This inductance can be less lossy than that of the Z-circuit, because it need not supply damping. An ESR of 0.03Ω is chosen (or 50% that of the Z-circuit combination).

5.4.4 Comments

5.4.4.1 Cost

Compared with the Z-converter, this topology replaces an expensive 60 Hz transformer with a small HF transformer. Considering that the primary winding is driven

in ZVS, the frequency in question could be extremely high, thus virtually eliminating the cost due to the isolating function. Additionally, the ensuing reduction in size should result in savings related to sheet metal.

Although this topology only has one large choke, L_B, in Fig. 5-27, it carries more current and has higher value than each of the Z-circuit inductors. Overall, the I^2L value is similar (compared to two 15A, in 650μH, to a single 18.5A in 800μH). A similar conclusion can be made for the Z-circuit capacitors, when compared to the DC-link capacitors for this topology. In both cases, they must be sized to deal with the same pulsed power from the grid.

Because of the double conversion stage and the AC/DC/AC/DC structure, this topology has high semiconductor content. Compared to the Z-converter, it includes an additional fast-diode full-bridge rectifier, and 5 IGBTs, accompanied by fast freewheeling diodes (note: all MOSFETs operating in ZVS are not considered here). Moreover, an extra control and drive circuit is needed for the additional conversion stage (see the comparison matrix below).

Table 5-2 Cost comparison HT transformer vs. Z-converter topologies

Component	Z-converter (LF transformer isolated)	HF transformer isolated
PV cabling	GOOD	GOOD
Transformers	GOOD	BETTER
Chokes	GOOD	GOOD
Capacitors	GOOD	GOOD
IGBTs	GOOD	POOR
Diodes	GOOD	POOR
Drivers	GOOD	POOR
Sheet metal	GOOD	BETTER
OVERALL	GOOD	BETTER

Considering the absence of the power transformer and, to a lesser extent the lighter sheet metal, cost should be much reduced compared to the Z-converter topology.

5.4.4.2 Reliability

Although the semiconductor component count is problematic, their electrical stress can be managed well, as all currents and voltages are precisely defined. This is not the case for the Z-converter, where the voltage stress on the bridge components, for instance, is strongly dependent on the operating point. A simple way of describing this is that this topology is inherently less reliable than the Z-converter. However, it can be easily upgraded by choosing better performing components. Considering that the cost is expected to be relatively lower, this may be quite acceptable in most cases.

5.4.4.3 Dynamic Behavior, Interaction with PV Source, Interaction with Grid

Because the battery charge current is controlled independently from the line current, dynamic behavior for this topology can be expected to be better than that of the Z-converter. Specifically, the EV battery current command can change rapidly and be followed by a fast control. It is not clear how important this feature might be in practical terms, although it definitely provides an added degree of flexibility, when interfacing to the vehicle on-board controller. Moreover, the added conversion stage completely removes the AC component from the battery charge current.

As is the case for the Z-converter, interaction with the line presents no major problems. However, since the isolation transformer is placed prior to the inverting bridge, this topology is capable of injecting a DC current component into the line. Given the strict IEC and IEEE requirements for DC-current injection, resolving this problem will

necessitate a more sophisticated current sensor and very high-accuracy and low-drift components and circuits [19], [20]. Periodic calibration may also be required, challenging one of the design goals established in 5.1.

5.4.4.4 Design Flexibility

This design comprises of two independently controlled power stages, including two isolation transformers that can be utilized to step-up or step-down critical voltages. As such, this configuration is extremely flexible, and can adapt itself to wide-range input/output requirements.

5.5 TRANSFORMER-LESS TOPOLOGY

5.5.1 Background

The topologies described in the previous two sections use a power transformer to achieve two critical operational goals. The first is isolation and the second is to provide voltage amplification, in order to optimize power transfer and electrical stress levels; the former is a safety requirement, while the latter is a design requirement. However, it is practical to assume that the PV source, the grid, and the battery may all be available in voltage ranges that are already close-to-optimal, without the need for intervening amplification. Furthermore, if safety agencies allow the use of non-isolated inverters from PV source to grid, then the transformer-less topology becomes extremely attractive. The DC/AC/DC/AC configuration, described in section 5.4, can then be reduced to a mere DC/AC.

Safety regulations in Europe have historically been lenient compared to North American standards, whereby PV panels may not be grounded as long as the switching topology guarantees small common-mode voltages, thus reducing dangerous leakage currents. The additional problem of a safety hazard, following an insulation breakdown, is dealt with by using Ground Fault Interrupter devices. Many of the known transformer-less topologies, however, also allow direct grounding of the panels. This is the case for the topology selected in this study. Consider the simple buck topology shown in Fig. 5-28 (left).
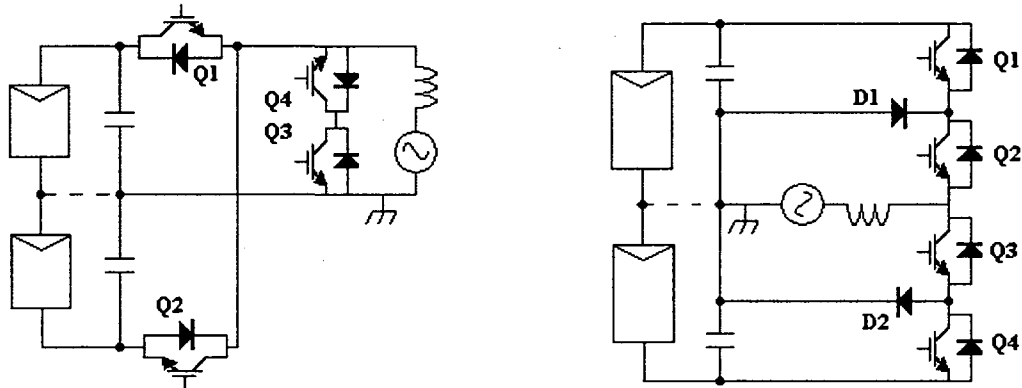
Fig. 5-28 Transformer-less topology (left); Neutral Point Clamped topology (right)

During the positive half of the cycle, Q2 is off and Q4 on at all times. Then Q1 and Q3 switch complementarily, in a classic buck configuration. This topology has only 4 devices and drives the grid current in a unipolar fashion, for low harmonic content and high efficiency. The only major drawback is that Q1 and Q2 must be rated at twice the maximum PV voltage. Thus, while Q3 and Q4 can be high-efficiency, 600V IGBTs, Q1, Q2 must be 1200V devices.

The Neutral Point Clamped (NPC) topology, shown in Fig. 5-28 (right), has increased conduction loss, because grid current is always driven through two series-

connected semiconductor switches. In fact, during the positive half-cycle, Q2 is on and Q4 off at all times, while control is exercised by Q1 and freewheeling diode, D1. On the other hand, with the NPC, all devices can be rated at 600V. Thus, the choice between the topologies shown in Fig-5-28 is strongly affected by whether conduction or switching loss is dominant. Moreover, it is important to consider that both topologies may have to be modified, in order to allow bi-directional flow from the grid. In this respect, the NPC is at a disadvantage.

Both topologies presented in Fig. 5-28 would benefit from the PV panels being completely floating, without the connection shown as a dashed line. This is because both strings would deliver at the same time, at all times. By introducing a connection, each string tends to deliver the peak power during only half of the cycle. This is remedied, not without difficulty, by adding the large decoupling capacitors shown. Note that should the panels be left floating, the common mode voltage would be very small, so that the configuration could, in theory, pass safety requirements for leakage current. Unfortunately, only 600V of ungrounded voltage is presently allowed, without incurring much higher costs, due to extra safety precautions. The ground connection, splitting the panels, is therefore non-negotiable. Because of its simplicity and lower conduction loss, the topology on the left, in Fig. 5-28, is adopted here, for comparative analysis.

Because of the lack of an intervening transformer between the PV source and the grid, voltage amplification cannot be performed. This imposes considerable restrictions on the value of operational input and output voltage ranges. When V_{PV} is at its minimum, at 360V, the grid voltage cannot exceed 250V (RMS). Considering semiconductor voltage drops and allowing for 10% dynamic range for the controlling duty cycle, the

design is not feasible for the requirements expressed originally for this comparative study. Either the variability of the PV voltage is in some way narrowed, or the grid voltage must be nominally set to 220V AC, instead of 220V AC – 240V AC. The latter option is adopted here.

5.5.2 Component Design

The obvious presence of the split power source suggests the use, once again, of the half-bridge topology. In this case, however, high voltage IGBTs must be used on the primary side. The DC/DC converter structure would then be as shown in Fig. 5-29.
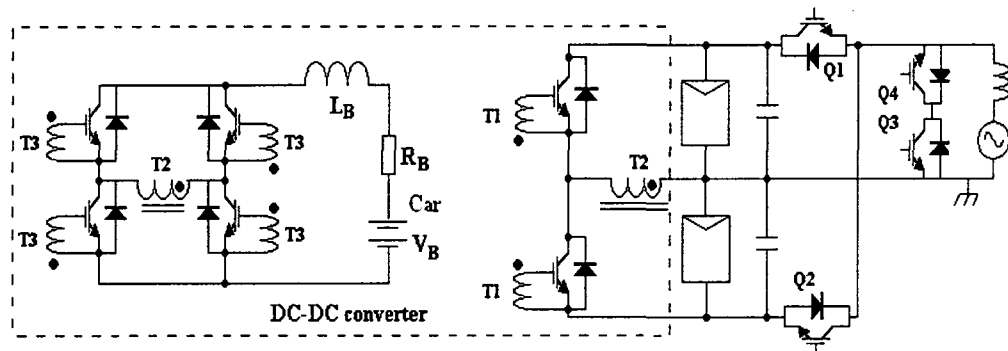
Fig. 5-29 Transformer-less topology showing DC/DC converter

A turns ratio for T2 of 4/5 will guarantee that a 400V battery can be charged when V_{PV} is minimum, at 360V. The inductance L_B is calculated so as to provide $\pm 10\%$ ripple under worst-case; that is, when V_{PV} is maximum, at 500V, and battery voltage is minimum, at 275V. Calculation of the required inductance value is straightforward and yields 1.7mH, at 25 kHz switching frequency. Note that a lower switching frequency has been selected here, compared to the previous topology, because the primary switching devices are less-efficient, high-voltage IGBTs.

5.5.3 Comments

5.5.3.1 Cost

The cost structure for this transformer-less topology proves to be extremely good. The absence of a 60Hz transformer as well as an isolation stage is the obvious strong point. These exists only a slightly offset due to the need for accurate sensing and processing of control variables, in order to maintain DC-current injection within acceptable limits, although some simple transformer-less topologies have been presented in [21] that deal with this problem topologically, rather than through control. Marginally higher costs may further need to be incurred due to the relatively large battery charge inductors (twice as large, compared to the previous topology). Finally, it must be noted that the split PV supply may require additional cost, for current sensing within the MPPT device. The expanded version of the cost matrix of Table 5-2 is depicted in the form of Table 5-3.

Table 5-3 Cost comparison HT transformer vs. Transformer-less vs. Z-converter

Component	Z-converter (LF transformer isolated)	HF transformer isolated	Transformer-less
PV cabling	GOOD	GOOD	GOOD
Transformers	GOOD	BETTER	BEST
Chokes	GOOD	GOOD	POOR
Capacitors	GOOD	GOOD	GOOD
IGBTs	GOOD	POOR	GOOD
Diodes	GOOD	POOR	GOOD
Drivers	GOOD	POOR	POOR
Sheet metal	GOOD	BETTER	BETTER
OVERALL	GOOD	BETTER	BEST

5.5.3.2 Reliability

The transformer-less topology, like the Z-converter, has a low part count and, like the HF isolated topology, has well-controlled stress levels for all devices. Hence, due to these important advantages, the Z-converter depicts superior reliability.

5.5.3.3 Dynamic Behavior, Interaction with PV Source, Interaction with Grid

From the point of view of dynamic response and interaction with the grid, the transformer-less topology is undistinguishable from the HF-isolated topology, as discussed in 5.4.4.3.

5.5.3.4 Design Flexibility

Arguably the weakest point of the transformer-less topology is its inability to adapt itself to different input and output voltage specifications. In fact, for the design presented here, the original grid voltage specification had to be relaxed, in order to allow the use of the assigned PV voltage range.

CHAPTER 6

SIMULATION TEST RESULTS

The PSIM software was used to validate the mathematical model and the overall operation under switch-mode regime. Steady state and transient behavior are verified and efficiency is calculated based on simulation results. It is important to mention that no attempts are made to model the MPPT/PV voltage-current characteristics in detail. Rather, the PV source is represented either as a voltage source, that remains constant under current changes at the MPPT power "knee," or as a diode string fed by a constant current source. One of the main results in [17] is that the MPPT has a fundamental effect on the overall system dynamic response. Therefore, although the simulations below confirm the fully controlled behavior of the converter, actual waveforms will vary in real life applications, depending on the type of MPPT strategy used.

6.1 THE Z-CONVERTER

In 5.3.9.3, the dynamic limitations of the Z-converter were discussed. These will be highlighted in simulations involving changes in PV current demand, battery current demand, and line voltage. However, it is important to appreciate that the SISO linear control methods used in this thesis are probably not the best in terms of dynamic performance. Rather, non-linear feedback and variable decoupling [9] or Sliding Mode Control [16] can improve response time and robustness. Nevertheless, it is demonstrated that more traditional techniques can produce an adequate behavior for this application.

In a system that includes the battery, there exist various combinations of line, PV, and battery voltages and currents that need to be considered. It is not convenient to present simulations for all these possibilities. Instead, typical combinations of critical variables will be used, while a given variable is swept from minimum to maximum level. Thus, in the course of this study, all significant extreme combinations have been simulated successfully using PSIM (electronic model) and SiMetrix (mathematical model), which were found to exhibit good matching.

Note that a specific line-frequency isolation transformer turns ratio was used in the simulations. This ratio must be as high as possible, in order to maximize duty cycle D for improved power transfer. Simply contrasting the minimum input voltage to the inverter bridge ($2V_{c(min)}$-$V_{PV(max)}$ = 1100-500 V = 600V) to the maximum peak of the line voltage (375V), and adding 20% margin for dynamic control of the duty cycle D, immediately yields an optimal turns ratio of 4/3. This is, in fact, the ratio used in all simulations related to the Z-converter, unless otherwise specified.

6.1.1 System without Battery (Scheme 1)

Fig. 6.1 shows the simulated response to a 40% step in input voltage, with 2 different PV voltages, at maximum power generation of 5kW. Note good regulation of V_C. The ripple current drawn from the PV source is approximately 15% of the DC level.
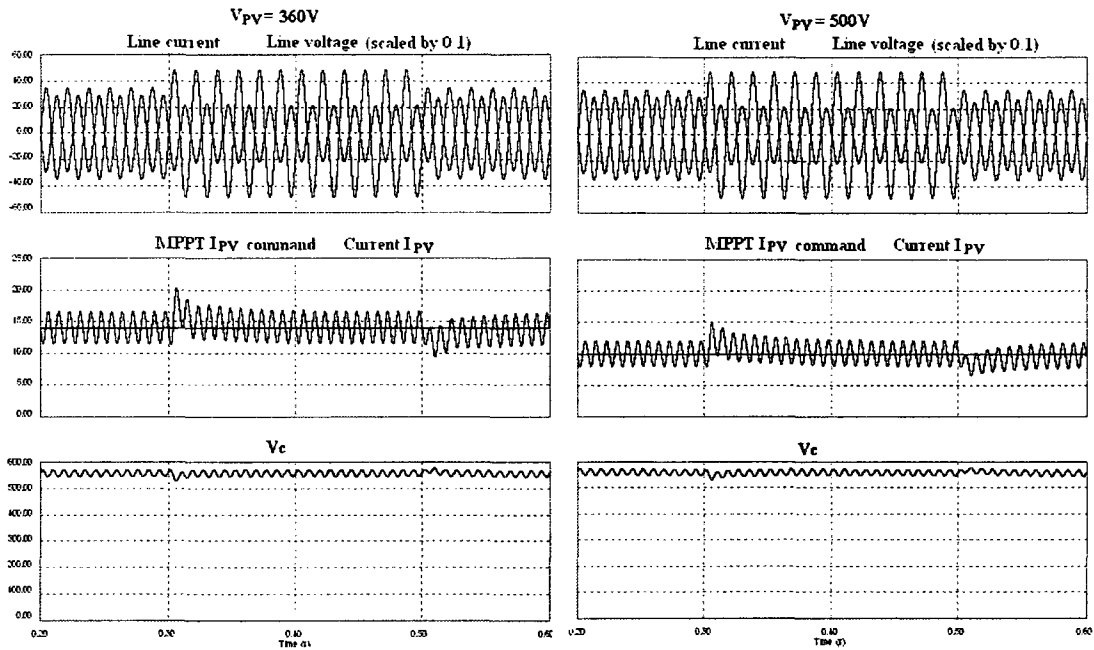
Fig. 6-1 System with no battery; Response to 40% step of input line voltage.
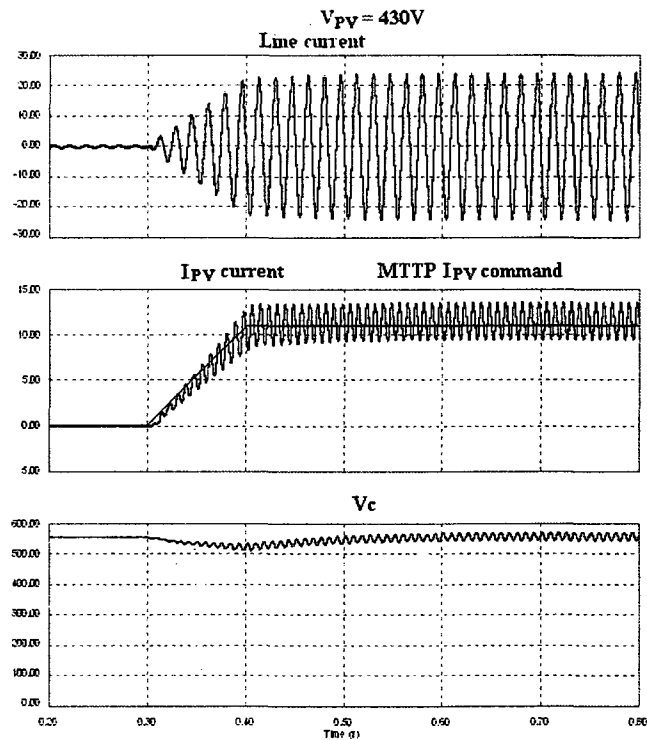
Fig. 6-2 System with no battery; Response to 100% step of MPP I$_{PV}$ command (100ms

transition)

71

The ripple current can be further reduced by increasing the gain of the ripple cancellation amplifier, at the expense of low frequency harmonic distortion of the input current. Fig. 6-2 shows the response to a 100ms transition of the PV power output. The result is acceptable, considering that 100ms is reasonably fast for an MPPT, tracking changes in irradiation.

6.1.2 System with Battery (Scheme 1)

Fig. 6.3 shows the response of the input current, PV current, and battery charge current to a 100% variation in MPPT current demand, in 100ms. The battery demand is kept constant at 2.5kW, so that at the beginning of the transition, the grid delivers power to the battery, and at the end of the transition, it absorbs power from the PV. This is clear from the phase reversal of the input current.
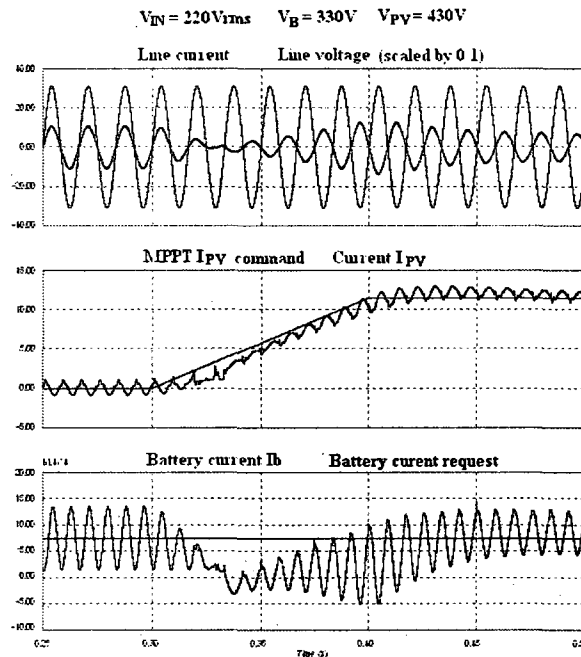
Fig. 6-3 System with battery; Response to 100% step of MPPT I_{PV} command (100msec transition)

Note that the battery charge current is disturbed for approximately a mere 50ms. Fig. 6.4 shows the typical behavior, following a 40% step in input voltage. The fast response of the input current loop produces predictably good results.
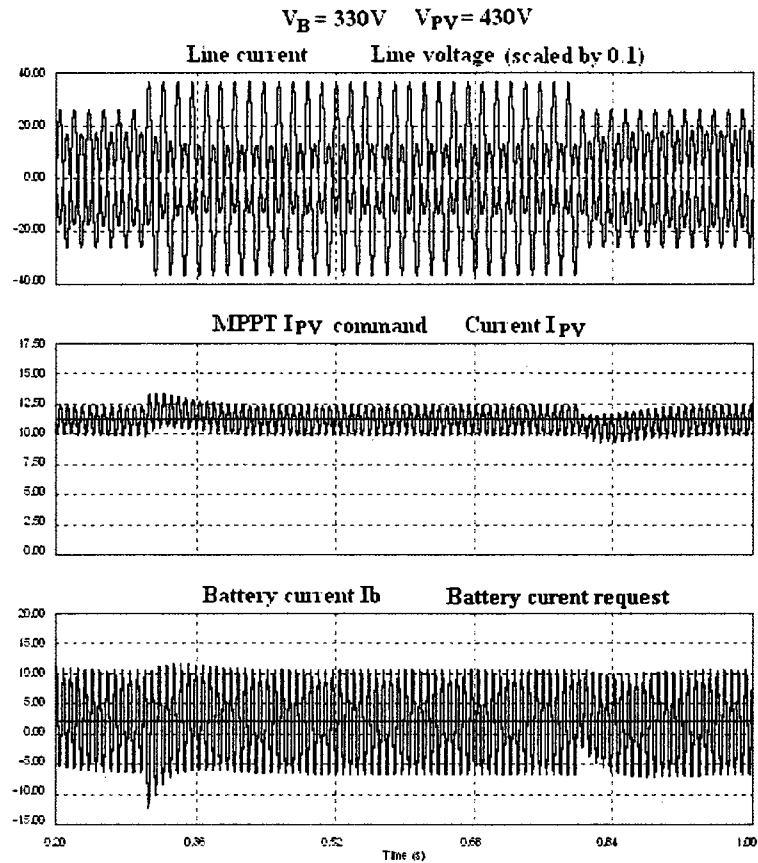
Fig. 6-4 System with battery. Response to 40% step of input line voltage

Finally Fig. 6-5 shows the response to a 1 Amp/sec change in battery charge current demand. Again, in this case, the grid changes from absorbing to supplying power. Note that the battery current cannot follow the changing demand voltage during the transition, due to the suppressed gain of the error amplifier. However, the current is still maintained at a safe level. In addition, Fig. 6-5 also depicts the same simulation run on SiMetrix, which strictly represents the average (mathematical) model. The match

between the two simulations is a good indication that the derived mathematical models are fundamentally correct. This is indeed the case; the very minor differences in amplitude of the 120 Hz ripple and response can be attributed to the time step limitation of the PSIM engine as well as some simplifications used in modeling the state-space equations in SiMetrix.
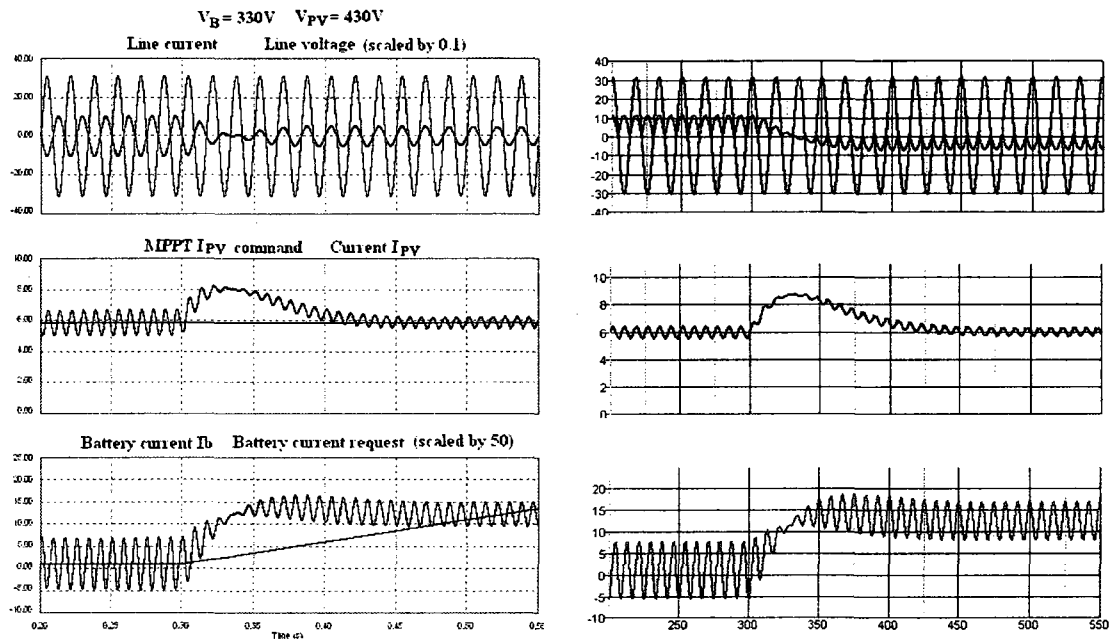
Fig. 6-5 System with battery; Response to a ramp in I_B demand; PSIM (left) and

mathematical model set in SiMetrix (right)

The last simulation presented here corresponds to the atypical case, where the grid is fed by both the PV source and the battery as it discharges. In this case, battery average current will be negative. Note that the power levels are more or less accurate: the battery discharge power is 3.3kW, and the PV power is 1.4kW, for a total of 4.7kW.
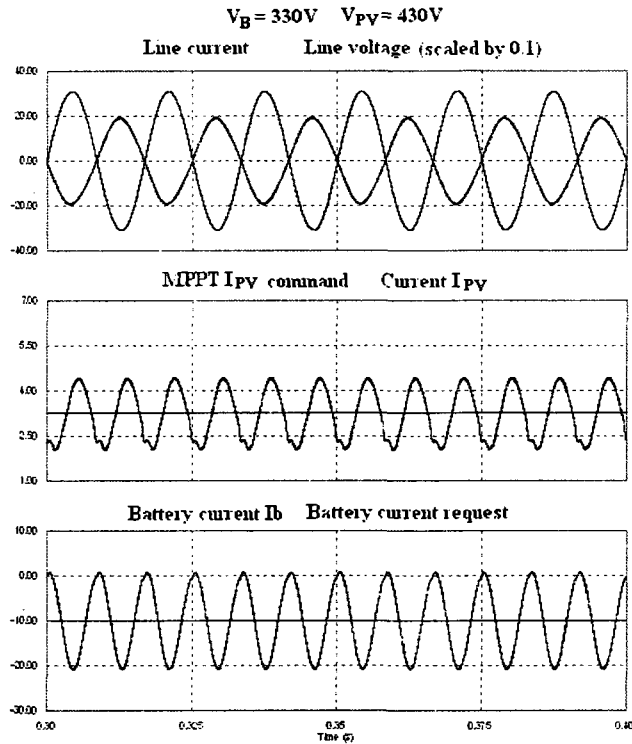
Fig. 6-6 System with battery; Battery discharges to provide grid power.

From Fig. 6-6, the power absorbed by the grid is found to be approximately 4.25kW, for a conversion efficiency of 91% (note that a factor of 1.33 must be used for the current waveform, due to action of the line transformer with its specific turns ratio).

6.1.3 System with Battery (Scheme 2)

If the design demands addition of a large capacitor at the PV terminals, in order to absorb the power ripple, the ripple cancellation circuit discussed in 5.3.8.5 could be eliminated. At the same time, the battery charge current control loop must be set to have appreciable gain at 120 Hz, in order to regulate out the ripple (5.3.8.5 and 5.3.8.9). This will redirect the ripple current from the battery to the PV; at the same time, the battery circuit becomes faster and more efficient. Using Scheme 2, Fig. 6-7 (left) becomes the

counterpart of Fig. 6-3. While the line current behavior is similar, it is evident that the

ripple content has been successfully transported from the battery to the PV source.
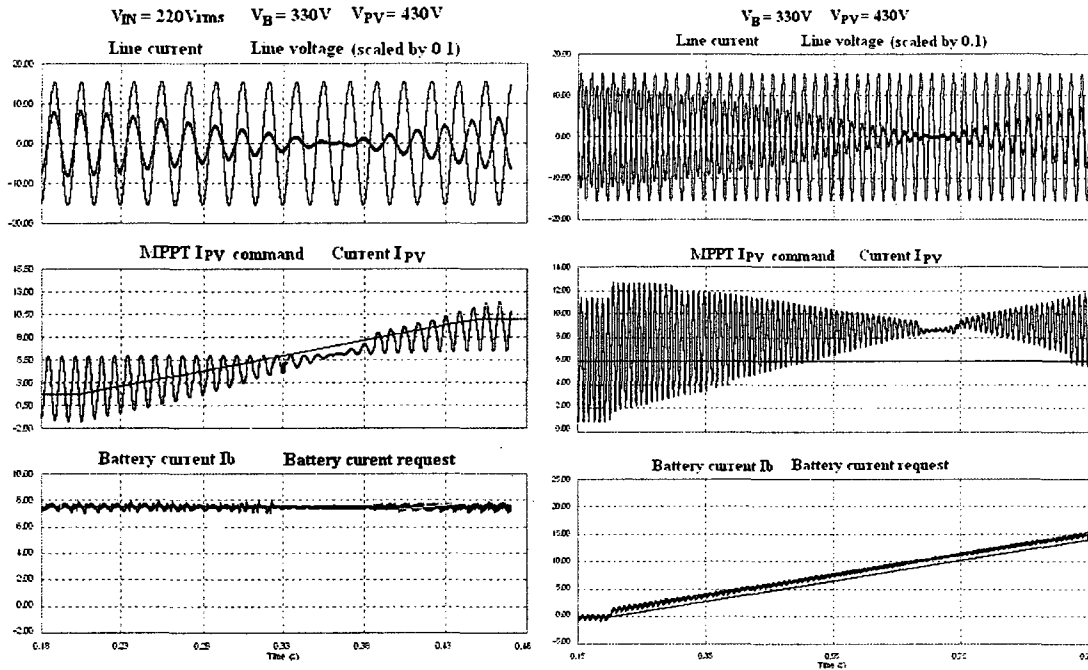
Fig. 6-7 System with battery; Response to 100% step of MPPT I$_{PV}$ command (200ms

transition) (left); Response to a 20A/sec ramp in I$_B$ demand (right)

The counterpart of Fig. 6-5 for Scheme 2 is Fig. 6-7 (right). Note that the battery

current command can be made to change much faster than that of Scheme 1.

6.1.4 I$_{PV}$ Ripple, PV Utilization Ratio, and MPPT

From the simulation results discussed above, it is safe to state that the Z-converter

fulfills all general requirements stipulated at the start of this study. However, three

specific outcomes are definitely less than desirable. The slow response of the battery

current loop as well as the high ripple in the battery has been mentioned. The third

drawback is the rather large 120 Hz ripple drawn from the panels that cannot be

completely eliminated, despite the added control mechanisms, which in turn is much

worse under Scheme 2. The presence of a ripple is not, in itself, a thoroughly objectionable occurrence. For instance, reference [22] draws on the switching ripple to perform the MPPT function. Reference [23] applies the same principle to the 120 Hz ripple for single-phase systems – this being more applicable to this present work. The problem lies in the extent of switching ripple present, especially at lower currents.

Fig. 6-6, for example, shows a 30% peak ripple. The utilization ratio, K_{PV}, is defined as the ratio of actual average power drawn from a PV source to the ideal maximum power achievable in the absence of ripple. Utilizations of more than 98% are good. However, they can be achieved only with voltage ripples of less than about 8.5% [24], corresponding to yet lower current ripples. Even in Scheme 1, it is well worth considering adding a relatively small decoupling capacitor across the PV source. A 100μF/600V capacitor, for instance, would only have 1/30th the CV product of the Z-circuit capacitors, so that a film capacitor can be employed to maintain reliability, assuming size is not an issue.

In order to study the performance of the PV with the addition of this power decoupling capacitor (using the same example of 100μF), a set of simulations using SiMetrix is performed, and the utilization factor is plotted and compared for different operating regimes. For this purpose, an ideal MPPT scheme is assumed, and the simulated values for I_{PV} under worst-case conditions are applied. Earlier simulation work reveals that the worst case condition for I_{PV} ripple occurs during the atypical case of battery discharging to the grid, with maximum V_{PV} = 500V. These conditions produce approximately a 1A peak ripple for all values of I_{PV}. For the simulation, a bare-bone model of the PV panel, as shown in Fig. 6-8, is used, where the model diodes are general

purpose 20A/1000V silicon type. Note that the absence of any series resistance will maximize ripple, representing worst case.
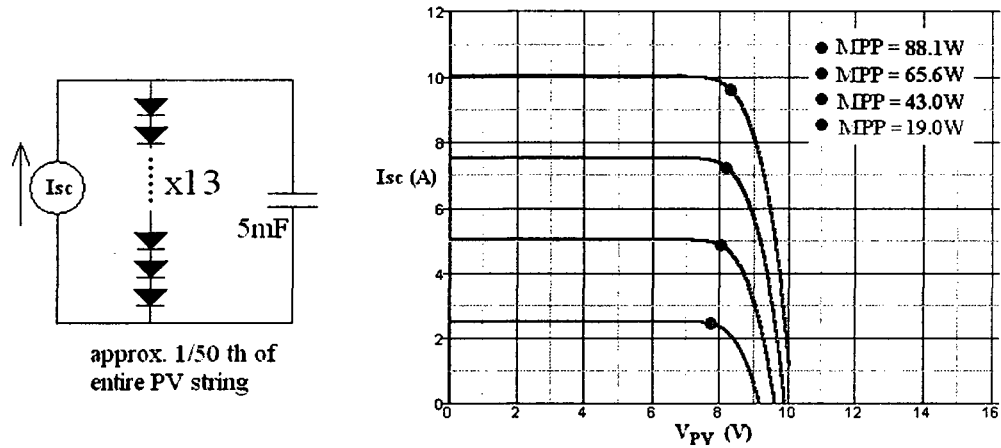
Fig. 6-8 I-V Characteristics of simulated solar panel (1/50th of entire string)
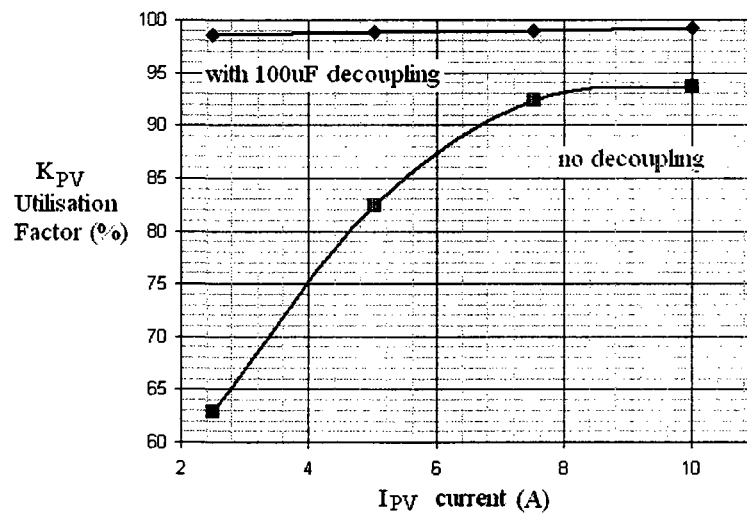
Fig. 6-9 Effect of capacitive decoupling on PV utilization factor for Scheme 1

From Fig. 6-9, it is clear that unless the PV is used only with high levels of irradiance, a relatively small decoupling capacitor is necessary; even in Scheme 1. This capacitor then, rather than being added, simply replaces the one already present that is needed for absorbing the HF switching current to the Z-circuit.

For Scheme 2, the ripple into the PV source is much higher than that discussed above. The worst case obviously occurs when the battery receives the full 5kW from the grid, with a minimum PV voltage of 360V. Thus, $I_{PV} = \dfrac{P_G}{V_{PV}} \sin(2\omega t)$, where P_G is the grid power (5kW). The peak ripple is then found to be 13.9A. Simulations with SiMetrix, using this current and the same model shown in Fig. 6-8, indicate that a 1mF capacitor is needed to keep the voltage ripple below approximately 5% peak, thus providing a utilization factor higher than 98%. This capacitor must be rated at 500V; the CV product is then higher than that of each of the Z-circuit capacitors.

6.1.5 Power Loss (Efficiency)

Power loss within the converter will be calculated using Scheme 1 for reference and by considering the following loss contributors:

a)   IGBTs (conduction and switching)

b)   IGBT body diodes

c)   Magnetics (conduction loss)

The results from the simulations will be used to describe all relevant RMS currents for the magnetic conduction losses, average currents for diodes, and IGBT conduction losses, as well as instantaneous currents and voltages for switching losses. Core loss for the inductors can be set arbitrarily small, if size concerns are less important, especially if many turns are needed to achieve the ESRs for better damping of the Z-circuit; they will not be considered here. For comparison purposes with other topologies, common commercially available semiconductor devices with equivalent chip-size will be chosen *ad hoc* for each topology. In the case of the Z-converter, the chosen IGBT will be

the IRG4PH50U. The relevant parameters from the datasheets are: IRG4PH50U: On-state = 3V @20A, E_{on} = 160uJ @1200V, E_{off} = 1.8mJ @1200V, 20A.

As a first degree of approximation in the power loss calculations, the on-state voltages for the IGBTs and diodes will be kept constant at all currents. As such, PSIM can directly estimate all conduction losses. Unfortunately, this is not the case for switching losses. They will be calculated indirectly, by assuming that the switch-on loss energy, E_{on}, increases with the square of the switching voltage for IGBTs. Conversely, the switch-off energy for the IGBTs, E_{off}, is assumed to increase linearly with switching voltage and current. With this postulation, PSIM can calculate switching losses, starting with the instantaneous peak currents and voltages, by applying the formulae 6-1 and 6-2.

$$Psw_{ON} = \frac{2f_G f_{SW} Eon}{V_R^2} \int_0^{\frac{1}{2F_G}} V(t)_{pk}^2 dt \tag{6-1}$$

$$Psw_{OFF} = \frac{2f_G f_{SW} Eoff}{V_R I_R} \int_0^{\frac{1}{2F_G}} V(t)_{pk} I(t)_{pk} dt \tag{6-2}$$

Here, $V(t)_{pk}$ and $I(t)_{pk}$ are the instantaneous switch voltage and current, f_G is the grid frequency, f_{SW} is the switching frequency, while V_R and I_R are the rated voltage and current. E_{on} is the switch-on loss, calculated at V_R, and E_{off} is the switch-off loss, calculated at V_R and I_R.

Before continuing with the power loss estimation, it is worth highlighting the switching sequence in the inverter bridge. In fact, switching losses can be minimized when a proper sequence is chosen, even without resorting to more sophisticated circuitry [25]. This can be done with no compromise on the harmonic distortion, by keeping the active state centrally placed within the cycle [26]. Also, given that the shoot-through

states are responsible for the HF ripple on the Z-circuit inductors, they can be split evenly on either side of the active states, effectively doubling their frequency. Finally, as is usually preferable, only one of the four devices should need commutation, to obtain a state transition. The sequence shown in Fig. 6-10 possesses all the requirements, and is relatively simple to implement using analog carrier-based methods.
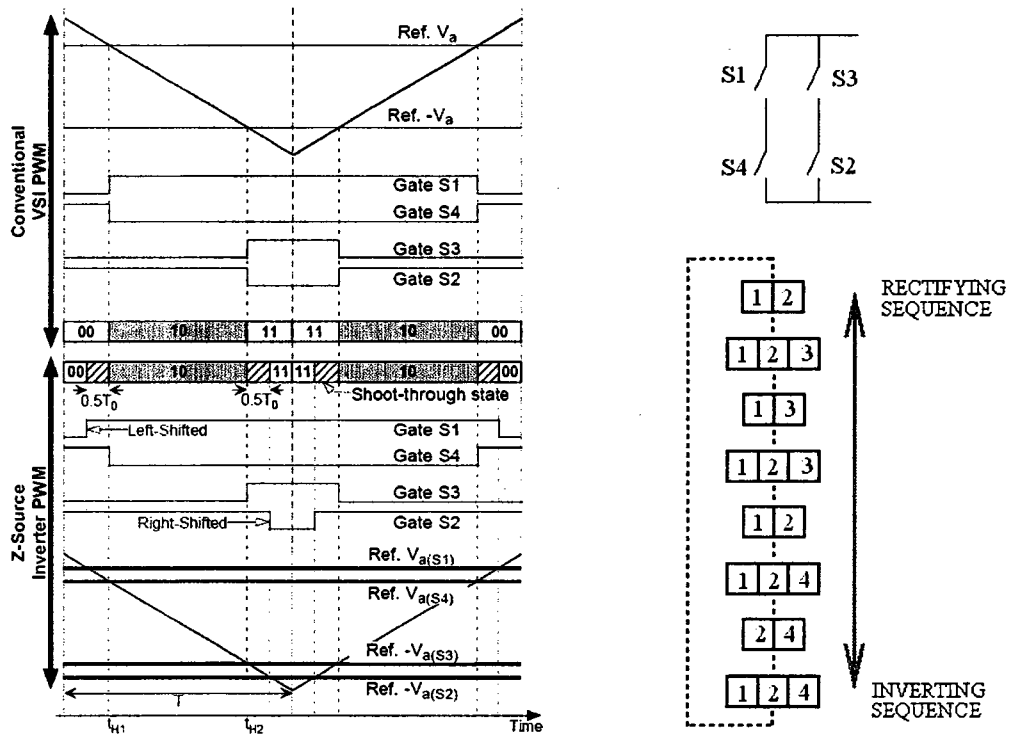
Fig. 6-10 Chosen switching sequence [27].

The most immediate result from Fig. 6-10 that affects power loss calculation is the fact that only one turn-on and one turn-off transition exists per switch and per switching period, even though these are "hard switching" transitions. The above statement is true for both line half-cycles. The manner in which the losses are estimated with PSIM will be demonstrated below in detail, for the input bridge. This procedure will then be repeated for all other devices; only the final results will be reported hereafter. Fig.

6-11 shows the pertinent waveforms for one of the bridge IGBTs. The operation considers no battery, and 5kW generated power.

IGBT current

IGBT current running average of conduction loss

Running integral of $(2Vc-V_{PV})^2$ (valid for both half-cycles)

■ Running integral of $(2Vc-V_{PV})(2I_L)$ (valid for only one half-cycle)
■ Running integral of $(2Vc-V_{PV})(2I_L - I_{IN})$ (valid for only one half-cycle)
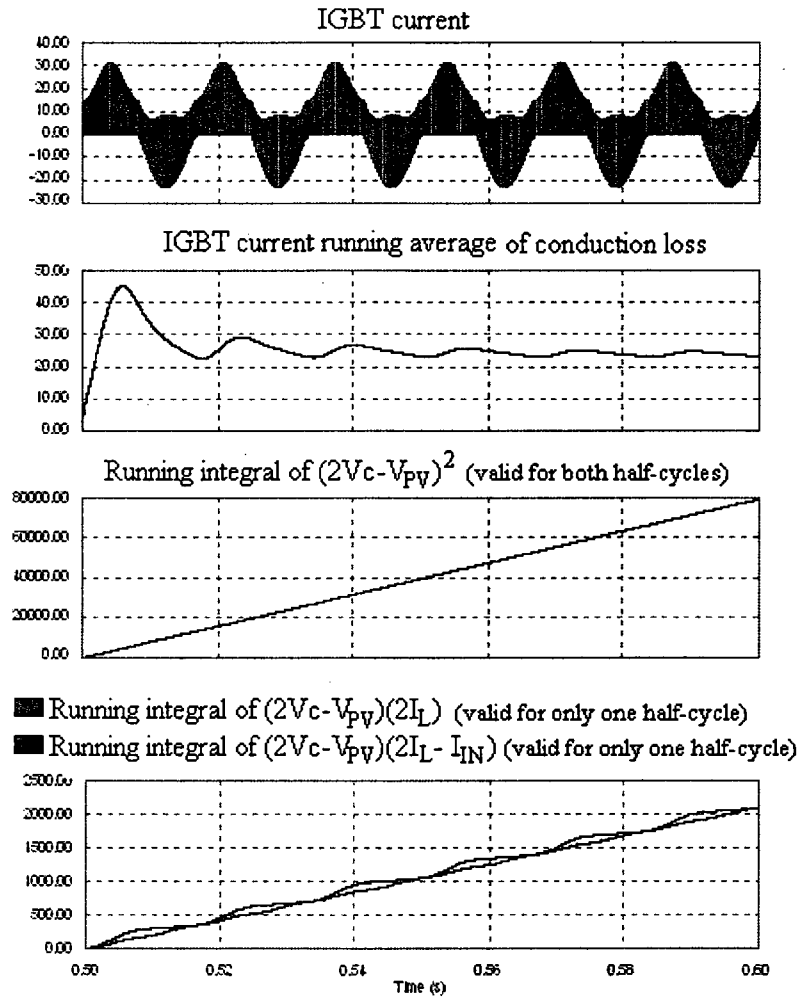
Fig. 6-11 Bridge IGBT power loss waveforms

The second graph (from top) of Fig. 6-11 is simply the running average of the conduction loss. It will converge to the average value of 24W. The third graph (from top) is used to calculate the turn-on loss; its increase over a ½ cycle represents the definite integral in Eq. 6-1; in this case, it has a value of 6600 V^2sec. Thus, the result of Eq. 6-1 can simply be estimated as 2.20W. The same idea is used to compute turn-off losses,

using the fourth graph (from top) and Eq. 6-2. The red trace is used over the ½ cycle when the IGBT current is positive and the blue trace over the ½ cycle when the anti-parallel diode conducts. The result is a total turn-off loss of 27.1W. The overall loss for a bridge IGBT is 53.3W. As there are 4 IGBTs, these losses already amount to about 4% in efficiency loss.

Continuing with the loss evaluation, the DC blocking IGBT was found to dissipate a total of 17.1W, which is less than that for bridge IGBTs, because of zero-current turn-off. The MOSFETs used for the DC/DC converter do not really need to be simulated in order to estimate their power dissipation. Those on the Z-circuit side operate in ZVS, while those on the battery side are not active during charging, due to the conduction of the body diodes. It will be shown here that their loss is rather small. For example, for the FCB20N60 MOSFETs: $R_{ds,ON} = 0.15\Omega$, $E_{on} = 80\mu J$, $E_{off} = 40\mu J$ @ 1000V. The RMS currents are calculated using Eq. 6-3 and 6-4. For a battery current of 15A, the total dissipation from all MOSFETs can be calculated at approximately 24W. However, in the case being discussed here, the system does not include the EV battery. Hence, the dissipation is obviously zero.

$$Ib_{p(RMS)} = \frac{Ib}{2\sqrt{2}} \qquad\qquad (6\text{-}3)$$

$$Ib_{s(AVG)} = \frac{Ib}{2} \qquad\qquad (6\text{-}4)$$

Here, $I_{bp,RMS}$ is the RMS current in the Z-circuit side MOSFETs (0.15Ω) and $I_{bs,AVG}$ is the average current in the battery side MOSFET body diodes (0.9V on-state voltage, at 20A).

Next, it is important to record the dissipations in the chokes and capacitors. These components possess high ESRs through design, because of damping requirements; the dissipations are expected to be high. Again PSIM is invoked to calculate RMS currents. From Fig. 6-12, the RMS currents in L, L_{IN}, and C can be estimated at 12.2A, 15.3A, and 9.8A, respectively, corresponding to a total loss of 39.0W.

The last critical component that needs to be considered is the 60 Hz isolation transformer. Again, if size and cost concerns are ignored, this component can be made arbitrarily efficient. Nevertheless, even when some compromises are made, due to real-world constraints, an efficiency of 98% is reasonable for this part.

The final estimate of all losses treated above, for operation without the EV battery, can finally be completed. The losses amount to approximately 370W of dissipation. Hence, the corresponding efficiency is estimated at 93.1%.

Table 6-1 Sample power loss mapping for Z-converter

Bridge IGBTs	DC Block IGBT	Z-inductors	Z-capacitors	Input Inductor	Transformer
213.2W	17.1W	8.9W	23.0W	7.0W	100W

Typical efficiency without battery: 93.1%   (V_{IN} = 220V RMS; V_{PV} = 430V)

Z-inductor current I_L (A)

Running rms of Z-inductor current

Line Filter Inductor Current I_{IN} (A)

Running rms Line Filter Inductor Current

Z-capacitor current (A)

Running rms of Z-capacitor current
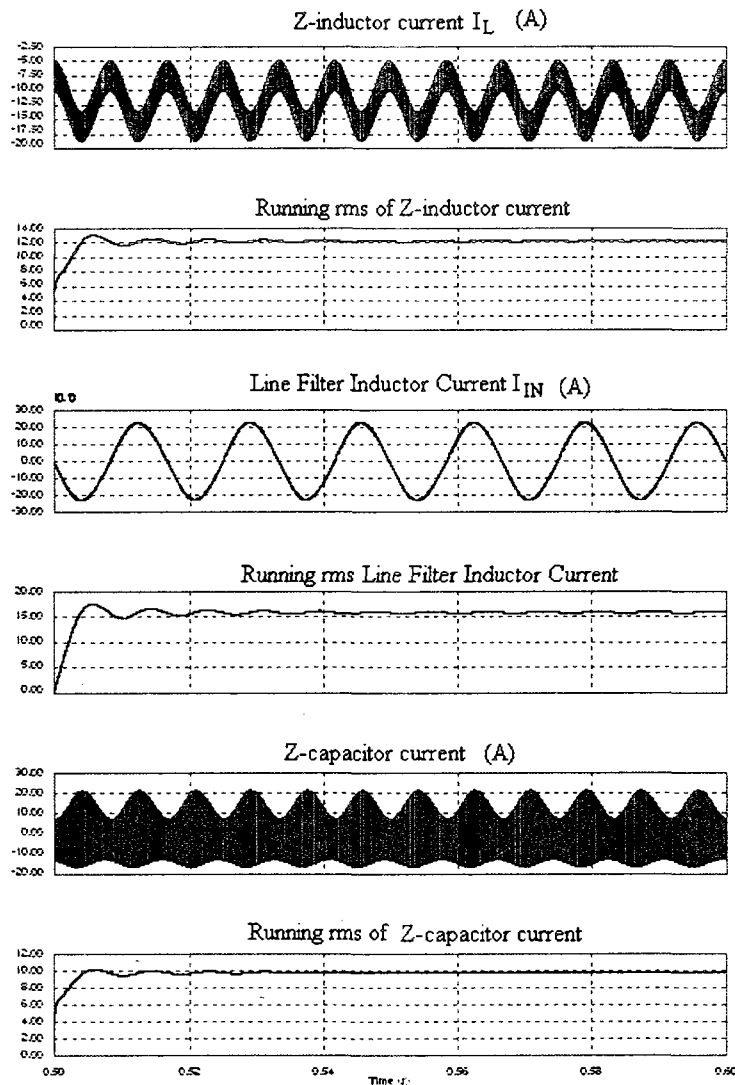
Fig. 6-12 RMS current estimation for inductors L, L_{IN}, and capacitor C

The same PSIM-aided procedure described above can be applied to other significant simulations; the results for typical and worst-case operations with battery are reported below. However, more detailed numbers relative to all 4 power flow paths can be found in APPENDIX C. Note that efficiency is defined as the ratio of the sum of the powers delivered to the grid as well as to the battery to the power generated by the PV panel.

Table 6-2 Sample power loss mapping for Z-converter

Bridge IGBTs	DC Block IGBT	Z-inductors	Z-capacitors	Input Inductor	Transformer
188.0W	16.5W	3.6W	19.5W	1.8W	50W

Typical efficiency with battery: 94.7% (V_B = 330V, V_{IN} = 220V RMS, V_{PV} = 430V, I_B = 7.5A).

Table 6-3 Sample power loss mapping for Z-converter

Bridge IGBTs	DC Block IGBT	Z-inductors	Z-capacitors	Input Inductor	Transformer
308.0W	19.3W	12.4W	35.8	10.1W	100W

Worst-case efficiency: 91.1% (V_B = 400V, V_{IN} = 180V RMS, V_{PV} = 360V, I_B = 0A).

Note that worst case condition is low input line and panel voltage ,with power flow from panel to grid.

6.1.6 Efficiency Results for Alternate Z-converter-based Topology

In view of the efficiency results, a different configuration for the Z-converter could be proposed. In fact, in related literature, the Z-converter has been acclaimed as an excellent method for obtaining buck-boost performance, for dealing with variable sources such as PV and fuel cells. Buck-boost operation is controlled by D and D_o and can, thus, be optimized. Instead, in the Z-converter configuration that was analyzed in this thesis, D_o was used in a novel fashion, for control of the EV battery current, so that it cannot be utilized for other purposes. For instance, this leads to the need for high-voltage devices in the inverter bridge that tend to be less efficient than lower-voltage devices. Consider the configuration evolution shown in Fig. 6-13. D_o is adjusted using Eq. 5-1 and Eq. 5-2 to keep inverter input DC voltage below 600V; this voltage being the threshold level for

extremely efficient commercially available devices. On the other hand, the DC/DC converter in this new case is regulated, and thus, incurs higher losses, including switching loss and higher conduction losses, if MOSFETs are used. Moreover, a much larger smoothing inductor is needed, increasing the losses further. Thus, a popular controlled half-bridge, driven from a 430V source using IGBTs, amounts to a nominal efficiency of 97%.
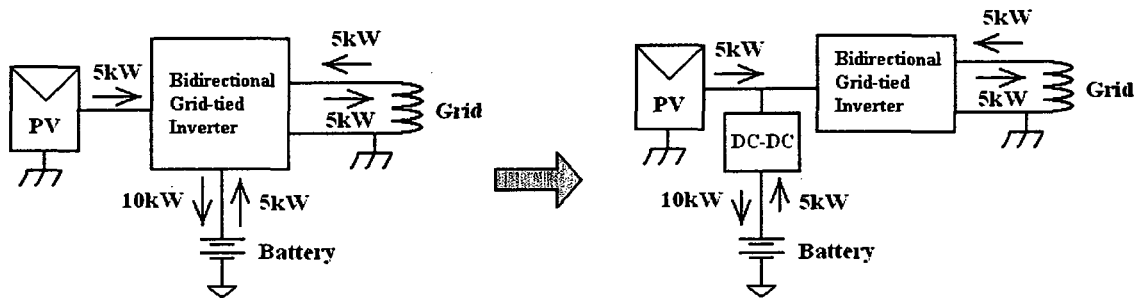
Fig. 6-13 Original (left) and alternate configuration (right) for Z-converter

Then, in the case where the full power from the PV is directed to the battery, 97% will obviously also be the total efficiency, constituting the best-case scenario. For comparison, two alternative operating regimes were simulated in PSIM, and the losses were evaluated. Note that, in this case, the choice for the transformer turns ratio is dictated by the ranges of the PV and grid voltage, the requirement of IGBT rated at less than 600V, as well as the allowance for some dynamic range for control variable D. The new turns ratio is 1:0.94, compared to 1:1.333. The chosen devices are: IRG4PC40W: On-state = 2.5V @ 25A, E_{on} = 170μJ @600V, E_{off} = 380μJ @600V, 25A; FCB20N60: $R_{ds,ON}$ = 0.15Ω, Eon = 80μJ, E_{off} = 40μJ @ 1000V; STTH15L06: On-state voltage = 1.0V.

Table 6-4 Sample power loss mapping for alternate Z-converter topology

Bridge	DC IGBT	Z-inductors	Z-capacitors	Input Inductor	DC-DC Conv.	Transformer
66.2.0W	6.4W	4.3W	4.2W	5.4W	87.0W	50W

Typical efficiency with battery: 95.7% ($V_B = 330V$, $V_{IN} = 220V$ RMS, $V_{PV} = 430V$, $I_B = 6A$).

Table 6-5 Sample power loss mapping for alternate Z-converter topology

Bridge IGBTs	DC Block IGBT	Z-inductors	Z- capacitors	Input Inductor	Transformer
205.0W	16.4W	18.2W	22.1	26.3W	100W

Worst-case efficiency: 92.8% ($V_B = 400V$, $V_{IN} = 180V$ RMS, $V_{PV} = 360V$, $I_B = 0A$).

As can be seen, the alternate configuration can deliver efficiencies that are 1% higher or more, at both nominal and worst-case operation. On the other hand, the use of 600V devices is marginal and may not be possible in real systems. This is because D_o must still be partly modulated, to attenuate PV ripple in Scheme 1; this dynamic requirement imposes a minimum DC value of 0.1 on D_o, which pushes the minimum Z-capacitor voltage to nearly 560V and the corresponding IGBT voltage to about 620V. In addition, this topology cannot be considered "single-stage," and as such, requires additional control for EV battery charging as well as related driver circuits. Nevertheless, it was included briefly in this study, for comparison purposes.

6.1.7 Conclusion

Simulations confirm the mathematical model developed previously for the Z-converter (see Fig. 6.5), especially the relatively sluggish behavior of the battery current regulation loop in Scheme 1. Apart from this drawback, the converter performs

satisfactorily, as expected. It was found that a mid-sized decoupling capacitor, in the order of 100μF, is needed in Scheme 1, in order to eliminate the strong interaction with the PV I-V characteristics. However, this addition is rather small, and does not contradict the original cost and reliability premises. In Scheme 2, this capacitor must be much larger (about 1mF), in order to achieve the same MPPT performance. Because this is very likely to be an electrolytic capacitor, reliability and cost are affected.

The power losses were estimated directly (conduction losses) or indirectly (switching losses) through PSIM, following a simple method, and provide a fairly good idea of the overall efficiency, especially for comparison with other topologies. Even considering a worst-case number, and for a seldom used power flow path, the efficiency of about 91% is somewhat disappointing for a single-stage topology. This can be attributed to the unavoidable use of high-voltage devices, with their poorer performance in terms of conduction and switching loss, as well as the presence of the 60 Hz transformer.

An alternate topology was briefly considered, to allow the use of more efficient, lower-voltage devices. Indeed the efficiency can be improved by 1% or so, but other technical difficulties arise.

6.2 HIGH-FREQUENCY TRANSFORMER–ISOLATED TOPOLOGY WITH DC-LINK

The topology, as described in 5.4, is rather uncomplicated. The dynamic behavior can be closely associated to that of the DC/DC buck converter, for the EV battery charger and voltage-fed inverter (another form of the buck converter), for the line conditioner. Because these are well known and loop compensation is straightforward, simulation

results relating to the dynamic response will not be shown here. In fact, comparable results will be shown in section 6.3, when discussing the transformer-less topology, which is also based on the buck design; similar performance can be expected for the HF transformer-isolated topology.

The efficiency estimation for typical operation, based on the PSIM simulations, are summarized in APPENDIX C and Fig. 7-1. Although Table 6-6 reports that the worst-case condition for this topology includes the grid to EV battery power flow path, the reverse flow (battery to grid) is actually worse, by approximately a percentage point. However, this scenario is not considered, because this path can be considered atypical, or nearly anomalous. However, the heat sinks and power devices must be sized accordingly.

Table 6-6 Sample power loss mapping for HF transformer-isolated topology

Bridge IGBTs	DC-DC IGBT	Diodes	Chopper IGBTs	Inductors	HF Transformer
145.6W	172.3W	0W	0W	57.9W	50W

Worst-case efficiency with battery: 92.1% ($V_B = 275V$, $V_{IN} = 180V$ RMS, $V_{PV} = 360V$, $I_B = 18A$).

The grid to battery path, quantified in Table 6-6, is a more critical path than the one corresponding to the worst case for the Z-converter. Hence, the Z-converter is better optimized for this application. However, the efficiency number itself is higher for the HF-isolated topology.

6.3 TRANSFORMER-LESS TOPOLOGY

As is the case for the HF transformer-isolated topology, no AC analysis is presented, due to the simple and thoroughly well-known transfer functions that can be

expected from the buck converter. It will be proven that the transformer-less topology, comprising of two power conversion stages, provides a superior dynamic performance. Again, modeling and simulation results are also used to estimate losses. Note that the same bare-bone model for the PV panel, used in section 6.1.4, is also used here.

6.3.1 Dynamic Behavior

Figs. 6-14 and 6-15 immediately confirm that the dynamic behavior is excellent, as expected.
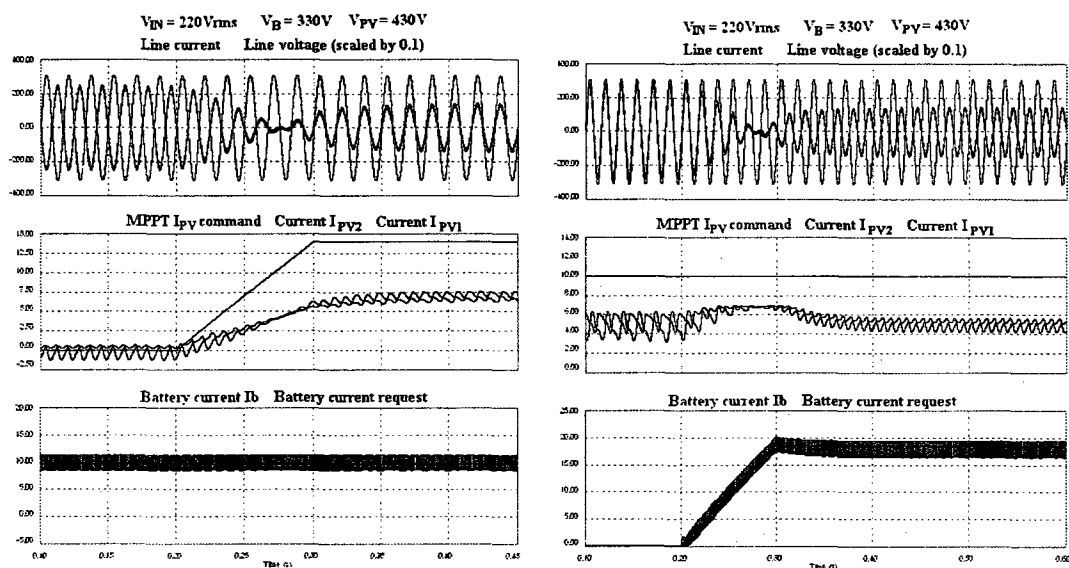
Fig. 6-14 System with battery; Response to 100% step of MPPT I_{PV} command (100ms transition) (left); Response to a ramp in I_B demand (100msec transition) (right)
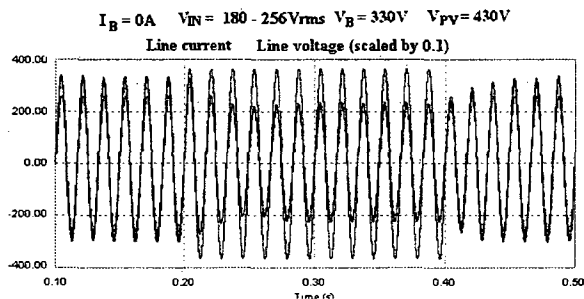
Fig. 6-15 System with battery; Response to 40% change in grid voltage

Fast changes in commands (<0.1 sec) from the battery charger and the MPPT scheme, as well as the line voltage, are serviced cleanly and promptly by the control loops. As mentioned earlier, similar results can be expected for the HF transformer-isolated converter.

6.3.2 Efficiency

Typical efficiencies for all modes of operation are found in Fig. 7-1 and APPENDIX C. The worst-case condition is again grid to EV battery. However, the results are significantly better than the proposed alternatives.

Table 6-7 Sample power loss mapping for the transformer-less topology

IGBTs	DC-DC IGBT	Diodes	Transformer	Inductors
89.9W	92.3W	37.1W	50W	48.9W

Worst-case efficiency with battery: 94.0% ($V_B = 275V$, $V_{IN} = 180V$ RMS, $V_{PV} = 360V$, $I_B = 18A$).

CHAPTER 7

SUMMARY, CONCLUSIONS, AND FUTURE WORK

7.1 SUMMARY

In the first part of this thesis, the basic physical and electrical requirements for a PV-powered, grid-connected, electric vehicle public charging facility were defined. This process was partly based on known "hard" facts, such as safety constraints, the state of the art in solar energy production, and present trends in electric and plug-in hybrid electric vehicle technology. However, the full set of specifications was complemented by requirements that will depend on future market and technological trends, government action, and regulatory agencies, that are far more ambiguous at present. For instance, PV efficiencies might rapidly improve to the point that higher charging powers may warrant 3-phase connections.

Other possible outcomes include the possibility that direct DC battery charging may never be broadly implemented on EVs, or the fact that utility companies and safety agencies come to fully accept transformer-less topologies as the norm. Because all of these prospects as well as future possibilities could markedly enhance the significance of the findings in this thesis, or possibly also render them obsolete, it is important to remark that some outcomes have independent merit. For example, the Z-converter was shown to be a credible topology for any AC-fed application, where bi-directionality and energy storage are involved. Apart from PV systems, this could include microgrids and electric and hybrid electric vehicle propulsion applications.

The second part of this thesis established that the Z-converter could provide controlled and stable power conditioning for all 4 power flow paths, utilizing a single stage of conversion. Moreover, it was also demonstrated that the power ripple generated at the single-phase grid connection could be managed and redirected to either the EV battery or a decoupling capacitor, based on the design alternative. The AC analysis confirmed that the presence of the Z-circuit resonance and the 2-variable control is a source of much complexity in the design process, as well as modest dynamic performance, when linear control is applied.

Despite the single conversion stage, reliability, rather than efficiency or cost, is the strong point of the Z-topology. While the critical component count remains low, efficiency is strongly affected by the presence of the line-frequency isolation transformer, virtually eliminating the gains due to the single-stage topology. Fig. 7-1 shows a comparison of typical efficiencies for the three topologies, analyzed in all 4 operating modes (see APPENDIX C for data). The Z-converter is inefficient when operated directly as a grid-tied inverter. However, this mode of operation only ranks third in order of importance. In the critical PV to battery, and grid to battery modes, the Z-converter is quite competitive with the other topologies. However, the Z-convetrer does not have a comprehensible advantage. On the contrary, the transformer-less topology has low component count, for low cost and high reliability, and is very efficient in all modes of operation.
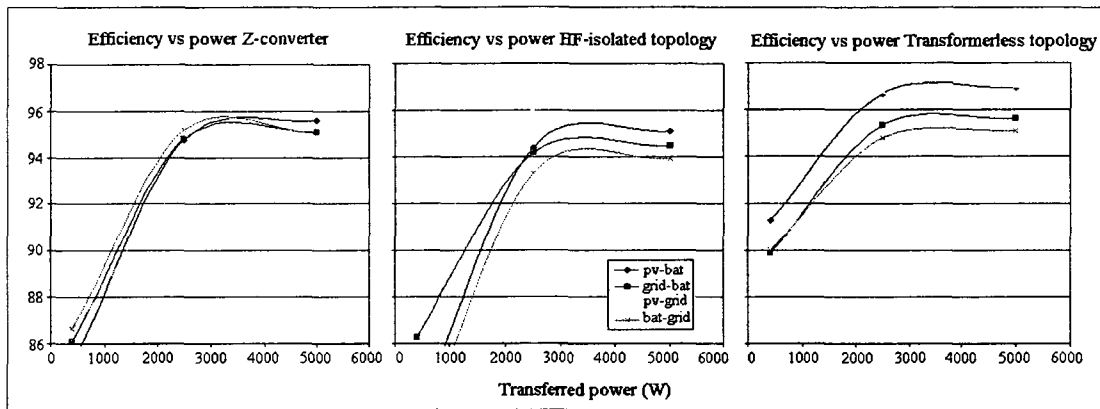
Fig. 7-1 Efficiencies under different operating regimes from three topologies

Unfortunately, the transformer-less topology is not very adaptable to wide input, output, and battery voltage ranges. If a transformer-less topology cannot be used, the HF-isolated topology can be exploited instead, due to its inherent low cost. The efficiency plot for the HF isolated topology is shown in Fig. 7-1. While the overall efficiency can be improved by decreasing the switching frequency of the DC/DC converter, at the expense of size, the reliability will still remain a problem, mainly due to the higher component count. Again, this major drawback points towards the Z-converter proving to be a viable option, especially considering the fact, that its moderately poor PV and battery system dynamic responses are not critical for this application.

Another way to compare the topologies is by means of the Switch Utilization Ratio (SUR). When operated at full battery load (5kW from the grid and an additional 5kW from PV panels, with nominal PV, battery, and grid voltages), the Z-converter was found to exhibit the highest SUR of 0.139, compared to 0.134 and 0.119, for the transformer-less and HF-isolated topologies, respectively. This underlines the effectiveness of the Z-converter in this application. Thus, the only truly outstanding concern is the cost of the high efficiency 60 Hz isolating transformer, perhaps making the

95

Z-converter exploitable, only when such a transformer is imposed by other, less technical governing factors.

7.2 FUTURE WORK

Although the work presented in this thesis clearly demonstrated that the modified Z-converter can be controlled for PV based EV/PHEV battery charging applications, few details have been examined simply superficially. For example, the slow response of the MPPT/I_{PV} loop and an even slower response of the battery current loop for the Z-converter are relatively inconvenient. This is due to the fact that these slower loop responses place major limits on the command signals. Furthermore, they also bring to light a critical need for protection circuits that intervene in lieu of the control loop, during common events such as start-up, inrush, shutdowns, and battery insertion. Since these auxiliary systems affect the overall cost, it is critical that they are investigated further. It must also be recalled that the dynamic performance obtained is borne out of non-optimal compensation techniques for MIMO systems; as a result, it can likely be improved. Therefore, future work might examine better suited methods, such as Linear-Quadratic control, Sliding Mode Control, and non-linear feedback de-coupling methods.

Another issue that requires further in-depth analysis is the interaction of the panels and MPPT device with the control loops. In this thesis, the PV source was modeled somewhat rudimentarily, while the MPPT algorithm was replaced by a simple command signal. However, actual MPPT strategies are closed loop systems that share sensed variables, such as panel current, including the converter control system. As such, the MPPT and the converter controllers cannot be practically separated.

The EV/PHEV battery is another element in this present work that was modeled using a straightforward method. However, this trivial battery modeling supposition should not affect the results in a dramatic manner. However, having postulated that the large 120 Hz ripple could be sent to the EV battery, it would indeed be essential to explore whether such a ripple is acceptable and to what extent. This would invoke a study on future trends in EV/PHEV storage technology.

Finally, additional work is needed in order to establish the behavior of the Z-converter in need of light radiation. Indeed, the deployment of a switch (instead of a diode), as the DC blocking element, at the output of the PV source, allows for rectification to occur from the grid. However, such an operating scenario remains to be analyzed when the battery is also present in the system.

REFERENCES

[1]   S. De Breucker, P Jacqmaer, K. De Brabandere, J. Driesen, and R. Belmans, "Grid power quality improvements using grid-coupled hybrid electric vehicles," in *Proc. IEEE Power Electronics, Machines, and Drives Conf.*, Dublin, Ireland, April 2006, pp. 505-509.

[2]   F. Z. Peng, "Z-source inverter," *IEEE Trans. on Industry Applications*, vol. 39, no. 2, pp. 504-510, March 2003.

[3]   P. Fairley, "Electric-car maker touts 10-minute fill-up," *IEEE Spectrum*, Nov 2007.

[4]   S.B. Kjaer, J. K. Pedersen, and F. Blaabjerg, "A review of single-phase grid-connected inverters for photovoltaic modules," *IEEE Trans. on Industry Applications*, vol. 41, no. 5, pp. 1292-1306, Sept. 2005.

[5]   X. Yuan and Y. Zhang, "Status and opportunities of photovoltaic inverters in grid-tied and micro-grid systems," in *Proc. IEEE International Power Electronics and Motion Control Conf.*, Aug. 2006, vol. 1, pp. 1-4.

[6]   M. Meinhardt and G. Cramer, "Past, present and future of grid connected photovoltaic and hybrid power systems," in *Proc. IEEE Power Engineering Society Summer Meeting*, July 2000, vol. 2, pp. 1283-1288.

[7]   J. Newmiller, C. Whitaker, M. Ropp, and B. Norris, "Renewable systems interconnection: distributed PV systems design and technology requirements," U.S. Department of Energy, Oct. 2007.

[8]   F. Z. Peng, M. Shen, and K. Holland, "Application of Z-source inverter for traction drive of fuel cell – battery hybrid electric vehicles," *IEEE Trans. on Power Electronics*, vol. 22, no. 3, pp. 1054-1061, May 2007.

[9] G. Carli and S. Williamson, "On the elimination of pulsed output current in Z-loaded chargers/rectifiers" in *Proc. IEEE Applied Power Electronics Conf. And Expo.*, Washington, D.C., Feb. 2009, pp. 1754-1760.

[10] M. Shen and F.Z. Peng, "Operation modes and characteristics of the Z-Source inverter with small inductance or low power factor," *IEEE Trans. on Industrial Electronics*, vol. 55, no. 1, pp. 89-96, Jan. 2008.

[11] X. Ding, Z. Qian, S.Yang, B. Cui, and F. Z. Peng, "A high-performance Z-source inverter operating with small inductor at wide-range load," in *Proc. IEEE Applied Power Electronics Conf. and Expo*, Feb. 2007 pp. 615-620.

[12] P. C. Loh, D. M. Vilathgamuwa, C. J. Gajanayake, Y.R. Lim and C. W. Teo, "Transient modeling and analysis of pulse-width modulated Z-source inverter," in *Proc. IEEE Industry Applications Conf.*, Oct. 2005, vol. 4, pp. 2782-2789.

[13] C. J. Gajanayake, D. M. Vilathgamuwa, and C. L. Poh, "Small-signal and signal-flow-graph modeling of switched Z-source impedance network," *IEEE Power Electronics Letters*, vol. 3, no. 3, Sept. 2005, pp. 111-116.

[14] J. Hahn, T. Edison, and T. F. Edgar, "A note on stability analysis using Bode plots," *Chemical Engineering Education Journal*, Summer 2001, pp. 208-211.

[15] X. Ding, Z. Qian, S. Yang, and F. Z. Peng, "A new feedforward compensation to reject DC-link voltage ripple in bi-directional Z-Source inverter ASD system," in *Proc. IEEE Applied Power Electronics Conf. and Expo.*, Austin, TX, Feb. 2008, pp. 1809-1813.

[16] Z. Chen, X. Zhang, and J. Pan, "An integrated inverter for a single-phase single-stage grid-connected PV system based on Z-source," *Bulletin of the Polish Academy of Sciences: Technical Sciences*, vol. 55, no. 3, pp. 263-272, 2007.

[17] Y. T. Tan, D. S. Kirschen, and N. Jenkins, "A model of PV generation suitable for stability analysis," *IEEE Trans. on Energy Conversion*, vol. 19, no. 4, pp. 748-755, Dec. 2004.

[18] Y. Xue, L. Chang, S. B. Kjaer, J. Bordonau, and T. Shimizu, "Topologies of single-phase inverters for small distributed power generators: an overview," *IEEE Trans. on Power Electronics*, vol. 19, no. 5, pp. 1305-1314, Sept. 2004.

[19] Characteristics of the Utility Interface for Photovoltaic (PV) Systems, IEC 61727 CDV, 2002.

[20] IEEE Standard for Interconnecting Distributed Resources with Electric Power Systems, IEEE Std. 1547, 2003.

[21] R. Gonzalez, E. Gubia, J. Lopez, and L. Marroyo, "Transformer-less single-phase multilevel-based photovoltaic inverter," *IEEE Trans. on Industrial Electronics*, vol. 55, no. 7, pp. 2694-2702, July 2008.

[22] T. Esram, J. W. Kimball, P. T. Krein, P. L. Chapman, and P. Midya, "Dynamic maximum power point tracking of photovoltaic arrays using ripple correlation control," *IEEE Trans. on Power Electronics*, vol. 21, no. 5, pp. 1282-1291, Sept. 2006.

[23] D. Casadei, G. Grandi, and C. Rossi, "Single-phase single-stage photovoltaic generation system based on a ripple correlation control maximum power point

tracking," *IEEE Tran. on Energy Conversion*, vol. 21, no. 2, pp. 562-568, June 2006

[24] S. B. Kjaer, "Design and control of an inverter for photovoltaic applications," Ph.D. Dissertation, Institute of Energy Technology, Aalborg University, Aalborg, Denmark, 2004.

[25] C. M. Wang, C. H. Su, M. C. Jiang, and Y. C. Lin, "A ZVS-PWM single-phase inverter using a simple ZVS-PWM commutation cell," *IEEE Trans. on Industrial Electronics*, vol. 55, no. 2, pp. 758-766, Feb. 2008.

[26] J. Takesuye and S. Deuty, "Introduction to insulated gate bipolar transistors," Application Note AN1541, Motorola Inc.

[27] P. C. Loh, D. M. Vilathgamuwa, Y. S. Lai, G. T. Chua and Y. Li, "Pulse-width modulation of Z-source inverters," in *Proc. IEEE Industry Applications Conf.*, Oct. 2004, vol.1, pp. 148-154.

[28] X. Ding, Z. Qian, Y. Xie, and F. Z. Peng, "A novel ZVS z-source rectifier," in *Proc. IEEE Applied Power Electronics Conf. and Expo.*, March 2006, pp. 951-955.

[29] H. C. Lamb, E. K. Stefanakos, T. Smith, B. Krakow, C. Hernandez, R. Rodriguez, and M. Kovač, "Efficient photovoltaic charging of electric vehicles," in *Proc. IEEE Southcon*, Orlando, FL, March 1994, pp. 47-52.

[30] California Energy Comminssion, "Photovoltaic chargeport demonstration," *Public Interest Energy Research*, Oct. 1999.

[31] J. M. A. Myrzik and M. Calais, "String and module integrated inverters for single-phase grid connected photovoltaic systems - a review," in *Proc. IEEE Power Tech Conf.*, Bologna, Italy, June 2003.

[32] IEEE Standard 929-2000, *IEEE Recommended Practice for Utility Interface of Photovoltaic (PV) Systems*, Jan. 30, 2000.

[33] D. G. Holmes, "The significance of zero space vector placement for carrier-based PWM schemes," *IEEE Trans. on Industry Applications*, vol. 32, no. 5, pp.1122-1129, Sept. 1996.

[34] R. González, J. López, P. Sanchis, and L. Marroyo, "Transformer-less inverter for single-phase photovoltaic systems," *IEEE Trans. on Power Electronics*, vol. 22, no. 2, pp. 693-697, March 2007.

[35] T. Kerekes, R. Teodorescu, and U. Borup, "Transformer-less photovoltaic inverters connected to the grid," in *Proc. IEEE Applied Power Electronics Conf. and Expo.*, Feb. 2007, pp.1733-1737.

[36] C. J. Gajanayake, D. M. Vilathgamuwa, and P. C. Loh, "Modeling and design of multi-loop closed loop controller for Z-source inverter for distributed generation," in *Proc. IEEE Power Electronics Specialists Conf.*, June 2006, pp.1-7.

[37] B. Farhangi and S. Farhangi, "Application of z-source converter in photovoltaic grid-connected transformer-less inverter," *Journal of Electrical Power Quality and Utilization*, vol. 12, no. 2, pp. 41-45, 2006.

APPENDIX A

AVERAGE MODEL FOR THE DC/DC CONVERTER

Fig. 5-9 depicts a simple technique to derive the equivalent circuit of the DC/DC converter, as seen from the Z-circuit. Unfortunately, this derivation is oversimplified, as it does not consider some parasitic components. In order to get a more precise model, the schematic in Fig. A-1 is redrawn, including all the ESRs. Also, only ½ of the circuit needs to be shown, as long as the secondary side is split into two parallel paths.
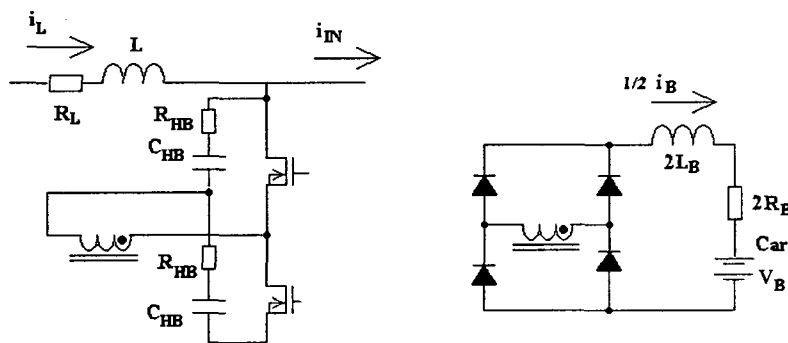
Fig. A-1 Equivalent circuit for half of the DC/DC converter circuit

Fig. A-2 shows the two topological configurations of the circuit, as the switches are on 50% of the time, in complementary fashion.
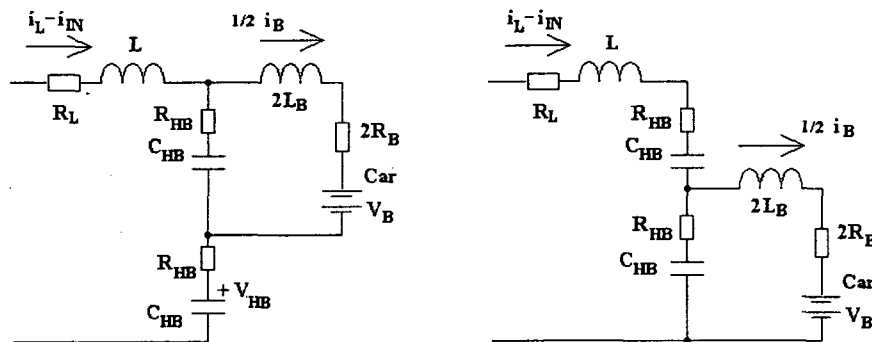
Fig. A-2 Topological configurations

It is easy to obtain average equation for the inductance $2L_B$ and capacitors C_{HB}.

$$C_{HB}\frac{dV_{HB}}{dt} = i_L - i_{IN} - \frac{1}{4}i_B \qquad L_B\frac{di_B}{dt} = V_{HB} + (i_L - i_{IN})R_{HB} - \frac{1}{2}(R_{HB} + 2R_B)i_B - V_B$$

Now, consider the configuration shown in Fig. A-3 (left):
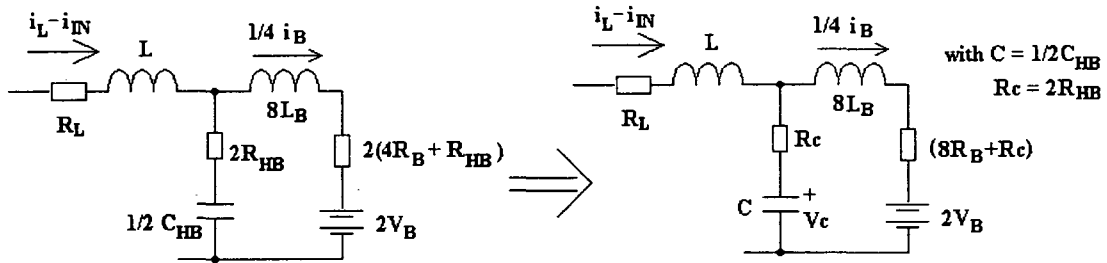
Fig. A-3 Equivalent averaged circuits for the DC/DC converter

The equations describing this circuit are:

$$C_{HB}\frac{dV_{HB}}{dt} = i_L - i_{IN} - \frac{1}{4}i_B \qquad L_B\frac{di_B}{dt} = V_{HB} + (i_L - i_{IN})R_{HB} - \frac{1}{2}(R_{HB} + 2R_B)i_B - V_B$$

These values match exactly those obtained earlier. Hence, this circuit, or the equivalent circuit of Fig. A-3 (right), accurately represents ½ of the DC/DC converter.

APPENDIX B

SWITCHING PATTERN FOR Z-CONVERTER

IGBT turn-off losses are calculated based on the instantaneous positive current. If the current is negative (through the anti-parallel diode), switching losses are considered negligible. Operation in inverting mode is different from operation in rectifying mode. The switching patterns are as shown below.
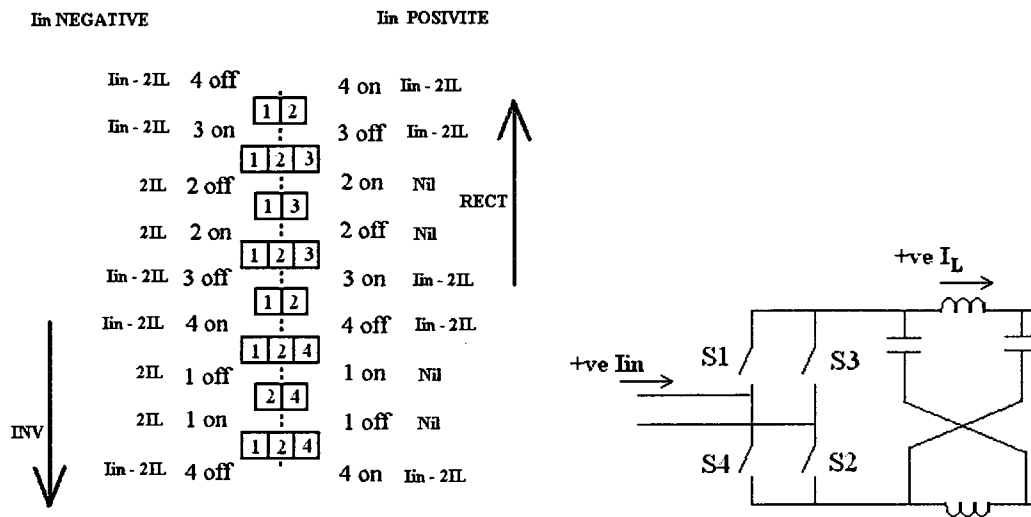
On the left hand side, the sequence used for inversion is read from top to bottom, and is valid during the ½ cycle that the input current is negative. When the input current is positive, the switch numbers 1 and 2 are simply replaced with 3 and 4, respectively. The right hand side shows the sequence in rectifying mode, read from bottom to top, when the input current is positive. When the input current is negative, the switch numbers 1 and 2 are simply replaced with 3 and 4, respectively.

For the inverting mode, the switched current is shown on the left hand side, for each transition. Since the turn-off loss is of critical importance, the value for switch 1 will

be $2I_L$, for the negative ½ cycle, and I_{IN}-$2I_L$, for the positive ½ cycle. The switching

losses for the DC blocking IGBT are low, because the anti-parallel diode conducts first at

turn on and turns off last at turn off.

For the rectifying mode, the switched current is shown on the right hand side, for

each transition. The value for switch 1 will be I_{IN}-$2I_L$, for the negative ½ cycle, and very

low, for the positive ½ cycle. The reason the losses are small during the positive ½ cycle

is, because the DC blocking IGBT can be used to force a current reversal in the bridge

IGBTs [28]. This implies, however, that the switching turn-on loss on the DC block

IGBT will now be significant.

APPENDIX C

DETAILED POWER LOSS MAPS

Simulations were run on all three topologies discussed in this thesis, at three different power levels, and for all four power flow paths. Input voltage and PV voltage were set at nominal values. Below are the related detailed power mappings.

Z-Converter (Scheme 1)

	Power W	IGBT Br ON	IGBT-Br TURN ON	IGBT Br TURN OFF	IGBT5 ON	IGBT5 TURN ON	Z-INDUCTORS	Z-CAPACITORS	INPUT INDUCTOR	XMER	DIODES	TOTAL	EFFICIENCY
	5000	44	18	53	15.1	12	5.03	22.1	0	25	35	229.23	0.95616372
PV-BAT	2500	24.8	18	27.3	8	9.2	1.38	7	0	25	18	138.68	0.94744342
	400	16	17	3.8	0.8	6.1	0.2	1.1	0	25	0	70	0.85106383
GRID-BAT	5000	48.8	18.4	31.6	3.2	2.2	1.2	11.9	8.36	100	33	258.66	0.95081256
	2500	26.2	18.5	19	3.1	1	0.4	4.4	2.24	44	18	136.84	0.94810455
	400	9.2	17.8	8.2	2.9	0	0.2	1.2	0.22	25	0	64.72	0.86073334
PV-GRID	5000	97.8	18.6	93.2	13.7	12	8.15	24	7.4	100	4	378.85	0.92956673
	2500	51.9	18.2	55.4	5.5	8.8	2.3	6.7	1.8	44	2	196.6	0.92709338
	400	2.75	17.2	9.7	0.8	5.5	0.2	1	0	25	0	62.15	0.86551985
	5000	62.2	19.9	31.9	3.2	8.4	1.2	5.05	7.2	100	24	263.05	0.95001948
BAT-GRID	2500	25.4	18.7	16.2	0.8	5.5	0.4	1.1	1.8	44	13	126.9	0.95169211
	400	2.5	22.1	3.8	0	3.3	0.2	0.5	0.3	25	4	61.7	0.86636344

HF Transformer-Isolated Topology with DC link

	Power W	IGBT1-IGBT4 ON	IGBT1-IGBT4 SW ON	IGBT1-IGBT4 SW OFF	IGBT9-10 ON	IGBT9-10 SW ON	IGBT9-10 SW OFF	DIODES	IGBT11-14 ON	IGBT11-14 SW ON	IGBT11-14 SW OFF	HF XFOs	IND. AND CAPS	TOTAL	EFFICIENCY
	5000	0	5.3	0.2	52	21.8	53.7	19.1	0	0	0	100	6.1	258.2	0.950895744
PV-BAT	2500	0	5.7	0.3	26.1	22.1	25	9.2	0	0	0	58	2	148.4	0.943966168
	400	0	4.8	0	3.4	20.6	3	1.6	0	0	0	50	0.7	84.1	0.826275563
GRID-BAT	5000	65.8	5.1	15.9	52.1	21.8	52.7	0	0	0	0	50	28.4	291.8	0.944858082
	2500	32.9	5.7	7.6	25.8	21.1	25.3	0	0	0	0	29	7	154.4	0.941832429

	Power W														
	400	5.5	4.8	2.1	3.1	20.9	2.2	0	0	0	0	25	0.2	63.8	0.862440707
PV-GRID	5000	78.1	5.7	15.3	0	10.1	0	18.9	0	0	0	50	17.5	195.6	0.96235276
	2500	38.3	5.7	7.4	0	9.4	0	9.5	0	0	0	29	4.3	103.6	0.960208941
	400	6.2	4.4	2.8	0	6.5	0	1.5	0	0	0	25	0.1	46.5	0.895856663
	5000	80.1	5.7	15.1	0	0	0	0	54.6	20.7	47	100		323.2	0.939284641
BAT-GRID	2500	37.5	5.6	7.4	0	0	0	0	27.2	20.6	23.5	58		179.8	0.932905441
	400	6.6	4.6	2.5	0	0	0	0	4.3	18.6	3.7	50		90.3	0.815827045

Transformer-less topology

	Power W	IGBT1 IGBT2 ON	IGBT3 IGBT4 ON	IGBT5-IGBT10 ON	IGBT1/2 TURNON	IGBT1/2/3/4 TURNOFF	IGBT5/10 TURNON	IGBT5/10 TURNOFF	INP. IND.	XMER	BAT IND.	DIODES	TOTAL	EFFICIENCY
	5000	0.8	1.6	32	2.6	1	2.2	30.2	0	50	6.8	30	157.2	0.96951834
PV-BAT	2500	0.8	1.8	14.8	2.8	1	2.2	13.5	0	32	1.7	15	85.6	0.96689356
	400	0.4	0.5	2.5	2.2	1	2.2	2.1	0	25	0	2.5	38.4	0.91240876
GRID-BAT	5000	20	38	31.6	2.1	8.4	2.2	30	10.3	50	6.8	30	229.4	0.95613263
	2500	11.2	18.9	16.2	2.1	4.1	2.2	16.9	2.6	32	1.5	15	122.9	0.95314347
	400	1.8	3.1	2.6	2.4	1.8	2.5	2.7	0.5	25	0.2	2.5	45.1	0.89867446
PV-GRID	5000	40.2	28.8	0	2.3	17.2	2.2	0	10.2	50	0	0	151.9	0.97051573
	2500	20	15.1	0	2	8.7	2.1	0	2.7	32	0	0	82.4	0.9680917
	400	3.4	2.4	0	2	1.5	2.4	0	0	25	0	0	36.7	0.91596061
	5000	37.9	28.1	85.2	2	17.1	2	18.6	10.2	50	6.8	0	257.9	0.95095
BAT-GRID	2500	19	14.5	45.5	2	8.8	2	9	2.9	32	1.5	0	137.2	0.94797513
	400	3.1	2.5	2	1.9	1.5	2	6	0.5	25	0	0	44.5	0.89988751